

# Analysis of Thermal Flow Sensor Technology

For the Bachelor's Degree of

Anton Østergaard Thorsen, Sara Linnet & Signe Husum Frederiksen



This page is intentionally left blank.

---

# Analysis of Thermal Flow Sensor Technology

---

by

Anton Østergaard Thorsen, Sara Linnet & Signe  
Husum Frederiksen

Name	Position	Student Number	Contacts
Anton Østergaard Thorsen	Bachelor Student	au681040	anton-thorsen@hotmail.com
Sara Linnet	Bachelor Student	au678176	saralinnet0@gmail.com
Signe Husum Frederiksen	Bachelor Student	au636935	signehusumf@gmail.com

Supervisor	Position	-	Contacts
Mahdi Abkar	Associate Professor, Aarhus University	-	abkar@mpe.au.dk
Casper Pedersen	Senior Specialist, Grundfos	-	capederssen@grundfos.com
Hanna Brigitte Becker	Sensor Specialist, Grundfos	-	hbecker@grundfos.com

Co-Supervisors	Posisiton	-	Contacts
Navid Zehtabiyan-Rezaie	Post-doc, Aarhus University	-	zehtabiyan@mpe.au.dk

University: Aarhus University  
Department: Department of Mechanical and Production Engineering  
Project Duration: February, 2023 – June, 2023

Last Compiled: November 7, 2024



DEPARTMENT OF MECHANICAL AND PRODUCTION ENGINEERING  
AARHUS UNIVERSITY

# Abstract

This report aims to investigate the operation and stability of an iST thermal mass flow sensor module. Flow sensors have diverse applications ranging from dosing to leakage detection and the knowledge provided by the sensor aids in a potential system optimization. Knowledge of operational range, stability, and potential installation requirements is however crucial, as these parameters impact the usability of the sensor. The operation principle of the sensor relies on heat transfer depending on fluid velocity by use of the constant temperature anemometry principle. For this reason, this work includes theoretical background on both fluid dynamics and heat transfer.

The investigation assesses the impact of changes in sensor geometry, differential temperature settings, and varying flow conditions on the sensor's response experimentally. Lastly, the sensor module was installed in challenging environments in which both inlet and thermal conditions were altered to examine whether any installation requirements were needed. To investigate the assumed flow and thermal conditions within the sensor, CFD analysis was utilized and qualitatively compared with the experimental results.

Altering flow velocity and temperature settings, the output proved to follow King's Law, thus, allowing for analytically predicting the sensor output. Furthermore, varying the velocities proved a decrease in stability going from low flow rates to higher. The sensor response proved most unstable at transitional flows with Reynolds numbers,  $2000 < \text{Re} < 3000$ . This tendency was further amplified by the increase in sensor diameter, with the largest sensor showing a standard deviation ten times that of the smallest sensor.

In testing challenging environments it was, amongst others, tested whether the sensor response was affected when being exposed to forced convection. Externally applied forced convection proved to have a significant impact on the sensor response both in terms of measured voltage and stability. With exposure to a wind-like environment, it was found that introducing insulation resulted in more accurate measurements along with increased stability of the sensor response. Furthermore introducing bends was found to affect the stability of the output and these should therefore be avoided. Installation considerations and ideal operating ranges have thus been found based on extensive investigation of differing working conditions and environments.

# Table of Contents

<b>Abstract</b>	<b>i</b>
<b>Table of Contents</b>	<b>ii</b>
<b>List of Figures</b>	<b>iii</b>
<b>List of Tables</b>	<b>v</b>
<b>Nomenclature</b>	<b>vi</b>
<b>1 Introduction</b>	<b>1</b>
1.1 Motivation for Investigation . . . . .	1
1.2 Theory of Operation of iST Thermal Mass Flow Meter . . . . .	2
1.3 Hypothesis and Report Overview . . . . .	3
<b>2 Methodology</b>	<b>4</b>
2.1 Experiments . . . . .	4
2.1.1 Experimental Setup . . . . .	4
2.1.2 Testing Equipment . . . . .	6
2.1.3 Experimental Areas of Investigation . . . . .	8
2.1.4 Experimental Execution . . . . .	10
2.1.5 Experimental Considerations . . . . .	12
2.1.6 Statistics . . . . .	12
2.1.7 Derivation of Mass Flow . . . . .	13
2.1.8 Data Analysis of Voltage Time Series . . . . .	13
2.2 Numerical Study . . . . .	13
2.2.1 Governing Equations of Fluid . . . . .	13
2.2.2 Heat Transfer . . . . .	17
2.2.3 Numerical Method . . . . .	18
<b>3 Results and Discussion</b>	<b>24</b>
3.1 Voltage Output and Standard Deviation . . . . .	24
3.2 Effect of Inlet Boundary Conditions - Bends . . . . .	29
3.3 External Forced Convection . . . . .	31
3.4 Simulations . . . . .	36
3.4.1 Comparison of Simulated and Experimental Results . . . . .	37
<b>4 Conclusion</b>	<b>39</b>
<b>5 Bibliography</b>	<b>41</b>
<b>A Experimental Pictures</b>	<b>42</b>
<b>B Additional Theory</b>	<b>43</b>
B.1 Wheatstone Bridge . . . . .	43
B.2 Simplification of Equation for Wall-Adjacent Cell Size . . . . .	43
B.3 Ohm's Law . . . . .	44
<b>C Supplementary Plots - Experiments</b>	<b>45</b>
<b>D Supplementary Plots - Numerical Study</b>	<b>52</b>

# List of Figures

1.1	Working principle of the iST thermal convection mass flow sensor module [8]. . . . .	2
1.2	Simplified diagram of Wheatstone Bridge which is used in the CTA principle [10]. . . . .	2
2.1	Sketch of the experimental setup. Red arrows indicate the direction of flow. . . . .	4
2.2	Picture of the experimental setup at Grundfos. . . . .	5
2.3	Close-up picture of the experimental sensor setup at Grundfos. . . . .	5
2.4	Different designs of sensor modules with an indication of placement of heater and sensor as well as visualization of diameter reference. The blue arrow indicates the flow direction. . . . .	6
2.5	Sensor module connected to flow demo board [10]. The blue arrow indicates the flow direction. . . . .	7
2.6	Back side of flow demo board [10]. . . . .	7
2.7	Visualization of bends in the experimental setup. The blue arrows indicate the flow direction. . . . .	9
2.8	Illustration of expected velocity flow profiles through the bend. . . . .	9
2.9	Illustration of orientations with the sensor module at position 2. The blue arrows indicate the flow direction. . . . .	10
2.10	Insulation layers with a thickness of 11 mm and alternating lengths. Left: insulation layer with a length of 35.7 mm. Right: insulation layer with a length of 232 mm. . . . .	11
2.11	Flow profiles of laminar flow and turbulent flow. . . . .	14
2.12	Dimensionless mean velocity, $u^+$ , in a pipe for turbulent flow at a dimensionless distance $y^+$ from the wall [16]. . . . .	16
2.13	The CAD-model of $D_2 = 5.0 \text{ mm}$ . . . . .	19
2.14	The four different mesh sizes used to determine convergence. . . . .	21
2.15	Residual plots for $\Delta T = 15.9^\circ\text{C}$ , . . . . .	21
2.16	Convergence for the temperature at heater and sensor for mesh size 2 for $\Delta T = 15.9^\circ\text{C}$ , $U = 0.0033 \text{ m/s}$ . . . . .	22
2.17	Line heater for different mesh sizes of $\Delta T = 15.9^\circ\text{C}$ . . . . .	22
2.18	Convergence of heat transfer rate for $\Delta T = 15.9^\circ\text{C}$ , $U = 0.0033 \text{ m/s}$ . . . . .	23
3.1	Two 10 minute tests with similar velocities for $D_1 = 3.2 \text{ mm}$ . . . . .	24
3.2	Voltage time series for $D_2$ at $\Delta T = 13.4^\circ\text{C}$ . Reynolds number in the transitional region produces noisier time series. . . . .	25
3.3	The experimental results for $D_1$ and $D_2$ fitted against King's Law. Note that for the found fits the volume flow rate should be inserted in mL/min. . . . .	25
3.4	Output voltage with standard deviation for three sensor settings and three pipe diameters. . . . .	26
3.5	Standard deviation of normalized voltage for all pipe diameters. . . . .	27
3.6	Standard deviation of normalized voltage for $D_2$ . . . . .	28
3.7	Standard deviation for five different sensor settings on three sensor diameters. . . . .	29
3.8	Voltage time series of four different orientations, $L = 22 \text{ mm}$ . . . . .	30
3.9	Average voltage for four different orientations for straight pipe and pipe with a bend, $L = 200\text{mm}$ . . . . .	30
3.10	Standard deviation for bend results for different lengths. . . . .	31
3.11	Forced convection test in 1-1-4 interval. . . . .	31
3.12	Forced convection impact on two temperature settings. The experiment was conducted with a Reynolds number of $Re = 2350$ . . . . .	32
3.13	Voltage and standard deviation as a function of Reynolds for convection experiment. . . . .	33
3.14	Voltage and standard deviation vs. insulation thickness. . . . .	34
3.15	Standard deviation vs. insulation thickness. . . . .	34
3.16	Forced convection tests in 1-1-2 interval. 95% settling time (blue)=6 s after convection, 99% settling time (red)=68 s, average change (black)=29 s. The temperature setting was $\Delta T=15.9^\circ\text{C}$ . . . . .	35
3.17	Temperature distributions for $\Delta T = 15.9^\circ\text{C}$ , $U = 0.0033 \text{ m/s}$ . . . . .	36

3.18 Bend-pipe velocity contours for $\Delta T = 15.9^\circ\text{C}$ with inlet-velocity $U = 0.1873 \text{ m/s}$ , the maximum investigated velocity for bends. White arrows indicate flow direction. . . . .	37
3.19 Comparison of straight pipe simulation with experiments for $\Delta T = 8.5^\circ\text{C}$ and $\Delta T = 15.9^\circ\text{C}$ . . . . .	37
3.20 Comparison of bend simulation and experimental results for $\Delta T = 15.9^\circ\text{C}$ . . . . .	38
A.1 Picture of largest sensor with diameter $D_3$ in foreground and second largest sensor with diameter $D_1$ in background connected to pipes. . . . .	42
B.1 Wheatstone Bridge . . . . .	43
C.1 Long duration tests for pipe diameters $D_2$ and $D_3$ . . . . .	45
C.2 Six voltage time series of different velocities. . . . .	45
C.3 Voltage fits for $D_3$ . The minimum $R^2$ is 0.99. . . . .	46
C.4 Average vol +/- standard deviation for three sensor diameters. . . . .	46
C.5 Average vol +/- standard deviation for three sensor diameters. . . . .	47
C.6 Normalised voltage and standard deviation for three sensor diameters. . . . .	47
C.7 Normalised voltage and standard deviation for two sensor diameters. . . . .	48
C.8 Normalised voltage and standard deviation for three sensor diameters. . . . .	48
C.9 Normalised voltage and standard deviation for two sensor diameters. . . . .	49
C.10 Average voltage for orientation test of differing lengths, L, with control test on a straight pipe. . . . .	49
C.11 Standard deviation vs. vol. flow rate for orientation test. . . . .	50
C.12 Standard deviation vs. temperature setting for orientation test $\Delta T$ . . . . .	50
C.13 Standard deviation vs. temperature setting for forced convection test. . . . .	51
C.14 Standard deviation vs. Reynolds for forced convection test. . . . .	51
D.1 Temperature contours for mesh sizes 1, 3 and 4, for laminar flows where: $\Delta T = 15.9^\circ\text{C}$ , $U = 0.0033 \text{ m/s}$ . . . . .	52
D.2 Residuals for laminar flows for all mesh sizes for $\Delta T = 15.9^\circ\text{C}$ , $U = 0.0033 \text{ m/s}$ . . . . .	53
D.3 Temperature convergence at the sensor for laminar flows for mesh sizes 1, 3 and 4 for $\Delta T = 15.9^\circ\text{C}$ , $U = 0.0033 \text{ m/s}$ . . . . .	53
D.4 Temperature convergence at the heater for laminar flows for mesh sizes 1, 3 and 4 for $\Delta T = 15.9^\circ\text{C}$ , $U = 0.0033 \text{ m/s}$ . . . . .	53
D.5 Convergence of heat transfer rate for bends for $\Delta T = 15.9^\circ\text{C}$ , $U = 0.0069 \text{ m/s}$ . . . . .	54

# List of Tables

2.1	Table of used flow demo board settings and the corresponding temperature differences. . . . .	11
2.2	Properties of water and steel . . . . .	19
2.3	Calculated values of wall-adjacent cell sizes. . . . .	20
3.1	Table of the percentage difference between flow regions averaged across temperature difference. Lam: Laminar flow region. Trans: Transitional flow region. Turb: Turbulent flow region. . . . .	27
3.2	Accuracy of fits on additional data points. . . . .	28
3.3	Table showing temperature setting, avg. volt and percent-change for forced convection experiment	32
3.4	Table showing temperature setting, avg. volt and percent-change for forced convection experiment	32
3.5	Table showing avg. volt with corresponding vol. flow and percent-error for forced convection experiment. . . . .	35

# Nomenclature

## Physics Constants

$g$	Gravitational acceleration	9.81 m/s <sup>2</sup>
-----	----------------------------	-----------------------

## Other Symbols

$\Delta T$	Temperature difference upheld by sensor module	°C
$\dot{m}$	Mass flow rate	kg s <sup>-1</sup>
$\dot{Q}$	Volume flow rate	mL min <sup>-1</sup>
$D$	Diameter	mm
$P$	Power	J s <sup>-1</sup> , W
$T$	Temperature	K
$U$	Velocity	m s <sup>-1</sup>
$V$	Voltage	V
$D_x$	D followed by a number e.g. D <sub>2</sub> corresponds to sensor diameter 2 of 3	mm

# 1 | Introduction

## 1.1 | Motivation for Investigation

With the advancement of technology, society gains still more tools to advance and streamline the knowledge and products, produced by earlier generations. The development of new materials, higher computational power and constantly improving software programs, ensures this advancement by allowing efficient production of lighter and stronger products. This advancement is not only economically beneficial but also necessary for society if we are to overcome global environmental and social problems.

The optimization of products in dynamic systems is challenging. The constantly changing environments and unpredictability, result in products having to be sturdy and reliable, thus limiting the evolution of the products. To achieve a truly optimized product the system needs to be 'smart'. The product needs to have knowledge of the environment to always optimize operation under the given conditions. The only way to achieve this goal is by utilization of sensors. Thanks to even smaller and more efficient micro-controllers, integrated sensors have become more versatile and are now easier implemented into a wide range of systems. This report analyzes such a sensor, integrated into a flow module, investigated in collaboration with pump manufacturer, Grundfos.

Grundfos produces 17 million pumps a year and covers 50% of the global market for circulation pumps. Achieving even a slight optimization of these pumps by utilizing integrated sensors, could therefore have a significant global impact. This could be due to the extended lifetime of a pump, as a result of optimized operation, as the system has more knowledge of the flow and other physical properties. The optimized pump operation would also minimize the needed power and, thereby, the CO<sub>2</sub> emission.

The investigated thermal mass flow sensor module is, by the producer, Innovative Sensor Technology, iST, described as an "easy and low-cost solution to optimize [processes] and minimize machine downtime" [11]. Working based on thermal dispersion, the investigated mass flow sensor is applicable as a flow monitoring device, continuously monitoring systems utilizing temperature control, pumping, and filling. With the ability to measure low flows in small geometries, with rapid response time, the iST thermal mass flow meter enables preventive maintenance by minimizing potential machine downtime, as it can detect process system deviations from set points, immediately. Deviations in coolant flow speed in cooling circuits or leakage in systems are easily detected by the integrated thermal mass flow meter, which, due to the high sensor sensitivity at low flow rates, could even include drip detection. Additionally, the application areas also include dosing systems, such as dosing pumps and white goods.

In the existing market for thermal mass flow meters, the iST thermal mass flow sensor module is a new generation of flow meters, with its out-of-liquid, OOL, design, assuring corrosion resistance and robustness [8], as the only wetted material is the stainless steel pipe wall which separates the measuring element from the flow medium. Other non-invasive technologies, such as ultrasonic flow sensors, are an alternative to thermal flow sensors. There are two general sensing methods for ultrasonic sensors. The time of travel method measures the time between pulses sent with and against the fluid flow. The Doppler method sends out a pulse that is reflected by particles. The motion of the particles changes the frequency of the pulse which then travels to a receiver. This frequency shift is proportional to the fluid velocity. The Doppler method, however, has the disadvantage of being very sensitive to temperature change. Ultrasonic flow sensors have multiple advantages, such as high accuracy as well as having no moving parts, meaning low maintenance. It does, however, have a higher upfront cost than many other flow sensor options [7]. Ultrasonic flow sensors are a fast-growing technology, where the improvement of hardware as well as improving noise filtering algorithms makes this technology a strong competitor to thermal mass flow sensors in certain applications [12] [5]. A limitation of the iST thermal mass flow sensor is that it requires calibration according to the liquid in use. Other types of sensors do not need calibration. Such a flow sensor, which is widely used and is capable of measuring both the flow and density of a fluid, is the Coriolis flow meter. In a Coriolis flow meter, the fluid moves into vibrating tubes, and by considering the phase shift between the vibrations at the inlet and outlet, as well as the frequency of the vibrations the mass flow and density can be found [19]. However, Coriolis flow meters are complicated, and thus costly, assemblies. For this reason, it might be a viable option to

combine the iST thermal mass flow sensor with a flow characterization method. One article suggests such a method in combination with the iST thermal mass flow sensor to achieve a system that both characterizes and measures the flow of the fluid, thus rendering the need for calibration of the iST device unnecessary [3].

## 1.2 | Theory of Operation of iST Thermal Mass Flow Meter

The iST thermal mass flow meter, with the integrated OOL sensor, is classified as a convection flow meter operating by constant temperature anemometry, CTA [8]. As visualized in figure 1.1, this type of thermal mass flow sensor operates with a heater and sensor, across which a constant temperature difference,  $\Delta T$ , is set and held. The sensor, placed upstream on the stainless steel tube design, is a Resistance Temperature Detector, RTD, whose resistance changes as its temperature changes. The heater, to which the power is supplied, is placed, and aligned with the sensor, downstream on the tube.

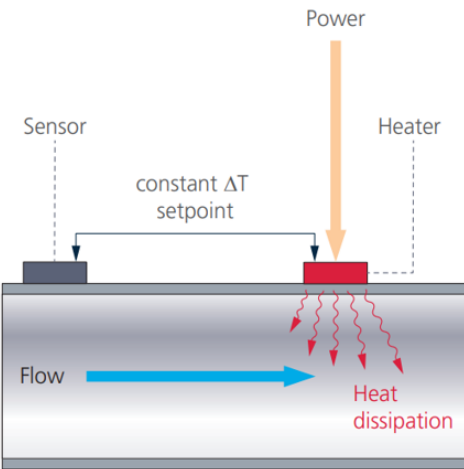


**Figure 1.1 | Working principle of the iST thermal convection mass flow sensor module [8].**

As the dissipated heat is transported away by the fluid flow, forced convection takes place, which affects the set temperature difference between the sensor and the heater. The attached electronic CTA control circuit is to assure a set, constant  $\Delta T$  across the heater and the sensor by supplying a certain power to the heater.

The CTA control circuit utilizes an analog Wheatstone Bridge as visualized in a simplified version in figure 1.2.

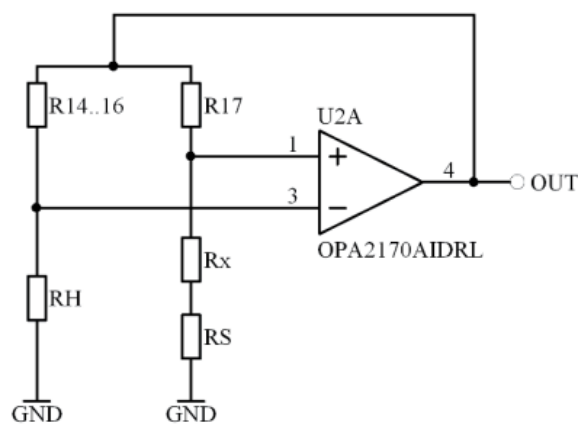


**Figure 1.2 | Simplified diagram of Wheatstone Bridge which is used in the CTA principle [10].**

In the Wheatstone Bridge, the sensor and heater form two opposite 'legs', RS and RH, in accordance with figure 1.2. The circuit aims to achieve a balanced bridge, which is met once the heater has reached the given elevated temperature and, thereby, the necessary resistance. For more theory on the Wheatstone Bridge, see appendix B.1. This is done by utilization of an operational amplifier which, incrementally, adjusts the power until the given requirement is met. The power necessary to reach the given temperature will be dependent on the velocity

of the flow. Increasing flow rate means higher heat removal and, thus, more power must be supplied in order for the temperature difference to remain constant. Thus, the output voltage will be related to the mass flow passing through the flow meter. The raw output voltage signal data can be calibrated by use of King's law which, mathematically, describes heat transfer in flows. According to [8], King's law can be described by

$$P = A + B\dot{m}^C, \quad (1.1)$$

which conveys the relationship between the heater power,  $P$ , and the mass flow,  $\dot{m}$ . The parameters  $A$ ,  $B$ , and  $C$  of equation 1.1, are determined in accordance with the fittings of the characteristic curves derived from experimentally found raw data.

## 1.3 | Hypothesis and Report Overview

The aim of this report is to investigate the thermal mass flow sensor module by iST. With equipment provided by Grundfos, experiments were conducted in order to investigate the capabilities and operational performance of the thermal mass flow sensor module. Furthermore, a numerical study was conducted to validate the results of the experiments.

As mentioned, the electrical power supplied to the heater by the flow demo board, presents the measured output variable, changing depending on the flow velocity. Although the sensor is able to operate in a measuring range of 0 mL/min to 3000 mL/min [9], iST states laminar flow to be the most suitable for measurements with the sensor [11]. The velocity of the fluid determines the state of the flow. This report seeks to investigate the ideal operating range of the iST thermal mass flow sensor module.

The ideal operating range was investigated across altering flow regimes by varying the flow velocity through sensor modules of different sizes. Evaluating the experimentally extracted output voltage at different set flow velocities by statistical parameters, such as standard deviation, gives insight into the stability of the operation. The operational stability of the sensor module was also investigated across varying temperature difference settings and varying the sensor size. Furthermore, the operational performance was investigated by altering the operating conditions of the iST thermal mass flow sensor module. One such operating condition was the inlet condition, which was altered by introducing bends, the effect of which, was of interest to evaluate. The bend was expected to influence the flow profile and change the local flow velocities at the location of the sensor. With an expected influenced velocity profile, the effect of changing the sensor orientation was investigated. Such an investigation would indicate the ideal installation requirements of the sensor module.

Moreover, the sensitivity of the sensor module was also of interest, as such might define further installation restrictions and ideal working conditions. With the sensor module's workings based on heat transfer, the effect of further introducing externally forced convection was evaluated. The effect of forced convection was further analyzed by adding layers of insulation to the sensor module.

Finally, the experimentally extracted relations were qualitatively validated with numerically derived results from simulations using computational fluid dynamics, CFD, from the computer application Ansys Fluent.

## 2 | Methodology

This chapter covers the extraction of both experimental and numerical results for analysis while also covering the theoretical foundation governing the experimental and numerical study of the investigation. The theories covered stem from fluid analysis as well as heat transfer. Additionally, some statistical tools used for the analysis are elaborated upon in this chapter.

### 2.1 | Experiments

The experiments described in this report were conducted at Grundfos facilities. The setup, the equipment, and the experimental execution are elaborated upon in the following section. Additionally, the considerations dealt with during the conduction of the performed experiments are presented in detail.

#### 2.1.1 | Experimental Setup

The general experimental setup was constructed as visualized in figure 2.1, with tap water as the medium. Tank 1, the inlet tank, was the main water tank, tank 2 was primarily purposed for recirculation of the water and tank 3, the outlet tank, was for enabling measurement of the mass flow via a strategic placement on a weighing scale. From tank 1 to tank 3 the tap water was to pass through two valves and continue in straight pipes before entering the sensor module.

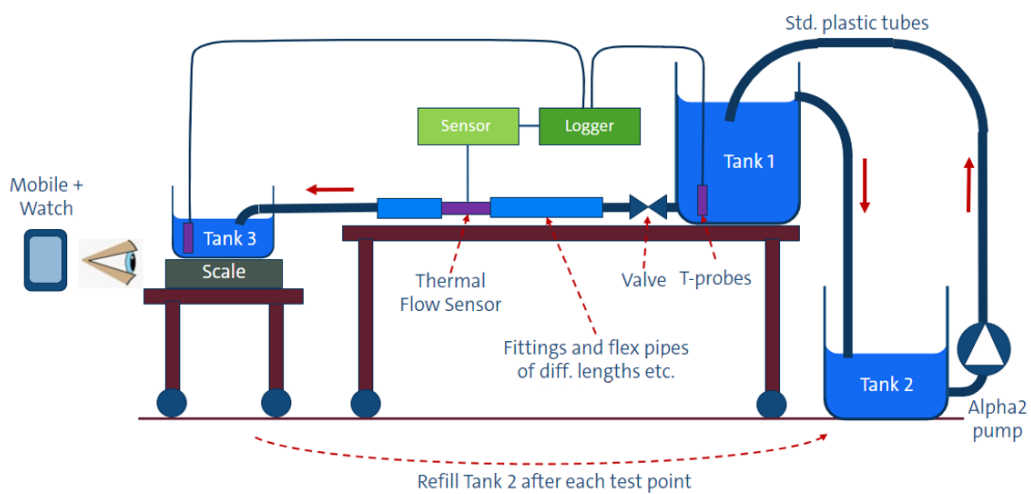
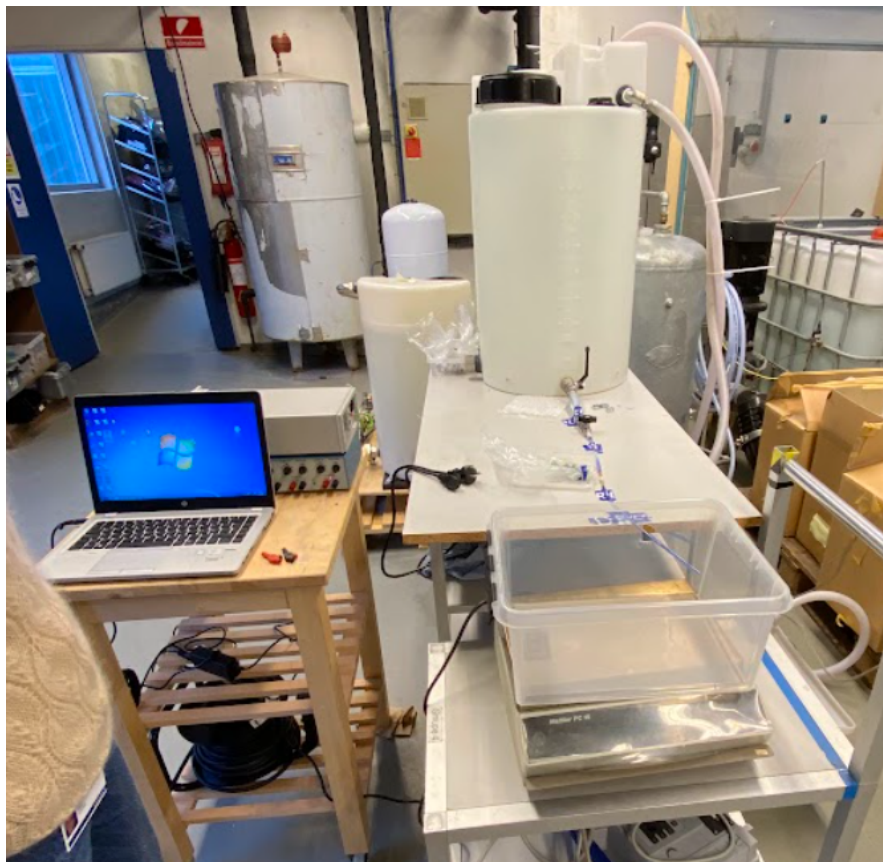
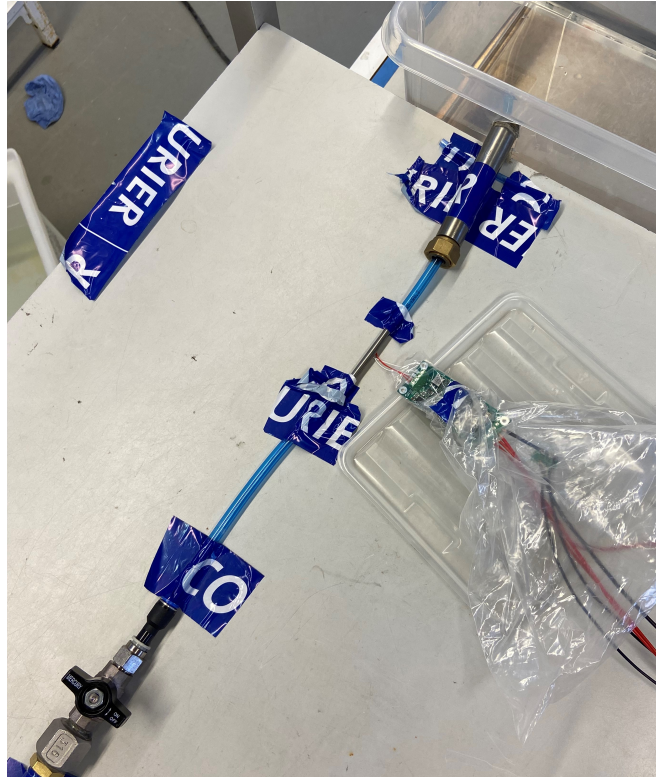


Figure 2.1 | Sketch of the experimental setup. Red arrows indicate the direction of flow.

The iST thermal mass flow sensor module in use was attached to a data logger measuring the output voltage of the sensor. The data logger also measured temperature by the placement of three temperature probes; one in tank 1, one in tank 3, and one placed in the room for measurement of the room ambient temperature, for reference. The logger was connected to a PC, visible on the left side of figure 2.2, for the collection and extraction of data.



**Figure 2.2 | Picture of the experimental setup at Grundfos.**



**Figure 2.3 | Close-up picture of the experimental sensor setup at Grundfos.**

As visible in figure 2.3, the pipes were taped to the table to ensure a straight traveling path for the fluid flow.

## 2.1.2 | Testing Equipment

The experimental setup included some larger testing equipment. The models of the used equipment will be described along with relevant parameters.

### Sensor Module and Pipes

The sensor modules in use were of three varying sizes and of two design types. The design of the two smallest sensor modules is visualized on the left of figure 2.4 with the heater and the sensor aligned on the length of the stainless steel tube. The smallest evaluated sensor module was of an inner diameter,  $D_{inner}$ , of  $D_1 = 3.2$  mm and the second smallest of an inner diameter,  $D_{inner}$ , of  $D_2 = 5$  mm.

On the right of figure 2.4, the altered design for the largest sensor module is visualized with the heater and the sensor on opposite sides of the tube. The inner diameter,  $D_{inner}$ , of the largest evaluated sensor module was  $D_3 = 9.5$  mm.

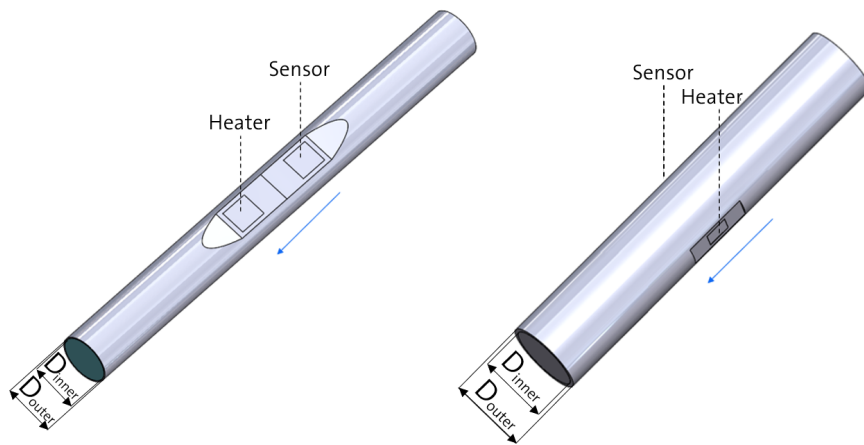


**Figure 2.4** | Different designs of sensor modules with an indication of placement of heater and sensor as well as visualization of diameter reference. The blue arrow indicates the flow direction.

At each indicated spot on figure 2.4 for the heater and the sensor, wires were attached, which were coupled with the data logger via a circuit board. For a picture of the comparison of the two sensor design types, see appendix A. Attached to the sensor module were clear polyurethane tubings with diameters corresponding to the sensor module in use.

### Flow Demo Board

The electronic components of the setup were connected via a printed circuit board, referred to as the flow demo board. The thermal mass flow sensor module was connected to terminals on the board as visualized in figure 2.5. The heater wires are connected at the 'H' terminals and the temperature sensor to terminals labeled 'S'. Lastly, the flow demo board was connected to a power supply which was, according to the available data sheet for the sensor, set to apply a voltage of +15 V.

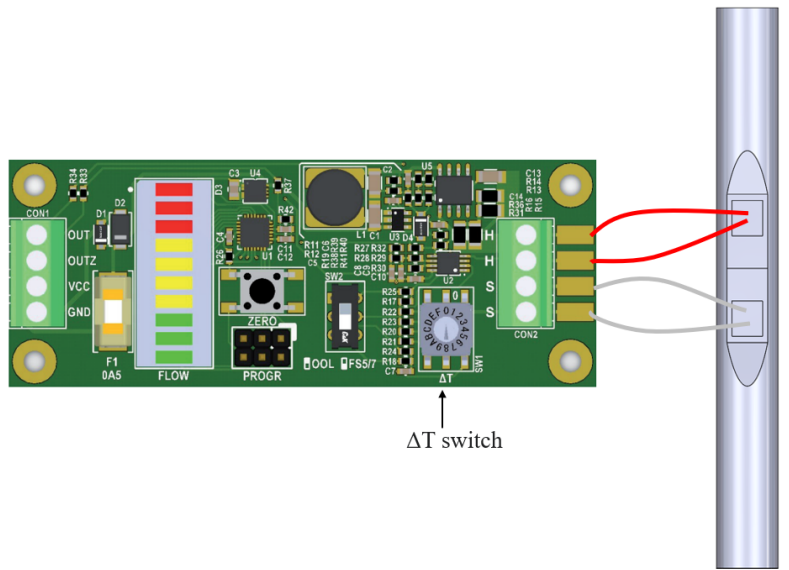


**Figure 2.5 | Sensor module connected to flow demo board [10].** The blue arrow indicates the flow direction.

The available temperature difference,  $\Delta T$ , settings were visible on the backside of the flow demo board as illustrated in figure 2.6. Dealing with the OOL sensor module, the OOL reference for the temperature difference table on the backside of the flow demo board was considered. The temperature difference was set by manually turning the  $\Delta T$  switch, indicated in figure 2.5.

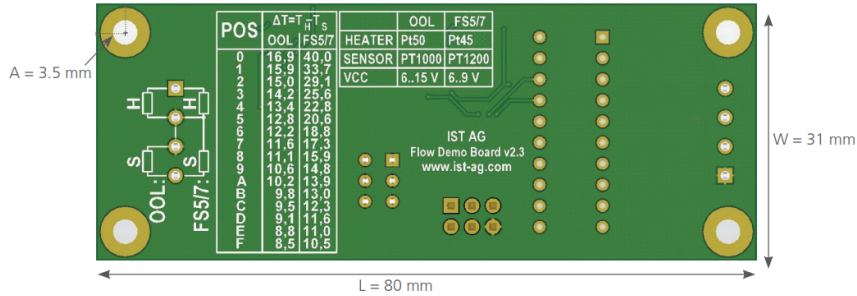


**Figure 2.6 | Back side of flow demo board [10].**

The 16 temperature difference settings available ranged from a difference of  $16.5^{\circ}\text{C}$  at maximum to a difference of  $8.5^{\circ}\text{C}$  at minimum.

The working principle of the flow demo board is covered in section 1.2.

## Logger and Voltage Source

Attached to the flow demo board were both a data logger and a voltage source. The data logger, a multiplexer device, was of the Agilent 34970A Data Acquisition/Switch Unit Family which measured the signals of voltage and resistance from the sensor module. Coupled with a PC, the logger was set to measure in specified time intervals with a certain amount of measurements per second. The voltage source was a Bang & Olufsen's Power Supply SN16A.

## Alpha2 Pump

For the recirculation of water from tank 2 to tank 1, in reference to figure 2.1, an Alpha2 pump from Grundfos with a maximum flow of  $4 \text{ m}^3/\text{h}$  was utilized.

## Mettler PC16 Weighing Scale

The weighing scale in use was of model type Mettler PC16 scale with a weighing range of 16500 g, a readability of  $0.1 \text{ g}$ , a linearity of  $0.2 \text{ g}$ , and a reproducibility of  $0.1 \text{ g}$ . The scale furthermore had a result deviation of  $\pm 0.2 \text{ g}$  [14].

The scale was used to log the weight of water versus time for the derivation of the mass flow of each experiment. Prior to operation, the Mettler weighing scale was assured placement on a stable support, i.e. on a table, and further setup including the adjustment of two leveling feet such that an air bubble in the level indicator on the front of the weighing scale was visually centralized.

## Uncertainty Analysis

The consideration of uncertainties in the testing equipment is of great importance as it gives insight into the accuracy and reliability of the measurements. It is also important to recognize the role of uncertainties in the calibration and validation of results. To calculate the uncertainty of the scale measurements the root-sum-of-squares method is utilized as expressed in equation 2.5 For the analysis of the weight measurements the result deviation, reproducibility, and linearity of the PC16 Mettler scale provided in [14] is used

$$\sigma_{scale} = \sqrt{(0.1g)^2 + (0.2g)^2 + (0.2g)^2} = 0.3g. \quad (2.1)$$

As such the measurements have an uncertainty of  $\pm 0.3g$ . Multiplying this result with a coverage factor of  $k = 2$  gives the result a confidence level of 95%. This would give an expanded uncertainty of  $\pm 0.6g$ . It should be noted that the uncertainty factors are assumed to be independent and that the uncertainties follow a normal distribution. The mentioned factors should be independent but a nonlinear response of the scale could affect the result deviation and as such not be entirely independent.

For the utilized power supply of the Bang & Olufsen SN16A model, the stated accuracy of measurement, as stated by the manufacturer, is  $\pm 2\%$  at full deflection [2].

These uncertainties potentially affect the raw experimental data, from which several parameters of interest are deduced. The uncertainty of the scale affects the derivation of the mass flow from which quantities such as Reynolds number, and thus the state of flow, are derived. The uncertainty in the power supply could potentially affect the output voltage from the sensor, thus inducing potential instability in the response.

### 2.1.3 | Experimental Areas of Investigation

A change in the diameter size of the sensor modules was investigated, as this indicated the scalability of the sensor. As three sensor module sizes were available, these were the possible geometrical variances. Moreover, the time-sensitivity of each sensor module was of interest, to explore possible differences in the stabilization time of the output of sensors with changing diameters.

Another investigated parameter was the temperature difference,  $\Delta T$ , the sensor module was to uphold between the heater and the sensor. The sensor module was to handle a maximum of five varying temperature differences across the available settings. Ranging between high- and low-temperature differences, it was of interest to investigate the potential effect a change in temperature setting had on the sensor response.

Additionally, a change in the alteration of mass flow was investigated. The impact of this parameter was examined across seven different valve settings corresponding to seven distinct mass flows. The valve settings were manually incrementally changed prior to data collection. Obtaining the mass flows would allow for derivations of flow properties used in the further analysis of the fluid behavior. Evaluating the sensor modules' stability of operation across differing flow velocities was of interest in the investigation of the sensor modules' most ideal operating range. Moreover, as a test of the sensitivity of the sensor, bends were introduced along the flow path as part of the investigation. The setup was similar to that visualized in figure 2.1, however with a different setup between the valve and the outlet tank, tank 3. Two bends, neighboring the sensor, were placed as illustrated in figure 2.7.

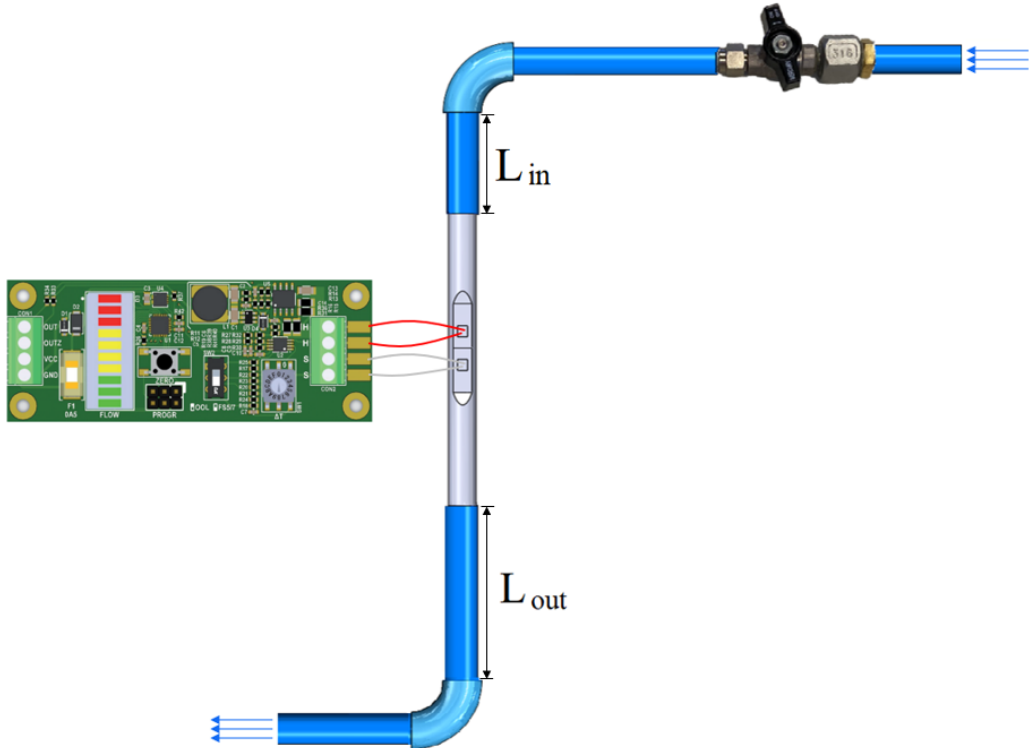


**Figure 2.7 | Visualization of bends in the experimental setup. The blue arrows indicate the flow direction.**

For the testing of the bends, a variation in mass flow was investigated, by altering the valve setting, ranging, this time, only between two settings; one aimed to be a lower-velocity flow and another, a higher-velocity flow. Besides also varying the temperature difference setting from a high difference to a low difference, the orientation of the sensor was also investigated. The introduction of bends was expected to affect the flow velocity past the bend as indicated in figure 2.8.

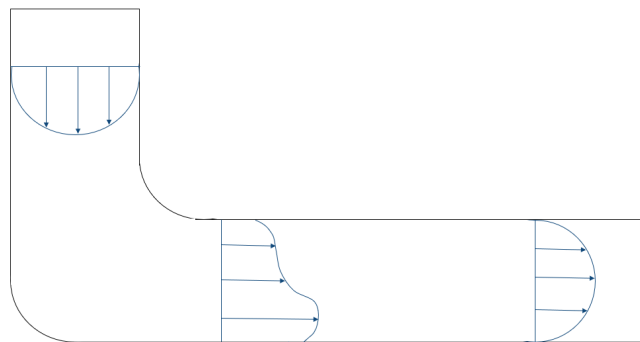


**Figure 2.8 | Illustration of expected velocity flow profiles through the bend.**

As it was expected for the velocity to increase at the outer part of the bend and decrease at the inner section, four orientations of the sensor were tested, numbered 1 through 4 in reference to the illustration in figure 2.9 with the depicted orientation at position 2.

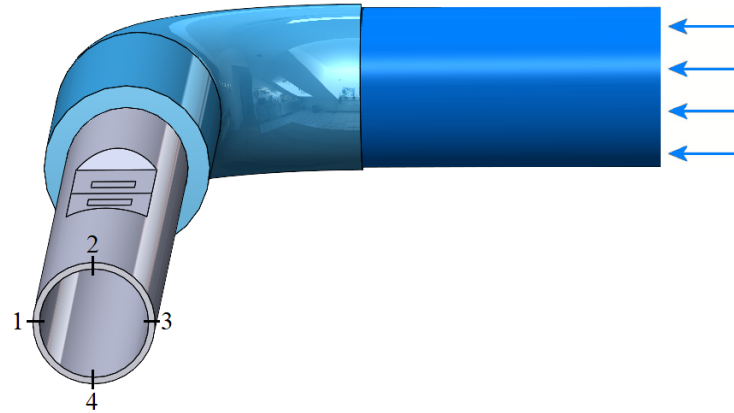


**Figure 2.9 | Illustration of orientations with the sensor module at position 2. The blue arrows indicate the flow direction.**

Additionally, for the investigation of bends in the setup, the length of pipe between the first bend met by the flow and the sensor module was altered to investigate if this parameter had an effect on the stability of the sensor output. This could also indicate if the sensor module was to be set up with bends, at what distance away from the bend it would have the best operation.

Finally, the sensitivity of the sensor module was evaluated by the introduction of externally forced convection applied directly to the sensor module. The effect of external factors such as applying a wind-like effect by blowing cool air from a hairdryer directly aimed at the sensor module was investigated. In the same respect, the effectiveness of insulation would be explored when the sensor module was affected by the externally applied forced convection. With two insulation types available, it was of interest to investigate the difference the externally applied forced convection would have on a non-insulated sensor module as opposed to an insulated sensor module. The insulation was varied in thickness, between two different insulation thicknesses, and in coverage, differing between insulation covering just the sensor module and one covering some length of the neighboring piping.

## 2.1.4 | Experimental Execution

Prior to the experimental execution, the Alpha2 pump was activated. Once engaged, a run-in-time was necessary to secure the water level in tank 2 had reached an equilibrium. Such equilibrium was achieved once the water level had risen just above the pipe feeding back to tank 2. At this point, the water being pumped into tank 1, would not exceed the water being funneled back to tank 2. As such a loop had been created, a constant water level in tank 1 had been ensured and, thereby, a constant pressure at the valve was secured for the investigation. The maximum flow of the pump provided an upper limit to the mass flow allowed through the valve and into tank 3. If a mass flow exceeding  $4 \text{ m}^3/\text{h}$  was achieved in tank 3, the water level in tank 2 would begin to fall, which would result in a difference in pressure at the valve. This in turn would result in a varying flow through the sensor.

The first set of experiments was conducted according to the setup of figure 2.1, with changing parameters of sensor module diameter, temperature difference, and valve setting. The sensor module sizes altered between those described in section 2.1.2, whereas the valve setting, controlling the investigated mass flow, along with the temperature difference setting, was to be set manually. Ensuring, visually, no air bubbles in the pipes, the smallest valve setting for each variation in sensor module size was aimed to be only a dribble, whereas the largest valve setting was set by an almost fully opened valve. The remaining five settings were set in between these. In terms of the temperature difference settings, the flow demo board had 16 available settings on the  $\Delta T$  switch, however, a maximum of five settings were investigated.

The temperature difference settings used during the experiments are presented in table 2.1, with position and the corresponding temperature difference to be held between the heater and the sensor.

Position	$\Delta T$
1	15.9°C
4	13.4°C
8	11.1°C
C	9.5°C
F	8.5°C

**Table 2.1 | Table of used flow demo board settings and the corresponding temperature differences.**

All five settings were used for the two smallest sensor modules with diameters  $D_1$  and  $D_2$ . For the largest sensor module of diameter  $D_3$ , three settings were used, namely  $\Delta T = 15.9^\circ\text{C}$ ,  $\Delta T = 11.1^\circ\text{C}$ , and  $\Delta T = 8.5^\circ\text{C}$ .

For the execution of the investigation, the sensor module of interest was mounted and a temperature difference was selected, whereupon the switch in valve settings would take place. Upon having investigated all valve settings, the temperature difference was altered and the change of the valve settings was repeated.

For each valve setting, the mass flow was found manually, as read off the weighing scale on which the outlet tank was placed. Prior to data logging, the mass flow was found for each valve setting by video-recording the weighing progress across one minute, from which the weight was documented in one-second intervals.

The second set of experiments focused on the effect of the inlet conditions on the sensor stability, which was conducted only on the second largest sensor module size,  $D_2$ . Prior to the introduction of the two bends neighboring the sensor, it was investigated whether the orientation of the sensor affected the output voltage when placed in the simple, straight-pipe setup. This was done in four increments, by manually twisting the sensor module in positions according to the illustration of figure 2.9. In a similar manner, the testing of the bends was conducted. The length of the pipe between the first bend and the sensor module was altered prior to data collection, between lengths of 22 mm, 43.5 mm, and 200 mm.

Finally, for the execution of the externally applied forced convection experiments, the sensor module of size  $D_2$  was used with a temperature difference set to switch between two  $\Delta T$ 's, namely  $\Delta T = 15.9^\circ\text{C}$  and  $\Delta T = 8.5^\circ\text{C}$ . In order to see the immediate effect the application of the forced convection had on the sensor module output, data collection was initialized prior to the application of external forced convection which was then applied after a short delay of 1 minute. After application, while still collecting data, the externally applied forced convection was removed to investigate the settling time of the sensor module post-application. The insulation experiments following the externally applied forced convection experiments were conducted on a set constant temperature difference setting of  $\Delta T = 15.9^\circ\text{C}$ , again utilizing the sensor module of size  $D_2$ . Applying first a thin layer of insulation of thickness 3.5 mm and length 46 mm, covering only the sensor module, the forced convection was applied with the cool air from the hairdryer. Thereafter, was the insulation with a thickness of 11 mm investigated, first with a length of 35.7 mm, again covering only the sensor module, and secondly with a length of 232 mm, covering the sensor module and neighboring pipes. The application of the thicker insulation of altering lengths is pictured in figure 2.10.

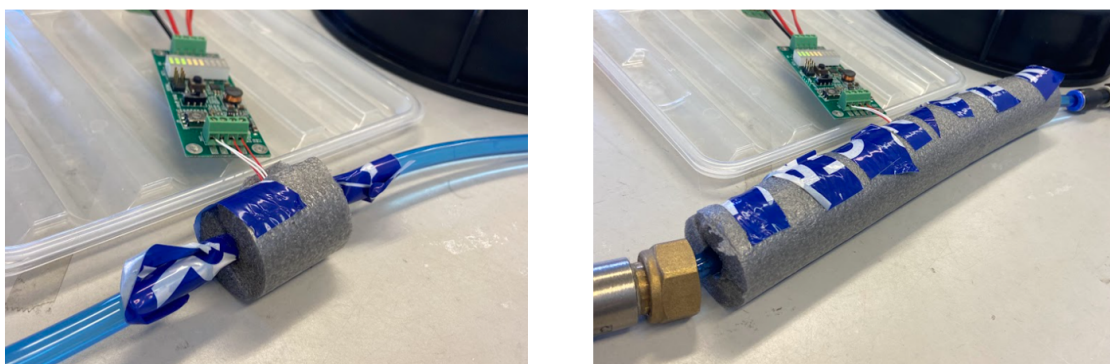


**Figure 2.10 | Insulation layers with a thickness of 11 mm and alternating lengths. Left: insulation layer with a length of 35.7 mm. Right: insulation layer with a length of 232 mm.**

As visible in figure 2.10, the insulation layers were fastened with tape to ensure closed insulation.

## 2.1.5 | Experimental Considerations

Concerning the experimental setup, the iST thermal mass flow sensor was intentionally installed a length away from the closest valve to ensure a laminar, fully developed flow reaching the sensor at low velocities as described in section 2.2.1. Although the valve settings were altered, this length remained unchanged for the experiments as the performance of the sensor in a turbulent flow was also desired to be investigated.

Experimentally, the sensor output voltage and temperature resistances were extracted by use of the data logger. Initially handling only one measurement per second, the data logger was later set to measure twice per second to strengthen the precision of later analysis.

Additionally, for the experiments concerning the largest sensor module size, it became necessary to replace the valve otherwise used for the smallest and the second-largest sensor module size. The replacement happened as the pipe fitting the largest sensor size was too large for the previously used valve. The effect of the replacement is unknown but should be considered in the analysis and comparison of data from the different sensor module sizes. Furthermore, it was found, for the largest sensor module diameter,  $D_3$ , that the seventh, and largest, valve setting was too great for the system, as the Alpha2 pump was unable to keep up with the rapid outflow of tank 1. It was, thus, decided to settle at only six valve settings when handling the investigation of the largest sensor module diameter.

Additionally, the derivation of the mass flows was based on data from two 15-second intervals of the one-minute video recording of the weighing scale, as these were decided as representative for an estimation of the considered mass flow.

## 2.1.6 | Statistics

For handling data that fluctuates over time, as is the case with the velocity and voltage measurements, the mean of the data is preferably handled to ease the analysis. The mean value is found using

$$\bar{x} = \frac{1}{n} \sum_{i=1}^n x_i, \quad (2.2)$$

in which all data is summed over the total amount,  $n$ , of considered values,  $x_i$ .

Although handling relatively large data sets, the mean value can, potentially, be affected by measurements differing significantly from expected values. Thus, it is convenient to describe the spread of the observations to find if the flow acts unexpectedly or inconsistently. To describe the spread of the observations, the measure of variance is used, as expressed by

$$s^2 = \frac{1}{n-1} \sum_{i=1}^n (x_i - \bar{x})^2. \quad (2.3)$$

The variance is, essentially, the mean distance from the average value squared. Taking the square root of the variance gives the standard deviation, as described by

$$s = \sqrt{\frac{1}{n-1} \sum_{i=1}^n (x_i - \bar{x})^2}, \quad (2.4)$$

which is then the mean distance to the average.

Another statistical tool used is the root sum of squares

$$\sigma = \sqrt{\sum_{i=1}^n (y_i - \hat{y})^2}, \quad (2.5)$$

used to calculate the compiled uncertainty. Furthermore,  $R^2$ , also named the coefficient of determination, is a statistic used to determine how well a model fits a set of data. It can be calculated using the sum of squares of residuals, and the total sum of squares, TSS:

$$R^2 = 1 - \frac{RSS}{TSS} = 1 - \frac{\sum_{i=1}^n (y_i - \hat{y})^2}{\sum_{i=1}^n (y_i - \bar{y})^2} \quad (2.6)$$

Where  $\hat{y}$  represents the estimated values using the regression, the data is desired to be fitted against.  $R^2$  is a number between 0 and 1, where 1 indicates a perfect fit [13].

## 2.1.7 | Derivation of Mass Flow

The first set of experiments was, among others, focused on acquiring a relation between the mass flow and the output voltage of the sensor. From a 1-minute video recording, two sets of 15-second intervals were investigated to document the increasing weight in 1-second intervals. In the comparison of each data point of the increased weight, the change in weight over 1 second could be recorded in the unit of g/s. In order to find an estimated mass flow at each new valve setting, the statistical mean value was found. Thus, for deriving the mass flow, the two sets of 15 data points recorded the change of mass over time, were averaged in order to find an estimate for the entire mass flow.

This derived mass flow could then be utilized to find the volume flow rate by dividing the mean mass flow rate by the density of water of  $\rho = 998 \text{ kg/m}^3$  (at 20°C), arriving at a volume flow rate,  $\dot{Q}$ , with units of  $\text{m}^3/\text{s}$ . From the volume flow rate, via multiplication of the cross-sectional area of the sensor, the velocity of the flow could be derived. These properties for each experiment were documented and utilized in further analysis.

## 2.1.8 | Data Analysis of Voltage Time Series

The duration of the experiments was set in accordance with the relevant parameter of interest. Each collection of data lasted between 5 and 15 minutes, from which data sets were extracted in 60-second intervals. This enabled statistical data analysis and comparison across the data sets.

# 2.2 | Numerical Study

For the examination of the sensor, it was highly relevant to investigate the sensor's response to different behaviors of the passing fluid. It is, thus, necessary to specify the state of fluid flow that the sensor experiences. During the experiments, parameters such as geometry, mass flow, temperature, and boundary conditions were altered and this section delves into the effects these alterations have on the fluid flow. Furthermore, in order to get a sense of the behavior of the sensor module's output and the behavior of the fluid flowing through the module, a CFD simulation was conducted and elaborated upon at the end of this section.

## 2.2.1 | Governing Equations of Fluid

As the investigated flow was confined to a pipe, it falls within the category of an internal flow. Internal flows are classified by being completely bounded by solid surfaces and, as such, the flow field is dominated by the influence of viscosity. Considering a fluid entering a pipe with a uniform velocity, the fluid particles coming in contact with the wall will come to a complete stop due to the no-slip condition. This layer of particles will cause the adjacent layer to slow down due to friction which will, in turn, affect the next layer of particles, continually increasing the thickness of the layer of particles along the flow direction. This layer of slower-moving particles is called the velocity boundary layer, in which friction is significant. The viscous forces create a velocity gradient and, thus, a velocity profile across the pipe diameter [16]. The same can be said for a fluid with a uniform temperature, entering a pipe with a specified surface temperature. The particles coming in contact with the surface will reach the surface temperature through conduction. The thermal boundary layer will, in this case, then affect the convection throughout the fluid, causing a temperature gradient [4].

In the classification of fluid flows, the property of compressibility comes of relevance in the analysis thereof. Depending on the density variation during flow, a flow can be categorized as either compressible or incompressible [4]. For a flow to be classified as incompressible, the density thereof must remain constant in any infinitesimal volume of fluid throughout the flow. Typically, the flow of liquids, as the one investigated in this report, is said to be incompressible as the densities thereof are essentially constant and change only very little in response to pressure and temperature changes.

## State of Flow

When observing flow at low velocities, the fluid particles will behave very orderly and streamlined. However, once the velocity is increased above a critical value, the flow suddenly becomes chaotic and unpredictable. The characterization of these behaviors is called laminar and turbulent flow, respectively. These behaviors are visualized in figure 2.11 in which the order of the streamlines is illustrated along with the resultant mean velocity profile for both types of flow profiles.

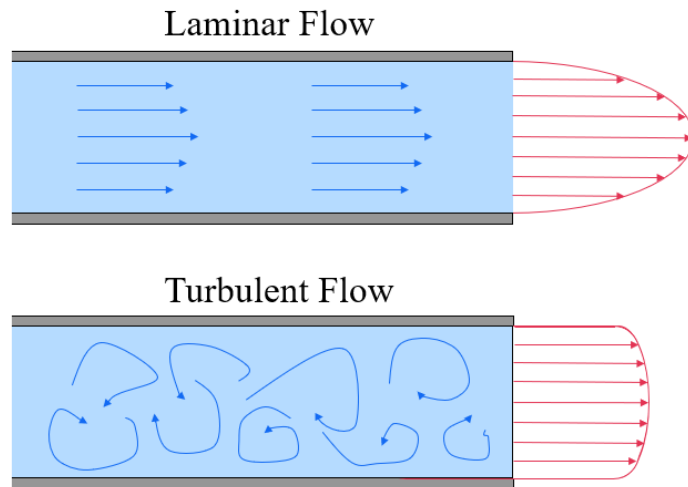


**Figure 2.11 | Flow profiles of laminar flow and turbulent flow.**

Laminar flows are characterized by smooth streamlines and very ordered motion, which is easy to predict [4]. These flows are found in fluids moving at low velocities or, conversely, in fluids with high viscosity. The ordered motion found in these flows allows for analytical analysis, enabling findings of expressions for velocity profiles, shear stresses, pressure drops, and several other interesting derivations. Additionally, a laminar flow is the only flow that can be characterized as steady [20]. A steady flow is characterized by an independence of time. This means that the fluid properties can change from one point to another within the flow, but at a fixed point the properties stay constant. Turbulent flows are, conversely, characterized by very disordered motion and velocity fluctuations. Turbulence is chaotic and, as such, analytically analyzing these flows is not possible as the fluid constantly behaves differently, i.e. unsteadily. Rapid fluctuations of swirling regions of fluid, known as eddies, are generated in turbulent flow, mixing the fluid throughout the profile, which, among others, affects the convection of the fluid, as further elaborated later on.

Various methods can be utilized for analyzing fluid flows, such as simulations and deriving relations from experimental data. It is, however, necessary to determine whether one is dealing with laminar or turbulent flow prior to the calculations, in order to utilize these methods. The estimation of the flow regime a certain flow is contained within has found widespread appliance. This method is based on the Reynolds number expressed by

$$\text{Re} = \frac{\rho U D_h}{\mu} = \frac{U D_h}{\nu}, \quad (2.7)$$

where  $\mu$  and  $\nu$  describe the dynamic viscosity and kinematic viscosity, respectively,  $U$  describes the velocity of the flow and  $D_h$  describes the hydraulic diameter which is given by the area and wetted perimeter:

$$D_h = \frac{4A}{P}. \quad (2.8)$$

For the investigation of the sensor module, the Reynolds number was derived with the kinematic viscosity of water as set at  $\nu = 1.01 \cdot 10^{-6} \text{ m}^2 \text{ s}^{-1}$ . The dimensionless value of equation 2.7 gives an estimate of how the flow behaves, as a Reynolds number of  $2300 < \text{Re}$  constitutes a turbulent flow for pipe flow. The calculation of the Reynolds number also shows how a change in geometry and mass flow can affect the fluid flow.

It is important to note, that the transition from laminar to turbulent flow does not occur suddenly, but rather over a transition region. If a flow is developing, it is called a transient flow. A transient flow describes a flow becoming either fully turbulent, hydrodynamically fully developed, thermally fully developed, steady, etc. A transient flow is therefore never independent of time [16].

## Entry Length & Fully Developed Flow

As earlier described, the boundary layer will increase in thickness along the flow direction, creating a velocity/temperature gradient across the pipe diameter. For the dynamical analysis, once the boundary layer has reached maximum thickness, the fluid particles will no longer experience changing viscous forces, and, as such, the velocity of the particles will stay constant. This means the velocity profile will become independent of distance in the flow direction, which is termed a hydrodynamically fully developed flow. For the thermal analysis, once the boundary layer has reached maximum thickness, the fluid particles will no longer experience changing temperature differences, and the relative temperature of the particles will become constant, as will the temperature profile. This is called a

thermally fully developed flow. If a flow is both fully developed hydrodynamically and thermally, the flow can simply be said to be fully developed. At the beginning of the flow, there will as such be an entrance region in which the flow is transient. The entry length describes the distance from the pipe inlet to the end of the entrance region, at which point the flow has become fully developed. The entry length is dependent on the state of the flow whereas in laminar flows the hydrodynamic and thermal entry length can be calculated by equation 2.9

$$L_{h,laminar} = 0.05\text{Re}D, \quad L_{t,laminar} = 0.05\text{Pr}\text{Re}D = \text{Pr}L_{h,laminar}. \quad (2.9)$$

Here  $\text{Pr}$  describes the dimensionless Prandtl number. In turbulent flows the mixing of the fluid due to eddies and fluctuations overshadows the heat transfer due to molecular diffusion. Therefore the thermal entry length becomes approximately equal to the hydrodynamic entry length, which can be calculated by equation 2.10

$$L_{h,turbulent} \approx L_{t,turbulent} \approx 10D. \quad (2.10)$$

These equations also illustrate how the thermal analysis is affected by the flow regime as well as the pipe geometry.

## Navier-Stokes Equations

In order to obtain detailed descriptions of the happenings in fluid flow, it is essential to consider differential forms of equations of fluid motion. Of particular interest, is the Navier-Stokes equations, which are derived from the application of Newton's second law to an infinitesimal fluid element.

The body and surface forces acting on the individual infinitesimal fluid particle are accounted for when considering Newton's second law and expressions can be derived for each direction component of the total force. These expressions are referred to as the momentum equations [16]. The momentum equations are expressed in terms of central stresses on each side of the infinitesimal element considered. However, as it is of interest to obtain knowledge of fluid motion, it is relevant to consider suitable expressions for the stresses in terms of velocity and pressure fields. Introducing these expressions, along with the assumption of an incompressible flow with constant viscosity, the Navier-Stokes equations are defined by

$$\rho \frac{\partial \vec{U}}{\partial t} = \rho \vec{g} - \nabla p + \mu \nabla^2 \vec{U}, \quad (2.11)$$

with the velocities expressed in vector form as corresponding to

$$\vec{U} = \begin{bmatrix} u \\ v \\ w \end{bmatrix}. \quad (2.12)$$

Equation 2.11, along with the continuity equation expressed by

$$\frac{\partial u}{\partial x} + \frac{\partial v}{\partial y} + \frac{\partial w}{\partial z} = \nabla \cdot \vec{U} = 0, \quad (2.13)$$

form a set of coupled equations that describe many common flows with the only restriction that the fluid be Newtonian, i.e. with constant viscosity, and incompressible [16].

For other than most basic cases, these equations are impossible to solve analytically, thus it is ideal to resort to computational fluid dynamics computer applications for handling the Navier-Stokes equations for more complicated, real-world problems.

## Reynolds-Averaged Navier-Stokes Equations

When it comes to the modeling of more complex, turbulent fluid flows, it is necessary to consider a moderation of the Navier-Stokes equations as these, in their original form, present no exact solution to such complex flows. Due to the nature of turbulent flows, it is not possible to perfectly represent the effects of turbulence, so a turbulence model is considered instead. It is apparent that eddies in turbulent flows cause significant fluctuations in the velocity of the flow. It is, however, such that for most turbulence problems, knowing the time-averaged velocity, along with the intensity of the turbulent fluctuations, is sufficient to model the turbulence.

As it, upon further analysis, becomes apparent, the instantaneous velocity, e.g. in the  $x$  direction,  $u$ , of the flow fluctuates about an average value, why it is concluded that the velocity can be expressed as the sum of an average value  $\bar{u}$  and a fluctuating component  $u'$ , i.e.

$$u = \bar{u} + u', \quad (2.14)$$

which is known as the Reynolds Decomposition. Equation 2.14 holds such that the time-averaged fluctuating velocity must be zero, i.e.  $\bar{u}' = 0$ . The Reynolds decomposed velocity vector yields

$$\vec{U} = \begin{bmatrix} u \\ v \\ w \end{bmatrix} = \begin{bmatrix} \bar{u} + u' \\ \bar{v} + v' \\ \bar{w} + w' \end{bmatrix}. \quad (2.15)$$

Time averaging the incompressible Navier-Stokes equations, equations 2.11 and 2.13, gives the Reynolds averaged Navier-Stokes, RANS, equations expressed by

$$\nabla \cdot \vec{\bar{U}} = 0, \quad (2.16)$$

and

$$\rho \frac{\partial \vec{\bar{U}}}{\partial t} = \rho \vec{g} - \nabla p + \mu \nabla^2 \vec{\bar{U}}, \quad (2.17)$$

From equation 2.17, the Reynolds stress tensor appears which yields  $R_{ij} = \rho u'_i u'_j$ . The most widely used method for handling this stress term is with the Eddy viscosity models [1] for which a turbulent flow characteristic quantity is introduced, namely the Eddy viscosity,  $\mu_t$ . Depending on which turbulence model is utilized for the modeling of the flow, the Eddy viscosity is defined differently. The choice of turbulence model depends on the computational cost per iteration, the user is willing to sacrifice.

## Turbulence Models and Wall-Adjacent Cell Size Estimation

There are many different RANS-based turbulence models, each with its own strengths and weaknesses. A widespread model is the standard  $k-\varepsilon$  model, SKE. Compared to other models it is computationally light, and excels in modeling the middle portion of the flow. It does however have limitations when modelling turbulence near walls. The standard  $k-\omega$  model, SKW, has superior performance at boundary layers compared to SKE but is more computationally heavy. Shear stress transport, SST,  $k-\omega$  model can be seen as a combination between the standard models of  $k-\varepsilon$  and  $k-\omega$  as it uses a blending function to transition from SKW near walls to SKE in the outer portion of the boundary layer.

The wall-adjacent cell size is important for turbulent simulation. This is because the velocity near the wall changes rapidly, as illustrated in figure 2.12 in the region of  $1 \leq y^+ \leq 30$ .

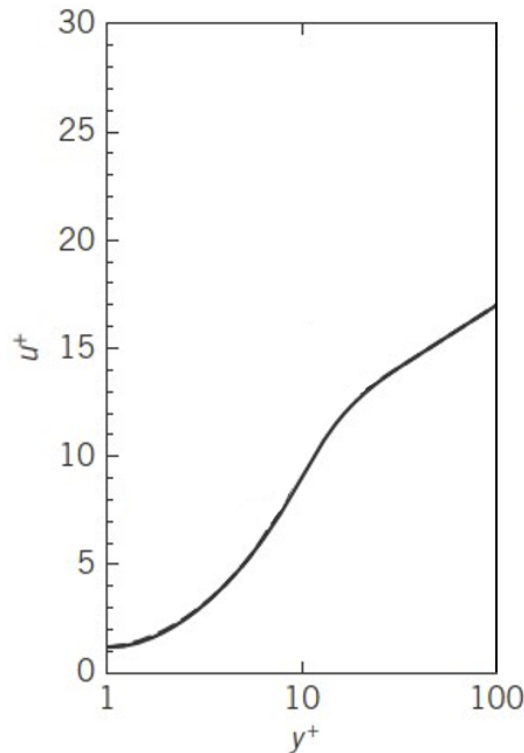


**Figure 2.12** | Dimensionless mean velocity,  $u^+$ , in a pipe for turbulent flow at a dimensionless distance  $y^+$  from the wall [16].

The dimensionless mean velocity depicted in figure 2.12 is given by

$$u^+ = \frac{\bar{U}}{U_\tau}, \quad (2.18)$$

in which  $U_\tau$  is termed the friction velocity and is given by

$$U_\tau = \sqrt{\frac{\tau}{\rho}}. \quad (2.19)$$

In figure 2.12  $y^+$  is a dimensionless wall distance vector and is used in the determination of the size of the first grid point,  $\Delta y$ , as expressed by

$$\Delta y = \frac{y^+ \mu}{U_\tau \rho}. \quad (2.20)$$

Equation 2.20 can be simplified to only rely on  $y^+$  and the components of the Reynolds number by

$$\Delta y \approx 5.06 D_h Re_{d_h}^{-7/8} y^+. \quad (2.21)$$

The derivation of equation 2.21 can be seen in section B.2 in appendix B. Equation 2.21 is the equation used to determine the wall-adjacent cell size.

The proper wall-adjacent cell size depends on the turbulence model. For k- $\omega$  turbulence modeling the size of the first cell needs to be  $y^+ = 1$ . This is necessary in order of resolving the viscous sublayer, which is the region corresponding to  $1 \leq y^+ \leq 30$ , which is closest to the wall and where turbulent friction is considered negligible compared to viscous friction [1] [16].

## 2.2.2 | Heat Transfer

A central aspect of the studied flow sensor is the transfer of heat to the measured fluid. It is, thus, prudent to investigate the effect, changes in thermal properties have on the flow sensor. Heat transfer arises from one, or a combination, of three processes; conduction, convection, and radiation.

Heat transfer aims to describe the flow of heat, through a variety of mediums, including liquids and gasses. The analysis of heat transfer is, consequently, closely related to the analysis of flow, especially when considering convection. Heat transfer, as well as flow, can be characterized as steady or transient, describing time dependency. Steady heat transfer is independent of time and transient, or unsteady, heat transfer is time dependent.

The focus of this section will be on conduction and convection as these are the most relevant processes of heat transfer because radiation is considered negligible for this study.

### Conduction

Conduction is the transfer of heat energy caused by a temperature difference between two adjacent parts in contact in a stationary system. In solids, this process happens through vibrations of molecules in a lattice and energy transported by free electrons. In liquids, it happens due to collisions and diffusion of molecules during their random motion. The rate of heat transfer through a medium is related to the geometry, thickness, and material of the medium along with the temperature difference across the medium given by

$$\dot{Q}_{cond} = kA \frac{T_1 - T_2}{\Delta x} = -kA \frac{\Delta T}{\Delta x}, \quad (2.22)$$

where the rate of heat transfer is represented by  $\dot{Q}_{cond}$ ,  $k$  is the thermal conductivity of the material,  $A$  is the area normal to the heat transfer,  $\Delta T$  is the temperature difference and  $\Delta x$  is the thickness of the medium through which the heat is transferred [4].

### Convection

Convection combines the effects of conduction and fluid motion, as it refers to the energy transfer between a solid surface and the adjacent fluid in motion [4]. Convection can be further classified as either forced convection or natural convection. Additionally, convective heat transfer can be considered as either external or internal convection, classified depending on whether flow over a surface or in a pipe is to be handled.

The rate of convective heat transfer, as described by

$$\dot{Q}_{conv} = hA_s(T_s - T_\infty), \quad (2.23)$$

is defined by the surface area,  $A_s$ , the temperature difference between the surface temperature,  $T_s$ , and the fluid temperature far from the surface,  $T_\infty$ , and, lastly, the convection heat transfer coefficient,  $h$ . The latter of which is

an experimentally determined quantity, dependent on parameters such as surface geometry and properties of the fluid [4].

Convection is, furthermore, dependent on the type of fluid flow, i.e. either laminar or turbulent.

It is of interest to nondimensionalize the heat transfer coefficient, why the dimensionless convection heat transfer coefficient, the Nusselt number, is introduced as defined by equation 2.24. The variable  $k$  is the thermal conductivity and  $L_c$  is the characteristic length of the geometry, which for a pipe is the diameter  $D$ .

$$Nu = \frac{hL_c}{k} \quad (2.24)$$

For convective heat transfer analysis, it's beneficial to consider approximated thermal conditions at the surface of an internal flow in a pipe. One such approximated thermal condition could be one of constant surface heat flux, i.e.

$$\dot{q}_s = h_x(T_s - T_m). \quad (2.25)$$

### Natural Convection

Natural convection is a convective process that occurs due to a naturally occurring buoyancy force that drives the movement of fluid around an object of higher or lower temperature than its surroundings. When an object is of higher temperature the surrounding fluid is heated through conduction and the change in temperature causes a decrease in density of the nearby fluid. The density difference between the adjacent fluid and the fluid further away, causes the fluid to rise, carrying heat away and allowing for a replacement from warmer to cooler air; thereby slowly cooling the object. Similarly for heating a cooler object, where a hotter fluid through conduction will heat the object and due to an increase in density will sink leaving room for new fluid [4].

### Forced convection

Forced convection occurs when a fluid, by external means, is forced to flow within a pipe or over a surface either by use of a pressure gradient or an external force such as a pump or a fan [4]. The convective heat transfer between solid and fluid is enhanced by the forced movement of fluid thus allowing for larger heat transfer.

## 2.2.3 | Numerical Method

Simulations can be used to analyze how a component responds to physical influences. It achieves this by use of finite element analysis, FEA, which when applied to fluid dynamics is frequently called computational fluid dynamics, CFD. Different numerical methods can be used in FEA/CFD to solve a problem. For structural problems, the finite element method, FEM, is often used, whereas for CFD applications the finite volume method, FVM, is common. CFD works by discretizing a component into many small connected components, called cells, which together form a mesh. By solving for each cell the result of the influences can be estimated. How accurate the result is depends on multiple factors, such as how the boundary conditions are applied and how finely the component has been meshed. However, with finer meshing comes a cost of greater computational power, and for this reason, it is valuable to find a mesh that produces sufficiently accurate results, but at the least amount of needed computational power [18] [16]. The CFD analysis utilizes the theory of heat transfer and fluid dynamics as covered in subsections 2.2.1 and 2.2.2.

## CAD Modelling Considerations

The CAD-modelled sensor module was of size D<sub>2</sub> as the experiments thereof encompassed a wider range of velocities. The dimensions of D<sub>2</sub> for the CAD model were measured using a vernier caliper capable of measuring accurately to the nearest 0.05 mm. A visualization of the D<sub>2</sub> CAD model is depicted in figure 2.13.

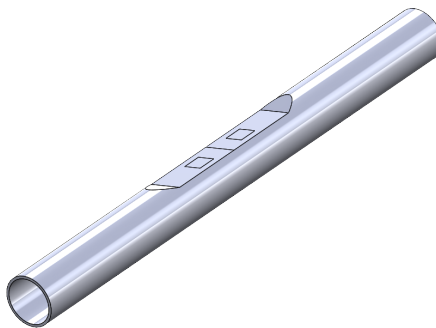


**Figure 2.13 | The CAD-model of  $D_2 = 5.0 \text{ mm}$ .**

The CAD model  $D_2$  was meshed in Ansys using 'Fluent Meshing', which is capable of creating the fluid domain by itself. For this reason, just the walls of the sensor module had to be CAD-modelled. In regard to further analysis, the coordinate system is placed with its origin in the radial center of the inlet cross-section of the sensor module.

## Material Properties

For the simulations, the properties of the water and the steel pipe had to be defined. The properties used can be found in table 2.2.

Material	Density, $\rho$	Specific heat capacity, $c_p$	Thermal conductivity, $k$	Dynamic viscosity, $\mu$
Water	998.2 kg/m <sup>3</sup>	4182 J/(kg · K)	0.6 W/(m · K)	$1.003 \cdot 10^{-3} \text{ kg}/(\text{m} \cdot \text{s})$
Steel	8030 kg/m <sup>3</sup>	502.48 J/(kg · K)	16.27 W/(m · K)	

**Table 2.2 | Properties of water and steel**

The properties are all at 20°C as defined within the Ansys material library. The ambient temperature was 21°C, however, the difference in property values, this difference in temperature causes, are assumed negligible. The properties are used throughout the simulations, as well as for calculations of mass flows and Reynolds numbers.

## Meshing

In general, the different types of 3D elements used for meshing are tetrahedrons, quadrilateral pyramids, triangular prisms, hexahedrons, and polyhedrons. Advantageously, tetrahedrons are easily meshed to complex geometry whereas hexahedrons and prisms are mostly applied to simpler geometries, however with the advantage of offering more accuracy for the same cell count [6]. Another desired property of a mesh is having cells ordered in a logical, uniform pattern. This is referred to as a structured grid, which offers higher resolution compared to an unstructured grid. For the sensor simulations, polyhedrons have largely been used, which much like tetrahedrons, can be easily meshed to complicated geometries, but at a higher accuracy [15].

For fluid dynamic simulations in pipes, it is especially important to consider the mesh at the wall boundary to get proper boundary layer results. For this reason, it is common practice to refine the mesh near the walls, in a process sometimes referred to as inflation. For determining the quality of a mesh different parameters can be considered. One such parameter is called skewness. It quantifies how different a cell's shape is from an equilateral cell of similar volume. It is calculated as

$$\text{Skewness} = \frac{\text{optimal cell size} - \text{cell size}}{\text{optimal cell size}}. \quad (2.26)$$

Skewness is a number between 0 and 1, where a value of 0 indicates the best mesh quality. Generally, the mesh should be improved if the skewness at maximum is above 0.85 or the average skewness is above 0.33 [17].

## Convergence Analysis

One way of finding a sufficient mesh size is by doing a mesh convergence analysis. A common way of performing such analysis is by considering what happens to a parameter when doubling the number of cells in the mesh twice. Doing this, the coarsest investigated mesh would be considered converged if the value of the parameter of interest is within 2% of the value of the same parameter from the finest mesh. For the numerical study of this report, the initial mesh size investigated was the coarsest mesh size available.

To determine convergence, multiple factors must be taken into consideration. An important measure to consider is the residuals, which quantify the error in the solution. In this case, the residuals of mass continuity, energy, and the three components of the velocity, are monitored for laminar simulations, whereas for turbulent simulations the two additional factors ' $k$ ' and ' $\omega$ ' are monitored as well for SST  $k-\omega$  turbulence modeling. A common practice is to ensure the value of the residuals is below  $10^{-5}$  in order of determining convergence. Moreover, it is important to consider the parameters of interest ensuring these are converged. For the performed simulations the values were considered converged once the value did not change more than  $10^{-6}$  over 20 iterations.

## Methodology

In the numerical study of the sensor, it was important to consider what assumptions were appropriate as well as how the boundary conditions were applied. In this case, the simulations were assumed to be steady state, the pressure was assumed to be atmospheric, the gravitational acceleration,  $g$ , was defined to be  $9.81 \text{ m/s}^2$ , and the ambient temperature was set at  $21^\circ\text{C}$ . For the boundary conditions, an inlet velocity determined from the experiments was applied, and the surface of the sensor module was considered to be adiabatic with the exception of the heater surface where a constant heat flux was applied. This heat flux was slightly altered across iterations in order to achieve the set temperature difference between the sensor and the heater. The temperature at the sensor and the heater were determined as an average across the area they span.

For flow rates with Reynolds number below 2300, the flow is assumed to be laminar. For flow rates of Reynolds number above 2300, the flow was modeled using the SST  $k-\omega$  turbulence model. For this turbulence model, the wall-adjacent cell size was calculated using equation 2.21, for two flow velocities above  $\text{Re} = 2300$ , for two different temperature settings, as seen in table 2.3. The hydraulic diameter used for the calculations was derived from the wetted perimeter and area at the cross section at the heater, both deducted from the CAD model. As such the hydraulic diameter was found to yield

$$D_{2h} = \frac{4 \cdot 17.96 \text{ mm}^2}{15.34 \text{ mm}} = 4.68 \text{ mm}. \quad (2.27)$$

The derivation of the Reynolds number, in table 2.3, for each corresponding velocity, was derived by use of equation 2.7 with properties as defined in table 2.2.

Temperature difference	$\Delta T = 8.5^\circ\text{C}$		$\Delta T = 15.9^\circ\text{C}$	
Velocity	0.649 m/s	1.0994 m/s	0.548 m/s	0.8363 m/s
Reynolds number	3022	5120	2552	3895
Wall-adjacent cell size	0.0214 mm	0.0135 mm	0.0249 mm	0.0172 mm

Table 2.3 | Calculated values of wall-adjacent cell sizes.

The mesh utilized for the simulation was created according to the calculated sizes of the first grid point. As such, the four different mesh sizes used for the mesh convergence analysis are visualized in figure 2.14.

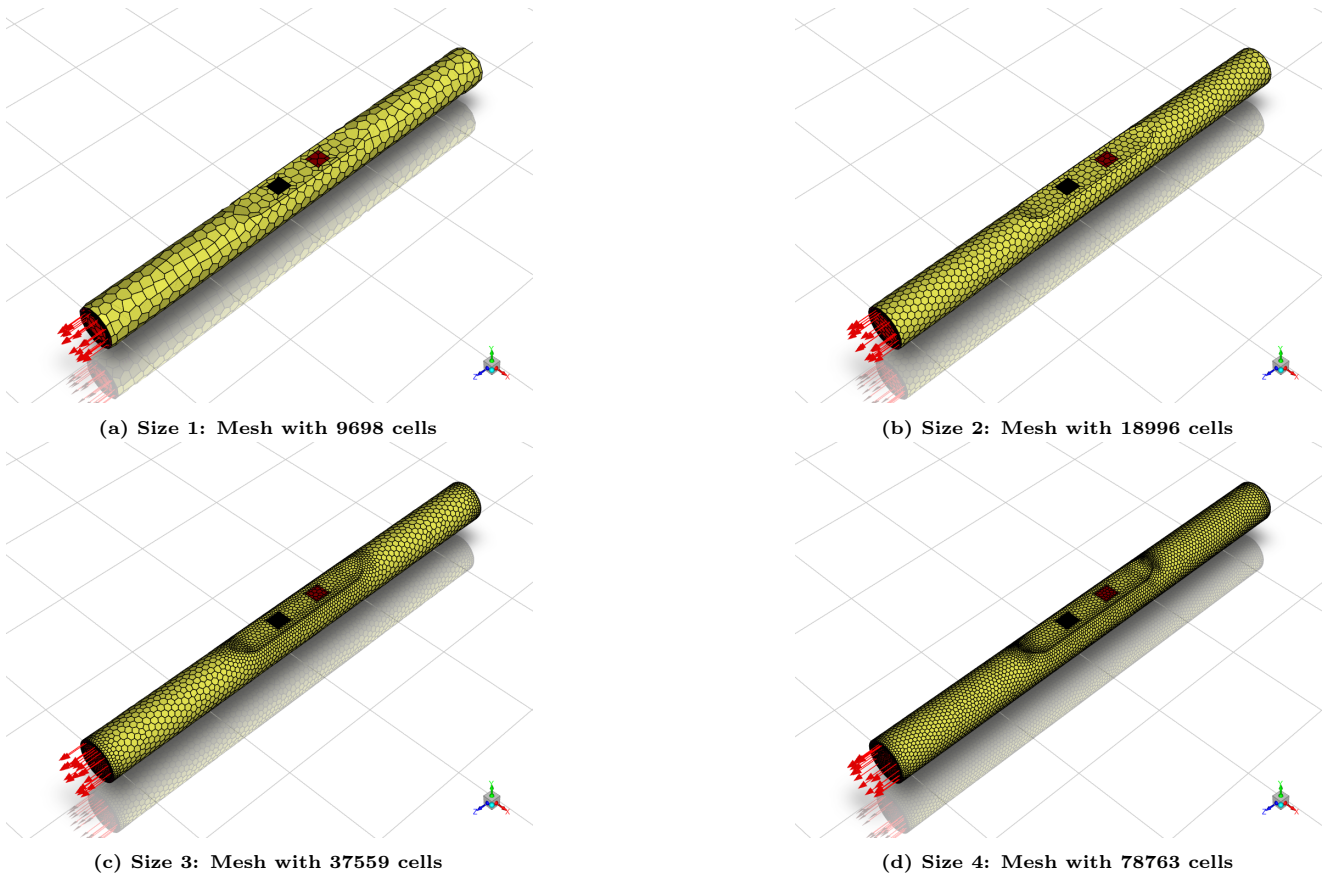


**Figure 2.14 |** The four different mesh sizes used to determine convergence.

The used mesh elements were polyhedrons with hexahedrons at the core of the sensor module. Additionally, all meshes were refined at the boundary between the fluid domain and the steel wall.

For the simulations for each of these mesh sizes, the residuals were monitored and ensured to be below  $10^{-5}$  for both the laminar and turbulent cases as evident in figure 2.15.

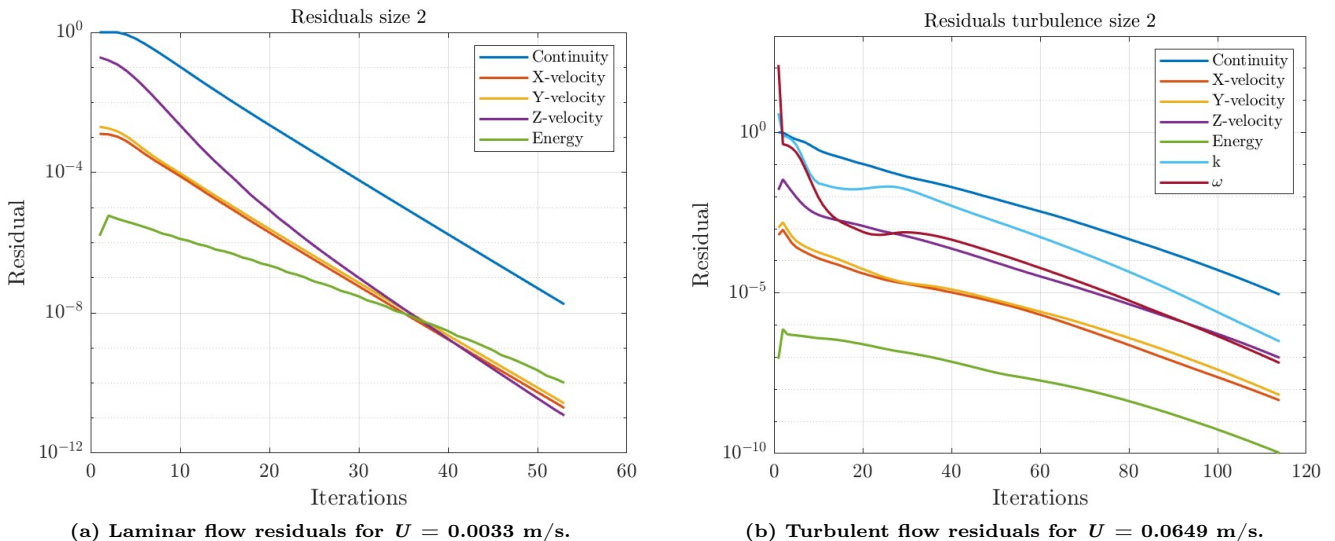


**Figure 2.15 |** Residual plots for  $\Delta T = 15.9^\circ\text{C}$ ,

The residual plot for laminar flows for all mesh sizes in accordance with figure 2.14, can be seen in figure D.2 in appendix D. Moreover, figure 2.16 shows the convergence of the temperature at the heater and the temperature at the sensor, which were created to ensure that the values do not change more than  $10^{-6}$  over 20 iterations.

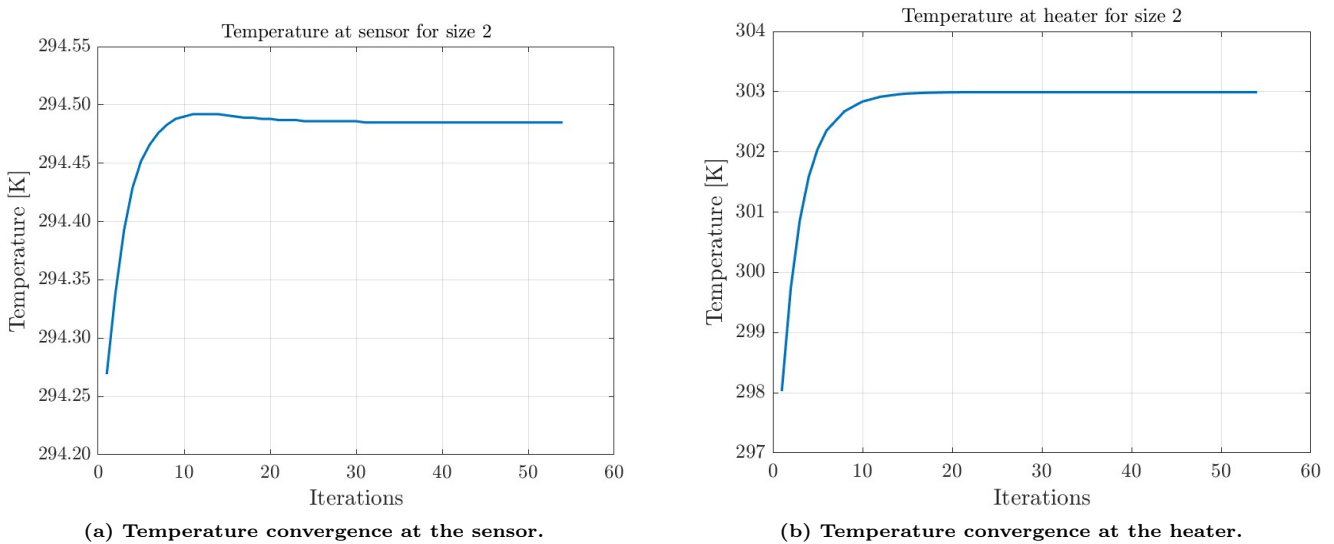


**Figure 2.16** | Convergence for the temperature at heater and sensor for mesh size 2 for  $\Delta T = 15.9^\circ\text{C}$ ,  $U = 0.0033 \text{ m/s}$ .

Additionally, in order of finding the sufficient mesh size, the temperature at a line normal to the heater is shown plotted against the Y-position in figure 2.17. Note that the largest positive value of the Y-position corresponds to the location of the heater.

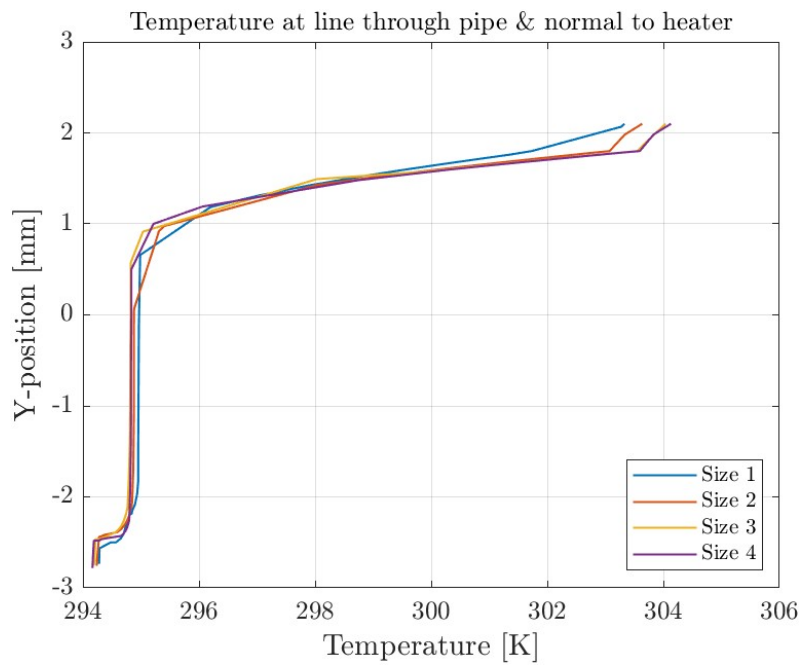


**Figure 2.17** | Line heater for different mesh sizes of  $\Delta T = 15.9^\circ\text{C}$ .

It can be seen that the coarsest size, size 1, deviates from the other mesh sizes as the heater is approached. At the heater, the temperature of size 2 deviates slightly from sizes 3 and 4. However, the temperature of size 2 at the heater leads to an applied heat transfer rate that is within 2% of the applied heat transfer rate of size 4 as seen in figure 2.18.

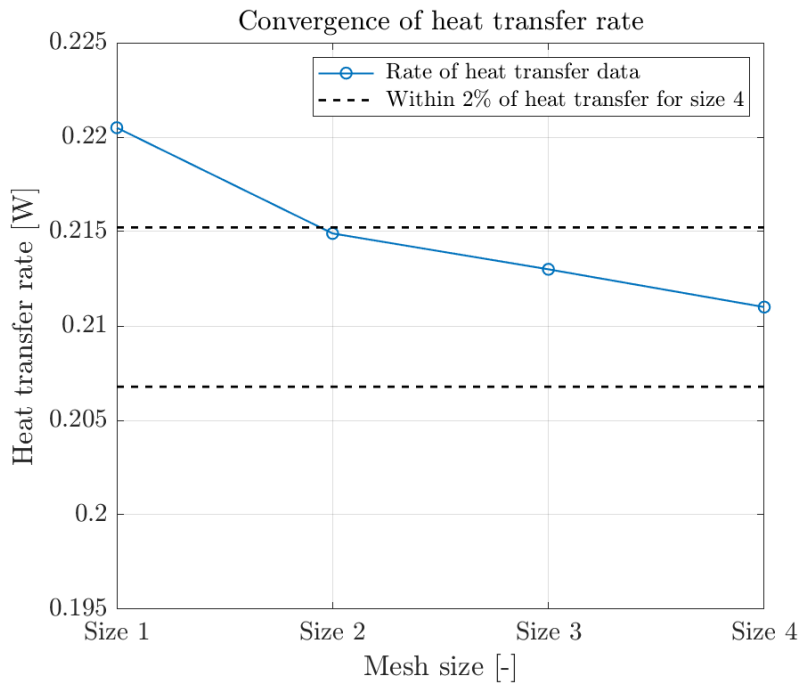


**Figure 2.18 | Convergence of heat transfer rate for  $\Delta T = 15.9^\circ\text{C}$ ,  $U = 0.0033 \text{ m/s}$ .**

For this reason, size 2 can be considered converged and was the chosen mesh size for all simulations. This mesh has a maximum skewness of 0.83 and an average skewness of 0.0937, which indicates that the quality of the mesh is sufficiently good.

A similar mesh convergence analysis is done for the simulations of bends. The convergence of the heat transfer rate for bends can be seen in figure D.5 in appendix D.

## 3 | Results and Discussion

In this chapter, findings from experimental and numerical investigations will be displayed along with a discussion of the results. The results cover the examination of the sensor output through different parameters such as velocity, temperature setting, and sensor geometry. Furthermore, the sensor response to a change in inlet conditions has been investigated along with a change in thermal conditions.

### 3.1 | Voltage Output and Standard Deviation

Initially, in the data collection process, it was of interest to investigate the sensitivity of each sensor in terms of the output response. This was done by use of extended duration tests, with maximum mass flow, initialized immediately after the valve was opened. The response of the sensor module with diameter size  $D_1$ , is graphically visualized in figure 3.1. Similar figures for sensor sizes  $D_2$  and  $D_3$  can be found in figure C.1 in appendix C.

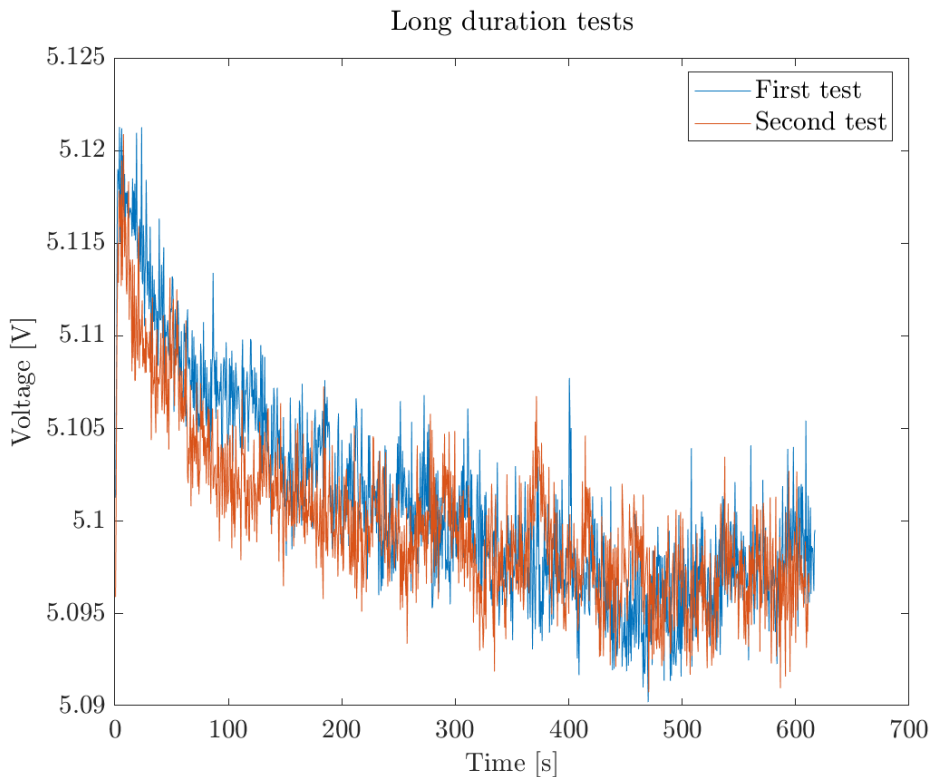


**Figure 3.1 | Two 10 minute tests with similar velocities for  $D_1 = 3.2$  mm.**

From the data, the sensor output was observed to drop significantly in the initial part of the data collection. It was therefore decided to allow the system time to stabilize after the valve was opened. The findings from the extended duration tests were utilized to conclude after which time the output was stable enough to produce usable data for analytical conclusions. For the smallest sensor diameter,  $D_1$ , it was decided that waiting 5 minutes for the three largest velocities was sufficient, whereas for the larger sensor diameter,  $D_2$ , it was found to be 4-6 minutes for all velocities. Lastly, for the largest sensor diameter,  $D_3$ , the time was found to be 10 minutes for all investigated velocities.

Once it was determined when the voltage output had become stable, data collection of voltage output over different mass flows was acquired. The initial experiments were performed using the set-up described in section 2.1.1. The

sensor output voltage produced was relatively stable throughout the different velocities. However, at Reynolds numbers in the transitional region, i.e. at Reynolds numbers between 2000 and 3000, noisier output series were produced as indicated in figure 3.2.

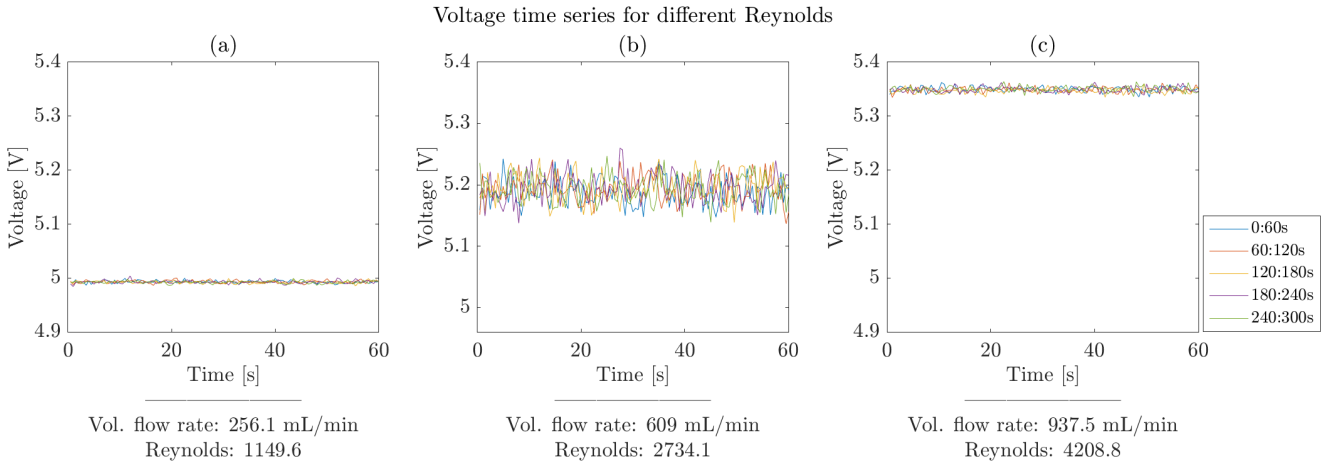


**Figure 3.2 | Voltage time series for  $D_2$  at  $\Delta T = 13.4^\circ\text{C}$ . Reynolds number in the transitional region produces noisier time series.**

The first and third plot presents the voltage outputs, at Reynolds numbers below and above the transitional range. Here the graphs show relatively stable outputs. The second plot shows the output voltage at Reynolds number of  $Re = 2559.1$ , where the results are visibly more fluctuating. The visualized results are from tests performed on the second largest sensor diameter,  $D_2$ , with a temperature setting of  $\Delta T = 13.4^\circ\text{C}$ . Additional graphs of the different output voltages can be seen in appendix C, figure C.2. Subsequently, similar tests were performed on the three different sensor diameters, changing both velocity and temperature settings.

After the first tests, it was possible to determine an average voltage output at each velocity for each temperature setting. These averages have been plotted and King's Law, equation 1.1, has been fitted to the data points as can be seen in figure 3.3. Note that in the process of fitting it was utilized that the  $A$ -coefficient of King's Law was known, as this corresponded to the voltage output when no water was flowing. This voltage is termed the zero-voltage, and the average zero-voltage was found for every temperature setting for both diameters.

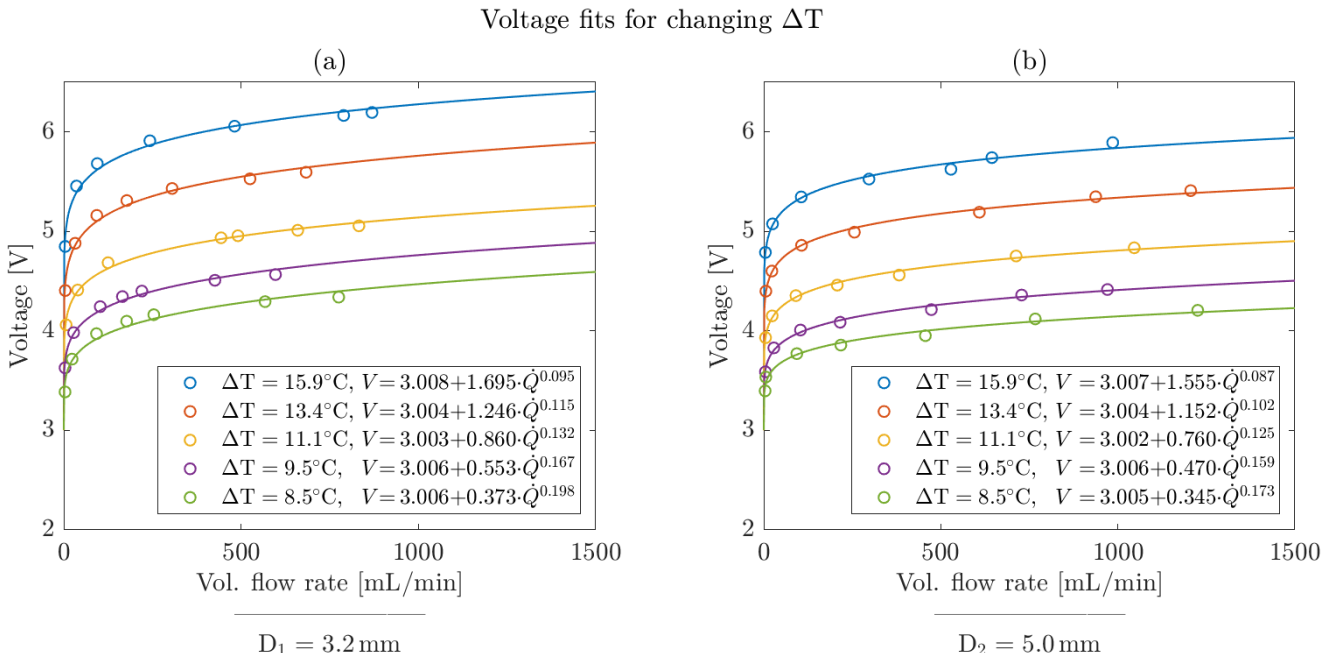


**Figure 3.3 | The experimental results for  $D_1$  and  $D_2$  fitted against King's Law. Note that for the found fits the volume flow rate should be inserted in mL/min.**

For the sensor with diameter,  $D_3$ , only three temperature settings were investigated. The graph showing the voltage fits for  $D_3$  can be seen in figure C.3 in appendix C.

The fits in figure 3.3 constituted a calibration of the sensor in which the parameters  $A$ ,  $B$ , and  $C$  seen in equation 1.1 were determined. All the fits have an  $R^2$ -value above 0.97, indicating an accurate correlation between the fit and the data points. The figure shows a decrease in the average output voltage with a decrease in the temperature difference between the sensor and the heater. Furthermore, the graphs show that the sensor is most sensitive at flow rates below 250 mL/min.

Comparing the results of the two diameters, a significant difference in the average voltages was evident. For the setting  $\Delta T = 15.9^\circ\text{C}$  the sensor with diameter  $D_1$  shows an average voltage of about 3 V at a flow rate of 500 mL/min. At the same setting and flow rate, the average voltage of the sensor with diameter  $D_2$  shows a voltage of about 2.5 V. This difference in velocity is because the fluid must be traveling faster in the smaller pipe to achieve the same volume flow.

In an attempt to create an expression to approximate the experimentally found voltages, MATLAB was used to find an equation that could calculate the voltages given a set temperature difference, a volume flow rate (in mL/min), and a sensor diameter;  $D_1$  or  $D_2$ . To do this it was assumed the voltage could be described as a simplified King's Law,  $V = n \cdot \dot{Q}^m$ , which is a standard power function. This was done out of convenience to limit the number of coefficients that the voltage relies on to two. Firstly fitting  $n$  to as simple an expression as reasonably possible;  $n = c + b \cdot \Delta T + a \cdot D$  yielded an  $R^2$  of 0.9961, and lastly fitting  $m$  to the same expression yielded an  $R^2$  of 0.889. This resulted in equation 3.1

$$V = (1.824 - 28.33D + 0.1793\Delta T) \cdot \dot{Q}^{(0.05963 - 4.679D + 8.553e-05\Delta T)}, \quad (3.1)$$

that does tend to slightly undershoot the experimentally found voltages but is able to approximate with decent precision.

As the graphs presented in figure 3.2 show, the sensor output voltage fluctuated depending on the state of flow. The observed fluctuations were largest at Reynolds numbers of about  $Re = 2300$ . This behavior has been further investigated by calculating the standard deviation of the measured output voltage. The standard deviation has then been deducted and added to the average which has been plotted against the Reynolds numbers. The results of the analysis can be seen in figure 3.4.

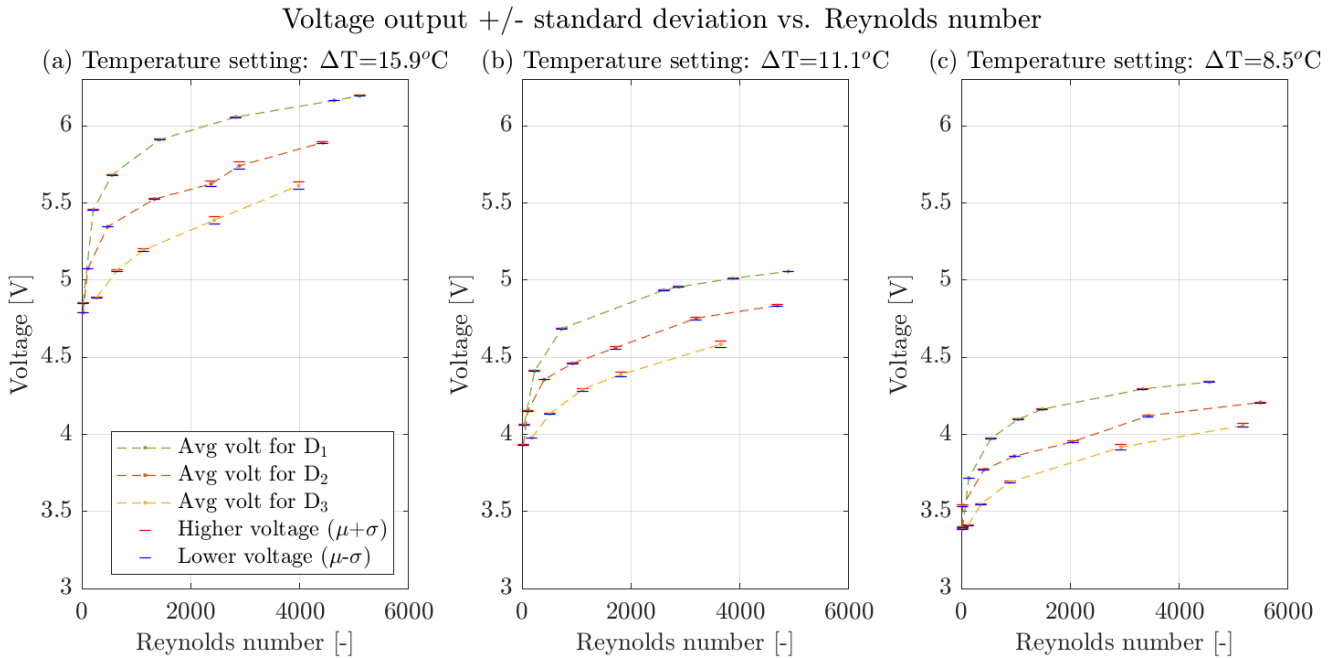


**Figure 3.4 | Output voltage with standard deviation for three sensor settings and three pipe diameters.**

The graphs show the results for three different temperature settings. On each graph, the voltages of the three different sensor diameters are visualized. It should be noted that the voltage for each sensor module is plotted against the Reynolds number. To achieve the same Reynolds number in two pipes of different diameters, the fluids must have different velocities, see equation 2.7. This explains the continual drop in output voltage for each increase in diameter. These results also imply that the investigated mass flow sensor does not, in reality, measure the mass flow in the sensor module but actually measures the local velocity of the fluid.

The standard deviation of the graphs is most visually apparent for the largest sensor, with diameter  $D_3$ . The largest

sensor as such, does not perform with the same stability as the smaller sensors. The larger standard deviation might be a result of the different placement of the heater and temperature sensor as described in subsection 2.1.2. The result could also indicate that the sensor is, simply, the most reliable in small geometries.

Independent of sensor module diameter or temperature setting, the standard deviation increases at Reynolds numbers between 2000 and 3000. As described in section 2.2.1, this is the range in which the fluid is expected to transition from laminar to turbulent flow.

The graphs show an apparent tendency in the stability of the sensors. From the graphs, it is, however, not evident, whether the relative deviation follows the average voltage. Therefore, the standard deviation is shown against the normalized voltage average, to give a clear indication of the relative spread of the measured voltage. The normalized voltage can be seen for sensor setting  $\Delta T = 8.5^\circ\text{C}$  for each sensor module diameter in figure 3.5. The rest of the graphs can be seen in appendix C in figure C.6 to C.9.

Normalised voltage,  $\tilde{V}$ , and standard deviation,  $\sigma$ , for  $\Delta T=8.5^\circ\text{C}$

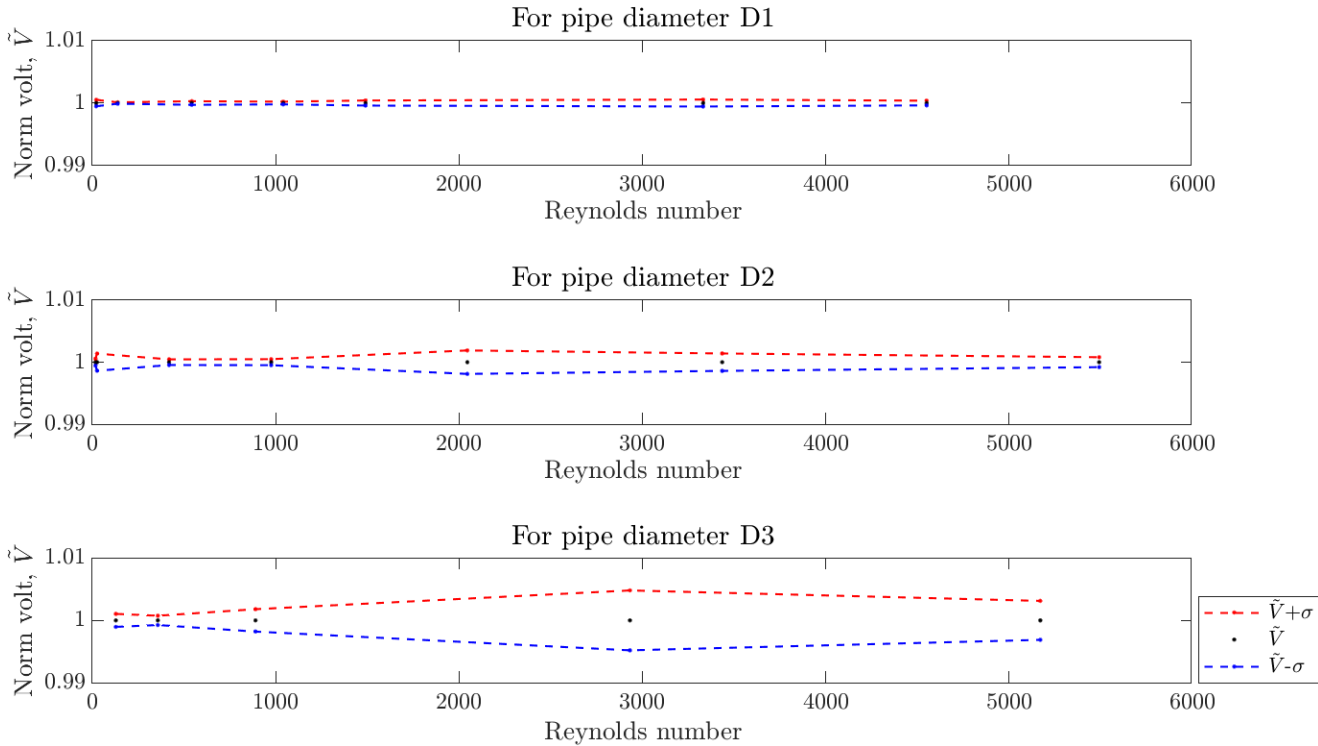


**Figure 3.5 | Standard deviation of normalized voltage for all pipe diameters.**

Figure 3.5 proves the expected behavior of the standard deviation. From this graph, the standard deviation visibly increases as the diameter of the sensor modules increases. Such behavior proves consistently independent of temperature setting, as can be seen from the graphs in appendix C. For diameter,  $D_1$ , the operation of the sensor proves quite stable throughout the changing Reynolds numbers. For the largest sensor module diameter,  $D_3$ , the standard deviations are significantly larger than for the smaller sensor modules, through all the investigated Reynolds numbers. Additionally, it becomes apparent that the standard deviation is higher in flows of Reynolds numbers in the transitional region at a value of about  $Re = 3000$ . It is evident, for  $D_2$ , that the output voltage becomes more fluctuating, at Reynolds numbers between 2000 and 3000, where the flow is transitioning.

To make clear what effect the flow region had on the standard deviation for all three diameters across all temperature differences, a percentage evaluation has been conducted. As evident in table 3.1, the visually observed tendencies are confirmed.

Diameter	Lam - Trans	Trans - Turb	Lam - Turb
$D_1$	128.5%	-30.9%	52.3%
$D_2$	765.4%	-52.6%	221.9%
$D_3$	258.4%	8.4%	269.5%

**Table 3.1 | Table of the percentage difference between flow regions averaged across temperature difference. Lam:** Laminar flow region. **Trans:** Transitional flow region. **Turb:** Turbulent flow region.

It should be noted, that the average percentage difference is based on only a few data points in each flow region.

During the experimental execution, the velocities were altered for each investigated temperature setting, resulting in some incidental larger leaps in Reynolds number. In some cases, this resulted in a lack of data points within the transitional region. From several graphs seen in appendix C, the transitional region proved to show a significant increase in standard deviation. An additional investigation was, thus, conducted to evaluate the standard deviations within the transitional region. Conducted with the sensor module of diameter D<sub>2</sub>, three temperature settings were investigated, from which the resulting graphs can be seen in figure 3.6.

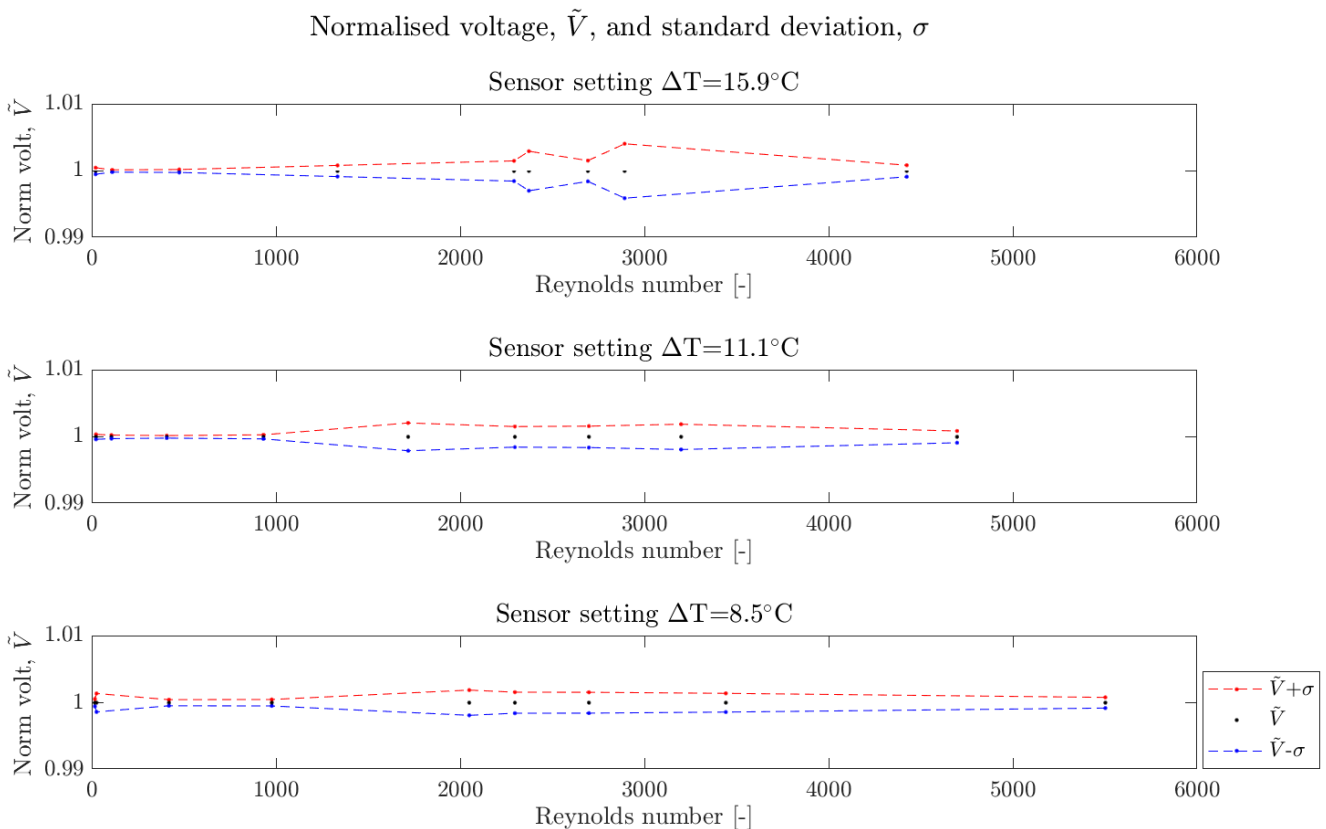


**Figure 3.6 | Standard deviation of normalized voltage for D<sub>2</sub>**

This figure brings more insight into the transitional region, as the standard deviation tends to increase in this region and, thus, produce less stable results.

With the additional two data points found in the transitional region for the sensor diameter D<sub>2</sub>, it was of interest to examine the accuracy of the sensor based on these. Considering the investigation of temperature setting  $\Delta T = 8.5^\circ\text{C}$  and  $\Delta T = 15.9^\circ\text{C}$ , fits were found for these settings, based on King's Law, which can be found in figure 3.3b. In table 3.2, the average output voltage from the sensor response can be seen along with the corresponding measured volume flow. Using the fits seen in 3.3b the expected volume flow has been calculated as well as the percentage error between the measured and expected value.

Temperature difference	$\Delta T = 8.5^\circ\text{C}$		$\Delta T = 15.9^\circ\text{C}$	
Avg. output voltage	3.98 V	4.01 V	5.71 V	5.74 V
Measured vol. flow rate	511.7 mL/min	601.2 mL/min	511.7 mL/min	601.2 mL/min
Expected vol. flow rate	417.4 mL/min	490.9 mL/min	580.7 mL/min	652.3 mL/min
Percentage error	18.42%	18.34%	13.5%	8.5%

**Table 3.2 | Accuracy of fits on additional data points.**

As evident from the errors between the experimentally derived volume flow and the expected values, the sensor is found to be inaccurate, within the flow region of the investigated points.

In both figure 3.5 and 3.6, an increase in standard deviation in the region of small Reynolds numbers can be observed. In figure 3.7 the standard deviations for each sensor setting and pipe diameter have been illustrated.

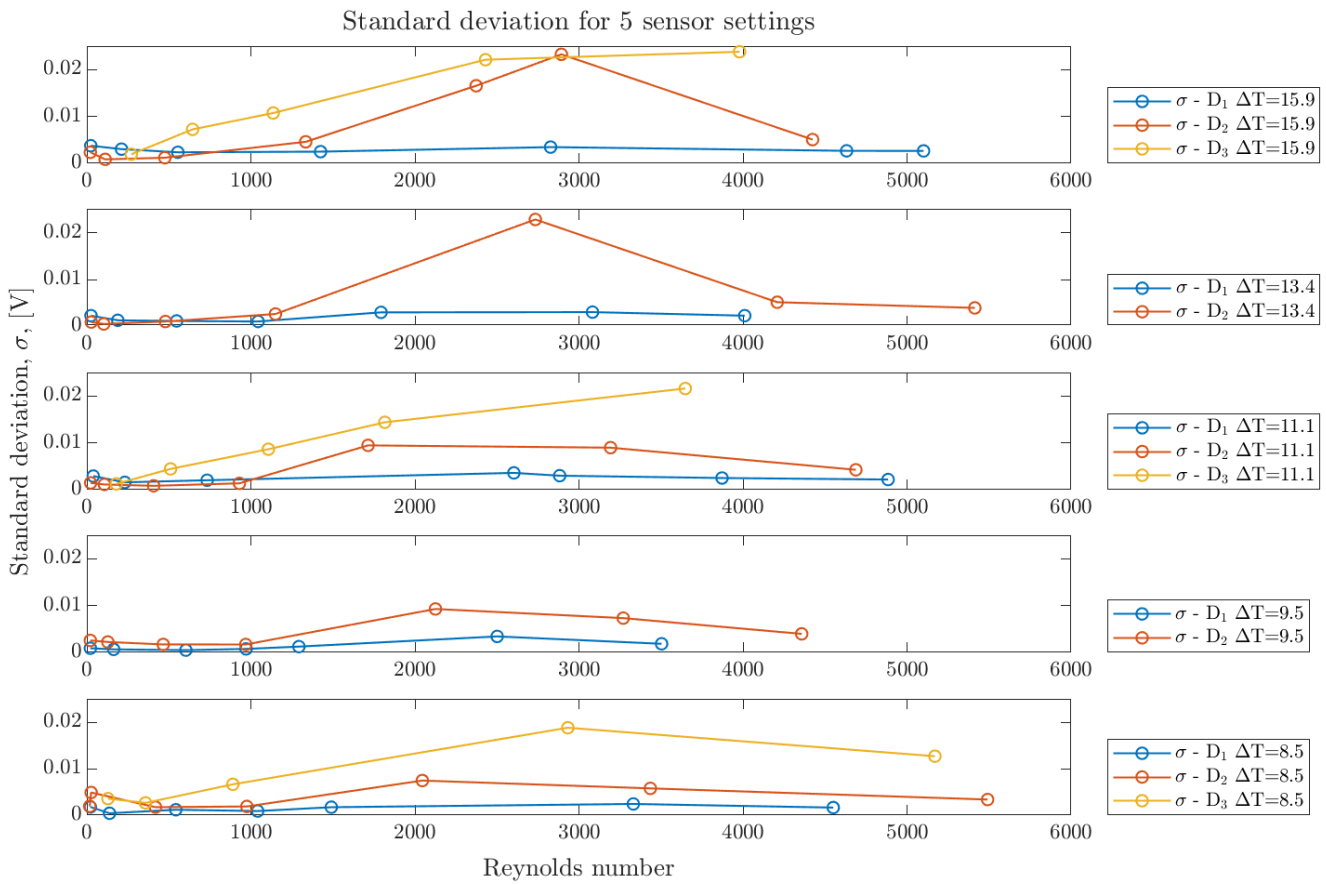
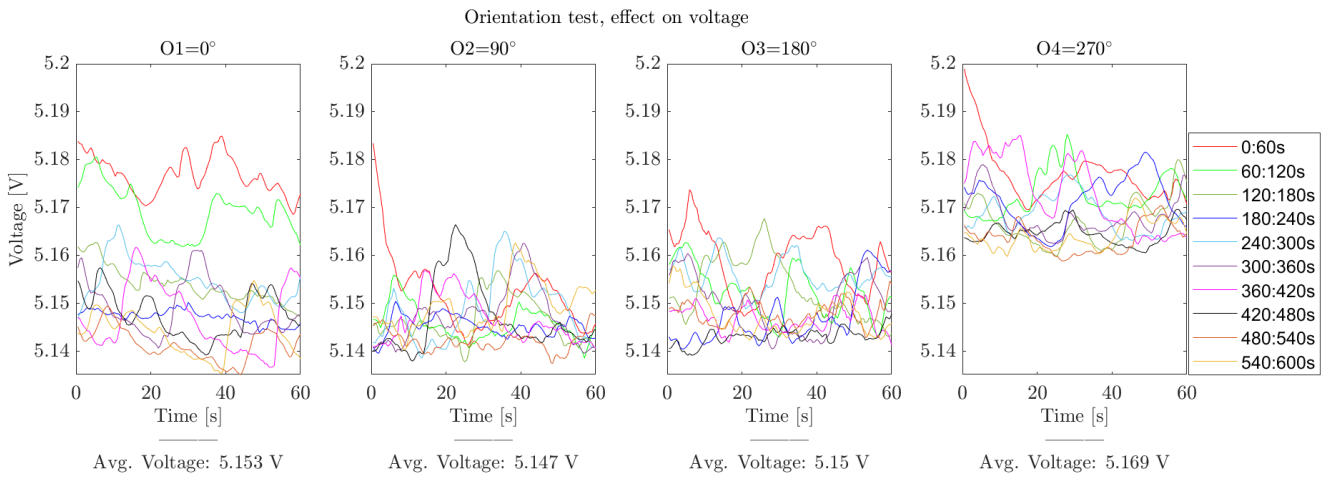


Figure 3.7 | Standard deviation for five different sensor settings on three sensor diameters.

It should be noted that the standard deviation in these graphs is not shown relative to the average output voltage. These graphs also show that the standard deviation is generally much larger for the largest sensors. The standard deviation of the voltage for  $D_3$  is a factor of ten larger than the standard deviation for  $D_1$ . These results indicate that the sensor concept might not be scalable to larger geometries.

## 3.2 | Effect of Inlet Boundary Conditions - Bends

After investigating the performance of the sensor under different flow velocities and temperature settings, it was of interest to examine how the sensor output responded to a change in inlet boundary conditions. The aim of this investigation was to determine whether the orientation of the sensor should be considered during installation. To explore this, bends were introduced in the pipe at a specified distance, denoted as  $L$ , from the sensor. The sensor output was then examined at different orientations of the sensor, as described in section 2.1.3. All experiments described in the section were conducted with a temperature setting of  $\Delta T = 15.9^\circ\text{C}$  and a volume flow of  $\dot{Q} = 214 \text{ mL/min}$ . The resulting time series data can be seen in figure 3.8.



**Figure 3.8 | Voltage time series of four different orientations, L = 22 mm.**

The graph in figure 3.8 does not immediately reveal any substantial impact of the sensor orientation on the output. The observed differences in the results were minimal, with a maximum difference of 0.022 V. To further analyze this finding, an experiment was conducted comparing the average voltage for each orientation in the pipe with a bend to the results obtained in a straight pipe. Figure 3.9 illustrates the comparison between the average voltage of the four orientations and the average voltages measured in a straight pipe.

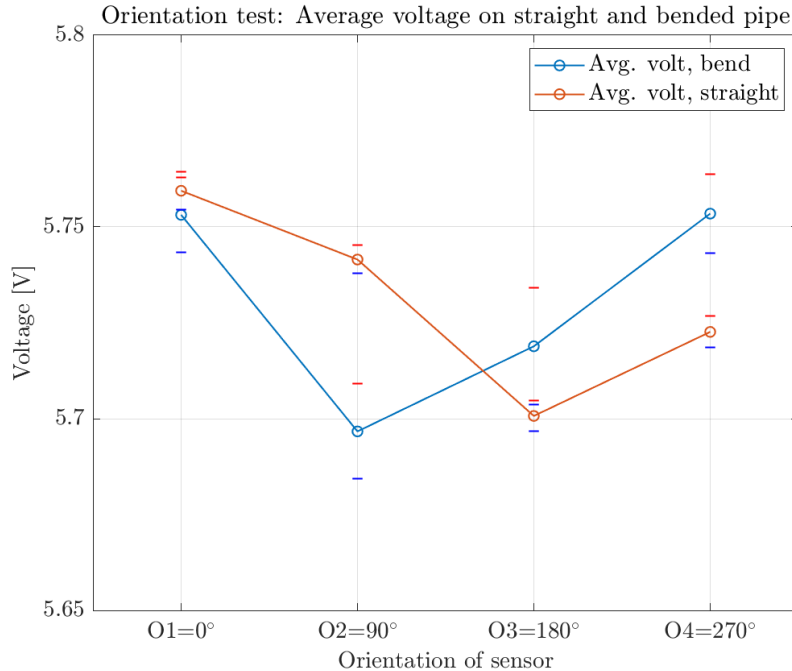


**Figure 3.9 | Average voltage for four different orientations for straight pipe and pipe with a bend, L = 200mm.**

The graph illustrates that average voltages found in the straight pipe are also affected by the sensor orientation. This indicates that the orientation of the sensor should be considered in straight pipes during installation. In addition, experiments were performed with three different lengths between the sensor and the bend to examine the effect this distance variation had on the average voltage. The corresponding graphs can be found in figure C.10 in appendix C. It is noteworthy that a significant change in length results in a drop in the average voltage. However, no discernible pattern is observed between the change in average voltage and the sensor orientation. Lastly in the investigation of the effect of sensor orientation, the stability of the sensor performance was evaluated. This was achieved by comparing the standard deviation found for each orientation as seen in figure 3.10.

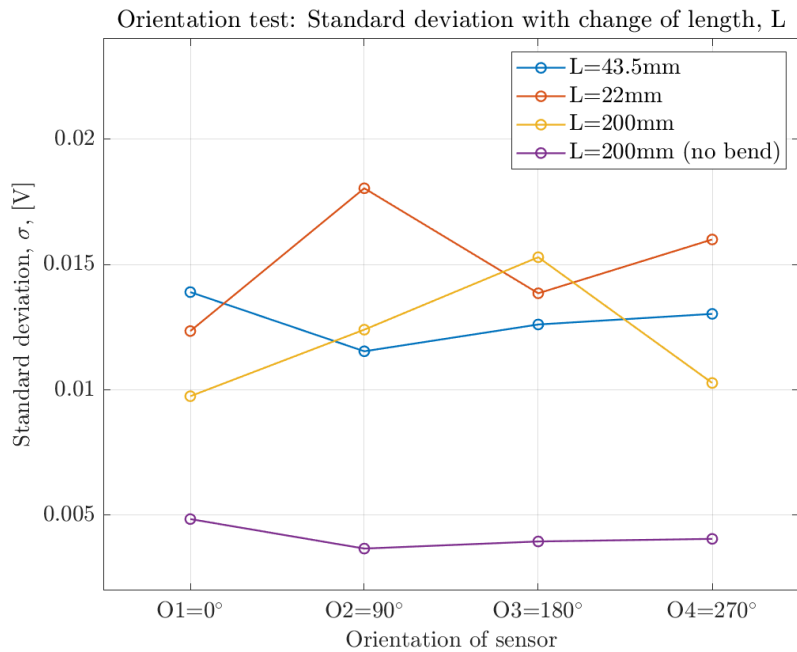


Figure 3.10 | Standard deviation for bend results for different lengths.

The standard deviation of the experiments performed on the pipe system with a bend indicates that the sensor performs most stably in systems with no bends. Further experiments were conducted in which the velocity and temperature settings of the sensor were varied. However, no discernible pattern was found in the difference in standard deviation between the different orientations of the sensor.

### 3.3 | External Forced Convection

Lastly, during the investigation of the sensor, it was of interest to examine its response to external forced convection. As the workings of the sensor module are based on an internally forced convection, it will be considered implicit in this section, and is, therefore, not referred to when discussing convection.

The first test was conducted by allowing the sensor to run with only natural convection for one minute before applying forced convection. After one minute, the external forced convection was removed and the sensor was allowed four minutes to reach equilibrium. Figure 3.11 shows the result of the forced convection test.

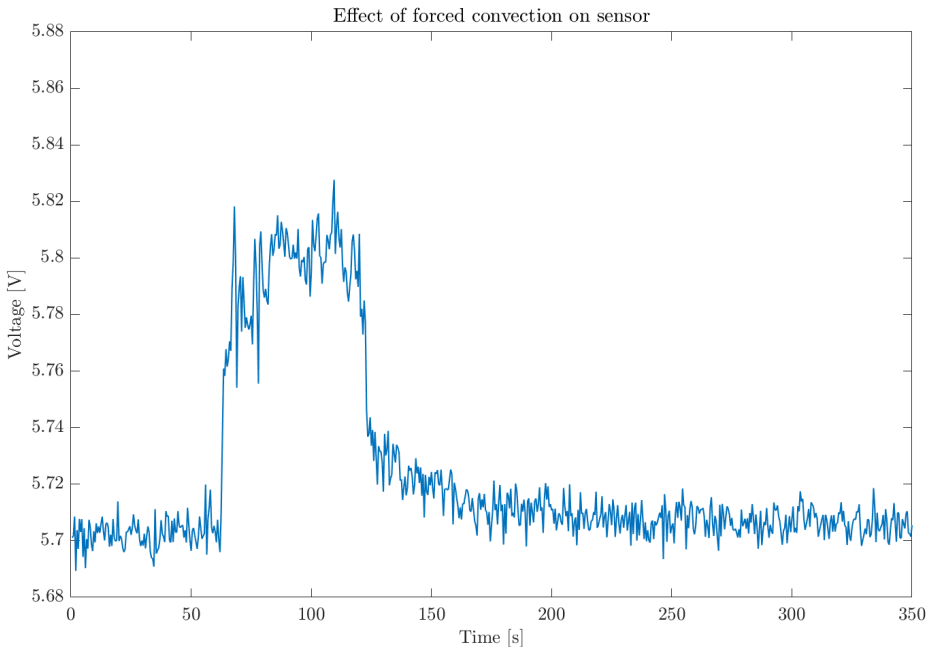
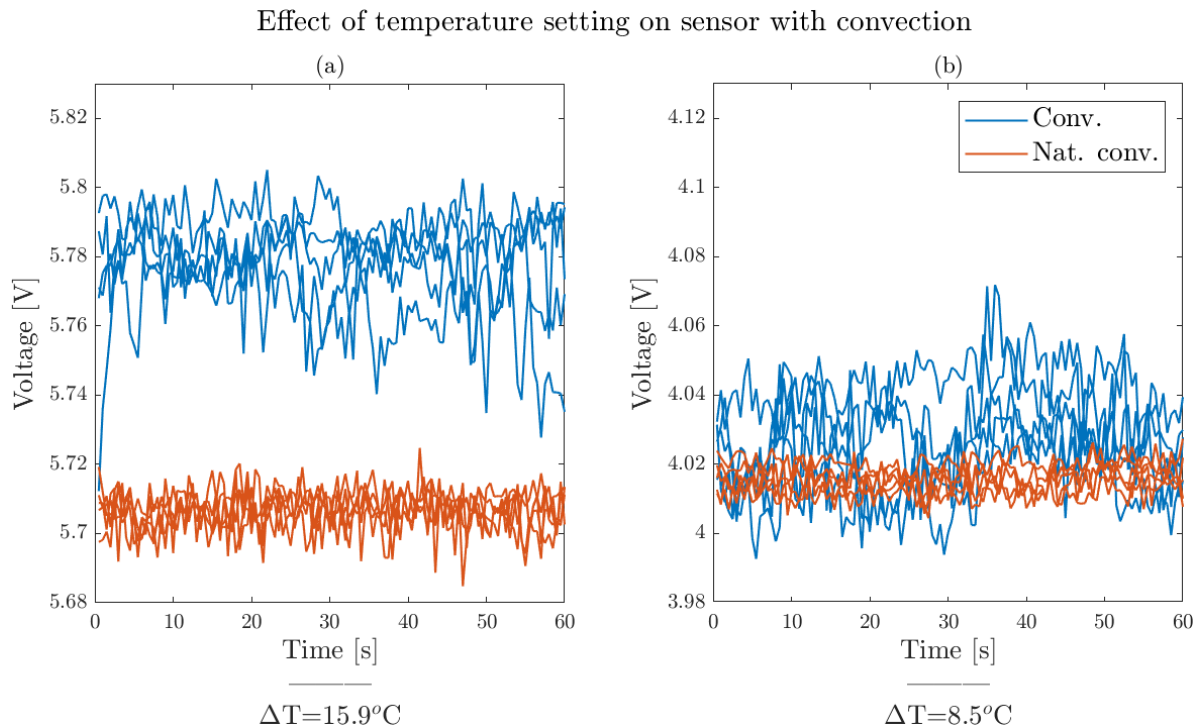


Figure 3.11 | Forced convection test in 1-1-4 interval.

During the test, a significant change in the output voltage was observed when the sensor was exposed to forced convection. Based on this result, it was decided to further investigate and quantify the impact thereof. The effect of forced convection was investigated on three different parameters: temperature setting, velocity, and insulation level of the sensor.

Two temperature settings were used to examine the difference of impact, forced convection had on the output voltage. In figure 3.12, the voltage time series of the two temperature settings can be seen, with and without forced convection.



**Figure 3.12 | Forced convection impact on two temperature settings.** The experiment was conducted with a Reynolds number of  $\text{Re} = 2350$ .

In the forced convection experiments, the sensor output fluctuated significantly more than in experiments where only natural convection was present. The average voltage observed under forced convection was likewise, higher than the average voltage recorded in the experiments without. The effect of different temperature settings can be seen in the amount the average voltage is shifted upwards under forced convection. In figure 3.12a, with a temperature setting of  $\Delta T = 15.9^\circ\text{C}$ , the two voltage time series are distinctly separated due to the significant increase in voltage, the forced convection has constituted. Conversely in figure 3.12b, the voltages between the two experiments have a high degree of overlap. The exact results of the experiments can be seen in table 3.3.

$\Delta T$	Avg. volt, conv	Avg. volt, no conv	% error
$15.9^\circ\text{C}$	5.81 V	5.72 V	1.6%
$8.5^\circ\text{C}$	4.03 V	4.02 V	0.2%

**Table 3.3 | Table showing temperature setting, avg. volt and percent-change for forced convection experiment**

From the average voltages the corresponding volume flow rates were calculated as can be seen in table 3.4.

$\Delta T$	Volume flow, conv	Volume flow, no conv	% error
$15.9^\circ\text{C}$	849.7 mL/min	603.7 mL/min	40.7%
$8.5^\circ\text{C}$	545.3 mL/min	517.6 mL/min	5.3%

**Table 3.4 | Table showing temperature setting, avg. volt and percent-change for forced convection experiment**

From the data, it can be seen that the sensor with a temperature setting of  $\Delta T = 15.9^\circ\text{C}$  results in a much larger error between the natural and forced convection experiments. This large difference in error suggests that

an ideal setting might be present when the sensor is implemented in tap water. In the experiments with forced convection, the same hairdryer setting was used, and as such the same convection was achieved throughout the experiments. The difference in change of average voltage will then be due to the relative difference between the wanted temperature difference of the sensor and the amount of heat being removed due to forced convection. The standard deviation has been visually represented in figure C.13 in appendix C.

In previous experiments, the sensor output has been investigated under different velocities. The average voltage has been determined in regard to flow rates along with the stability of the sensor in different flow ranges. It was therefore a parameter of interest to investigate under the influence of forced convection. Three different velocities were investigated; one in the laminar flow regime, one in the transitional, and one in the turbulent. The average voltages and standard deviations through the different velocities have been recorded for both the natural convection experiments and the forced convection experiments. The resultant graph can be seen in figure 3.13 in which average voltage has been plotted with a range calculated by use of standard deviation. The experiment has been conducted on a sensor with a temperature setting of  $\Delta T = 15.9^\circ\text{C}$ .

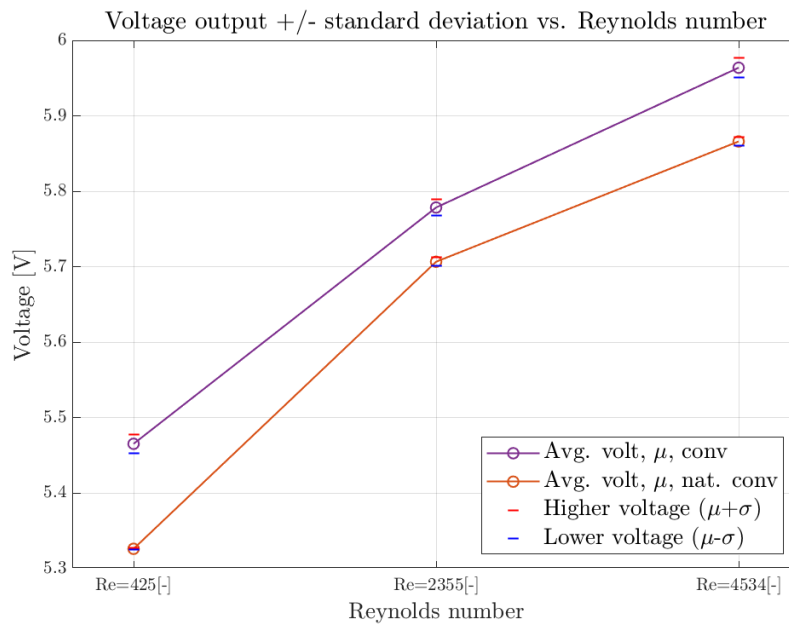


**Figure 3.13 | Voltage and standard deviation as a function of Reynolds for convection experiment.**

The graph shows a significant increase in average voltage between the forced and natural convection case, particularly for the laminar, low flow velocity. The standard deviation of the forced convection experiment is found to be significantly higher than for the natural convection experiment as can be seen in figure C.14 in appendix C.

The aim of investigating the influence of forced convection on the sensor output was to determine necessary considerations for sensor installation and to identify the applications in which the sensor would exhibit stable performance. It was therefore of interest to examine, how the impact of forced convection varied across different levels of insulation. Understanding this impact allows for the optimization of the sensor performance by adapting the installation procedure to the specific installation location. As such this investigation aimed to broaden the possibilities of sensor installation and methods. The experiment was conducted with the same temperature setting of  $\Delta T = 15.9^\circ\text{C}$  throughout, as well as the same velocity of 0.51 m/s.

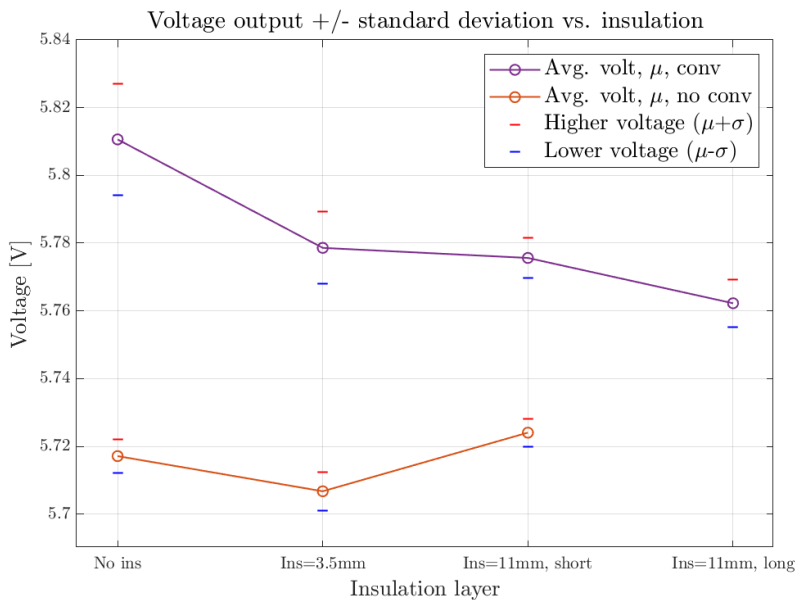


**Figure 3.14 | Voltage and standard deviation vs. insulation thickness.**

The results shown in figure 3.14 show that the most significant increase in average voltage, with and without convection, is seen in the uninsulated case, as one would expect. From the results with forced convection, a significant improvement for both average voltage and the standard deviation is achieved by covering the sensor with 3.5 mm insulation. After the first amount of insulation has been added, the benefits of further insulation become less pronounced. The largest amount of insulation results in a small further drop of the average voltage resulting in a difference of under 0.02 V from when the smallest insulation layer was added. This despite the amount of insulation has been more than tripled. The sensor performance also becomes significantly more stable with an increase in insulation as can be seen in figure 3.15.

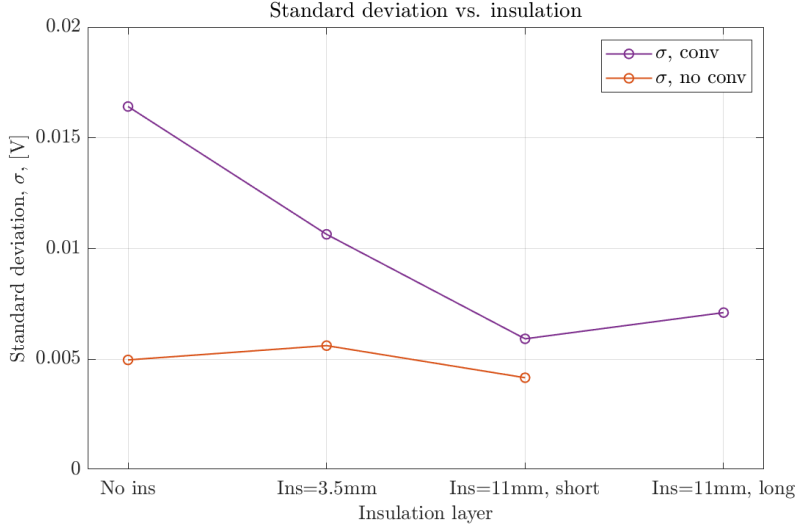


**Figure 3.15 | Standard deviation vs. insulation thickness.**

The standard deviation of the output illustrates how the output becomes more stable as the insulation of the sensor is increased. The insulation with a thickness of 11 mm (short) performs most stable with a standard deviation difference under 0.002 from the corresponding no-convection experiment. From this result, it might be deduced that the sensor with insulation of 11 mm (short) could simply be calibrated to account for the difference in average voltage and would not need an increase of insulation as it behaves as stable as the no-convection case.

For the last part of the investigation of the impact of forced convection, five interval experiments were conducted in a similar set-up as the first mentioned experiment, with the exception of the allotted time to reach equilibrium being reduced from four to two minutes. The primary objective of these experiments was to determine the duration it would take for an uninsulated sensor to reach equilibrium after being exposed to forced convection. By conducting these experiments, the aim was to gain insight into the sensor's response and understand the time required for it to

stabilize under varying conditions of convection. The decision to limit the time was based on a visual estimation of the settling time observed in figure 3.11.

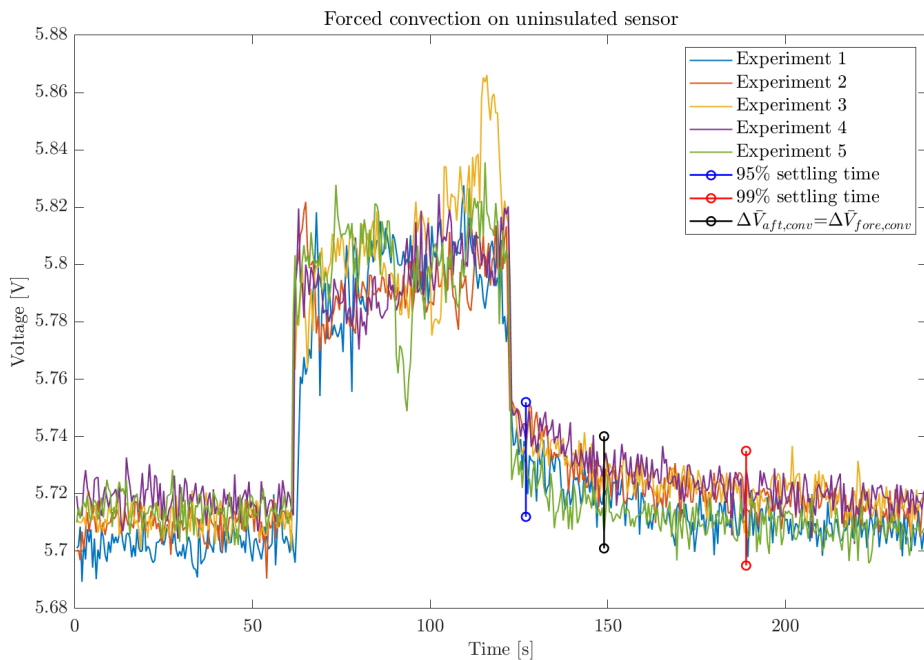


**Figure 3.16 | Forced convection tests in 1-1-2 interval. 95% settling time (blue)=6 s after convection, 99% settling time (red)=68 s, average change (black)=29 s. The temperature setting was  $\Delta T=15.9^{\circ}\text{C}$ .**

The graph includes three lines indicating the 95% settling time, the 99% settling time, and the average change in average voltage. Settling time was calculated by comparing the average voltage before the introduction of convection with the average voltage of four consecutive data points after convection was removed. The black line represents the average change in the average voltage before convection was introduced. Dependent on the demand of precision of the sensor, the results show that it takes only about 6 seconds after the convection is removed for the sensor to settle if using a criterion of 95%. If a higher level of precision is required, with a criterion of 99%, the settling time is 68 seconds. However, if the aim is to minimize significant changes in comparison to the undisturbed system, it takes approximately 29 seconds for the system to meet this requirement.

A conversion from the voltage output to the corresponding volume flow has been made to determine the reading error the forced convection results in.

	Before conv.	With conv.	% error
Voltage	5.71 V	5.80 V	1.5%
Vol. flow	582.9 mL/min	809.6 mL/min	38.9%

**Table 3.5 | Table showing avg. volt with corresponding vol. flow and percent-error for forced convection experiment.**

From the found volume flows the significance of forced convection on the sensor response becomes obvious resulting in a 38.9% error in the flow reading.

## 3.4 | Simulations

### Straight Pipe Temperature Contours

To gain further insight into the workings of the sensor module, it was of interest to see how the temperature propagated through the flowing fluid. This insight was achieved by simulating a constant heat flux applied to the heater element on the sensor module. The heat flux corresponding to the desired temperature difference was found through iterations. The results thereof are depicted in figure 3.17 with a mesh size 2 as seen in figure 2.14b.

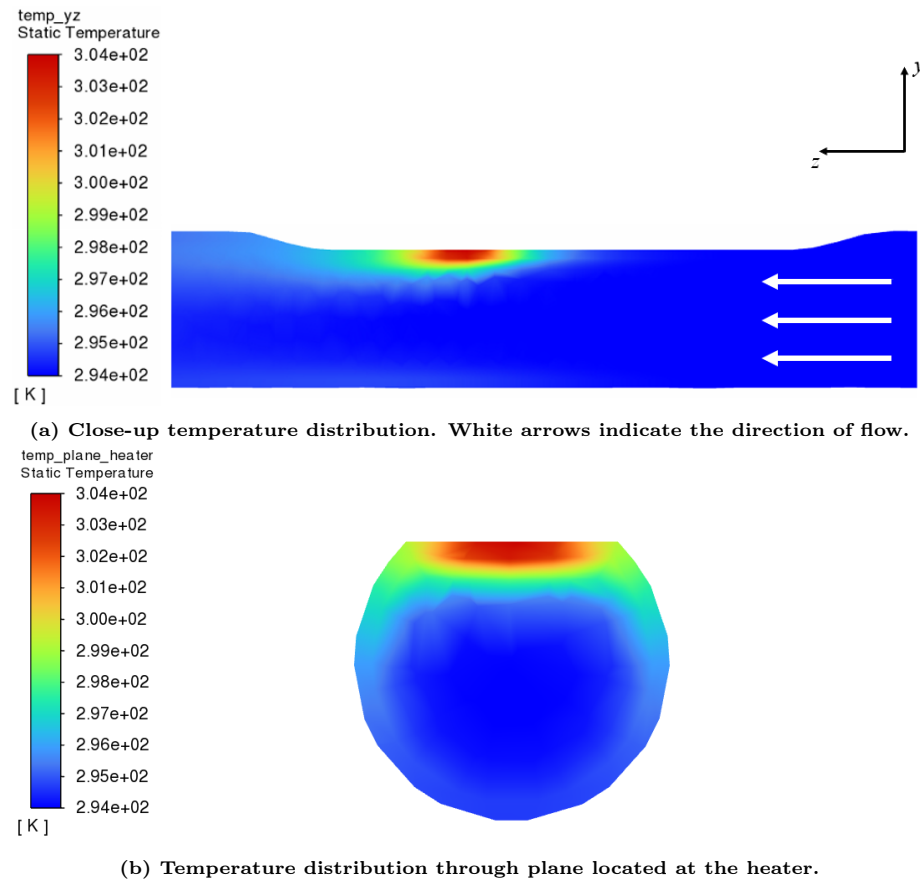


**Figure 3.17 |** Temperature distributions for  $\Delta T = 15.9^\circ\text{C}$ ,  $U = 0.0033 \text{ m/s}$ .

Upon observing figure 3.17b it becomes evident that the heat distribution is most efficient in the outer rim of the profile. This is due to the close proximity of the steel pipe, which possesses higher thermal conductivity, allowing a more rapid propagation of heat. In figure 3.17a the heated water is seen to be carried along with the direction of the flow, from right to left. The contour plot for flows of mesh size 1, size 3, and size 4 can be seen in figure D.1 in appendix D.

### Bend Pipe Velocity Contours

Introducing a bend in the sensor setup, the velocity of the fluid is expected to travel faster on the outside of the bend and slower on the inside, which would be visible on the velocity contour plot. If this change in velocity causes a disturbance of the fluid that propagates all the way to the sensor, this could affect the readings. By simulating where the bend is oriented in different directions as described in section 2.1.3 this can be used to predict whether orientation has an effect on the sensor response. Such a velocity contour plot depicting orientation 1 of the sensor is visual in figure 3.18 with a length between the bend and sensor of 22 mm.

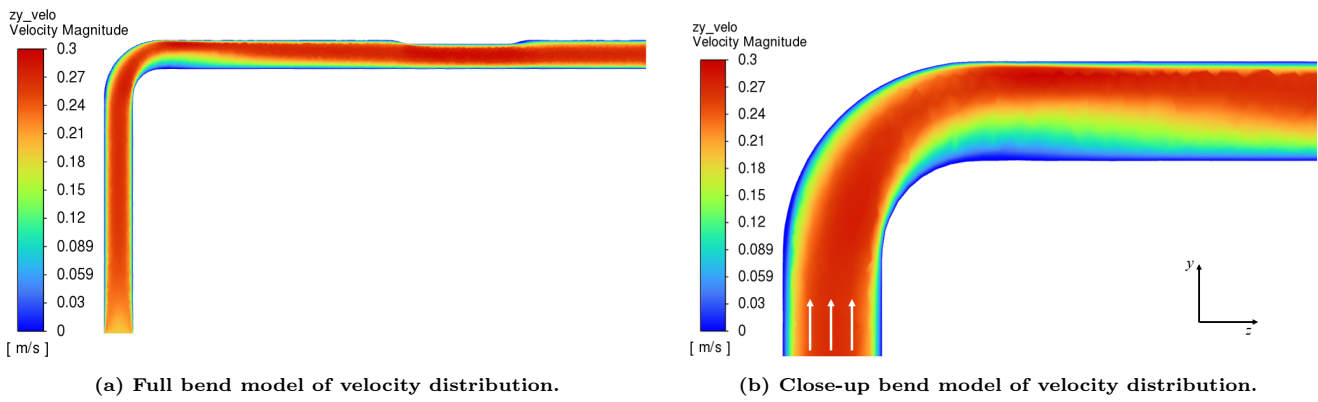


**Figure 3.18** | Bend-pipe velocity contours for  $\Delta T = 15.9^\circ\text{C}$  with inlet-velocity  $U = 0.1873 \text{ m/s}$ , the maximum investigated velocity for bends. White arrows indicate flow direction.

Due to the low fluid velocity the flow quickly recovers after the bend. This result indicates that a change in sensor response should not be visible due to the effect of inlet conditions. Therefore, the velocity and the desired temperature difference, at the heater and sensor, should remain unaffected by the bend.

It should be noted, however, that the bend simulations are simplified compared to the experimental setup since in reality there are small contractions where the pipe is inserted into the bend, and where the sensor is inserted into the pipe.

### 3.4.1 | Comparison of Simulated and Experimental Results

The simulation has been done with the assumption of laminar flow below  $Re = 2300$  and with SST  $k-\omega$  turbulence modeling for flows above, the difference of which is indicated by a black dashed line in figure 3.19. The voltage from the experiments has been converted into power by use of equation B.8 in appendix B knowing that the resistance of the heater is given by the manufacturer to be  $50 \Omega$  [9]. The experimental and simulated results are plotted for comparison for  $\Delta T = 8.5^\circ\text{C}$  and  $\Delta T = 15.9^\circ\text{C}$ :

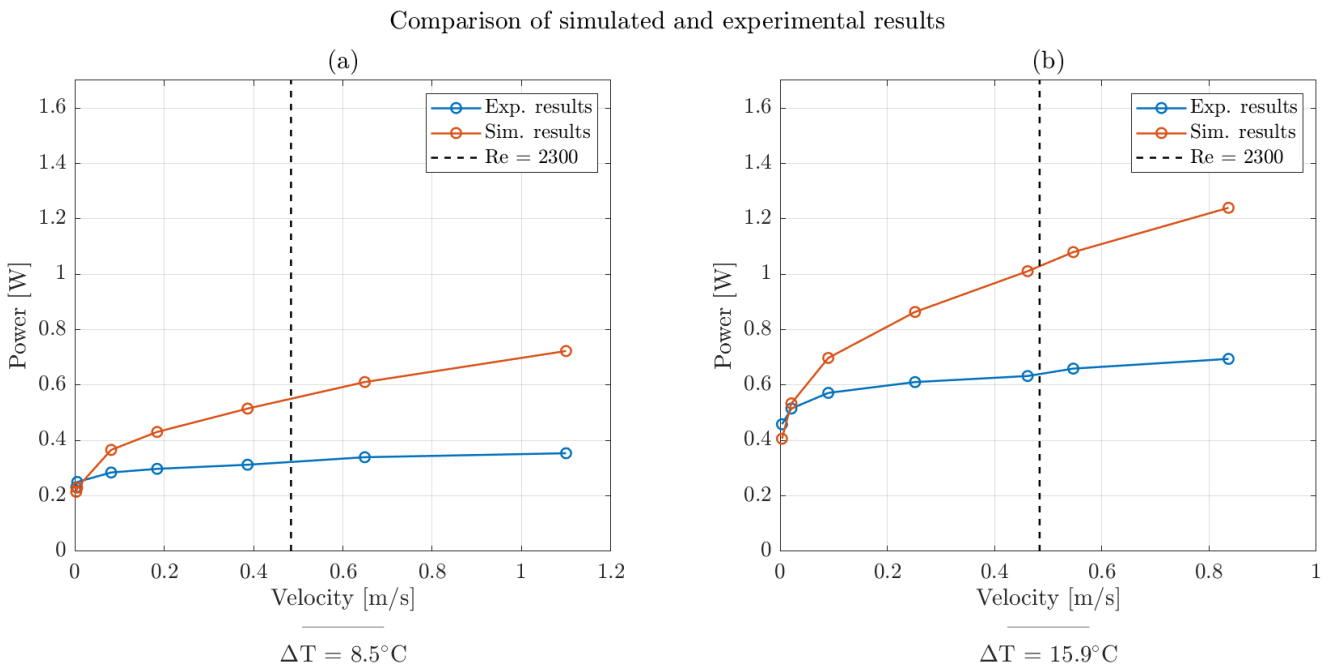


**Figure 3.19** | Comparison of straight pipe simulation with experiments for  $\Delta T = 8.5^\circ\text{C}$  and  $\Delta T = 15.9^\circ\text{C}$ .

Qualitatively, the simulated results show the same general tendency as the experimental results. Additionally, for the same setting of  $\Delta T$ , the simulated results are especially accurate at low velocities  $< 0.05 \text{ m/s}$  and become decreasingly less accurate as the velocity increases. As such the simulated results in this case represent a conservative estimation of the experimental results.

Bend simulation results for two different velocities at four different orientations are shown in figure 3.20.

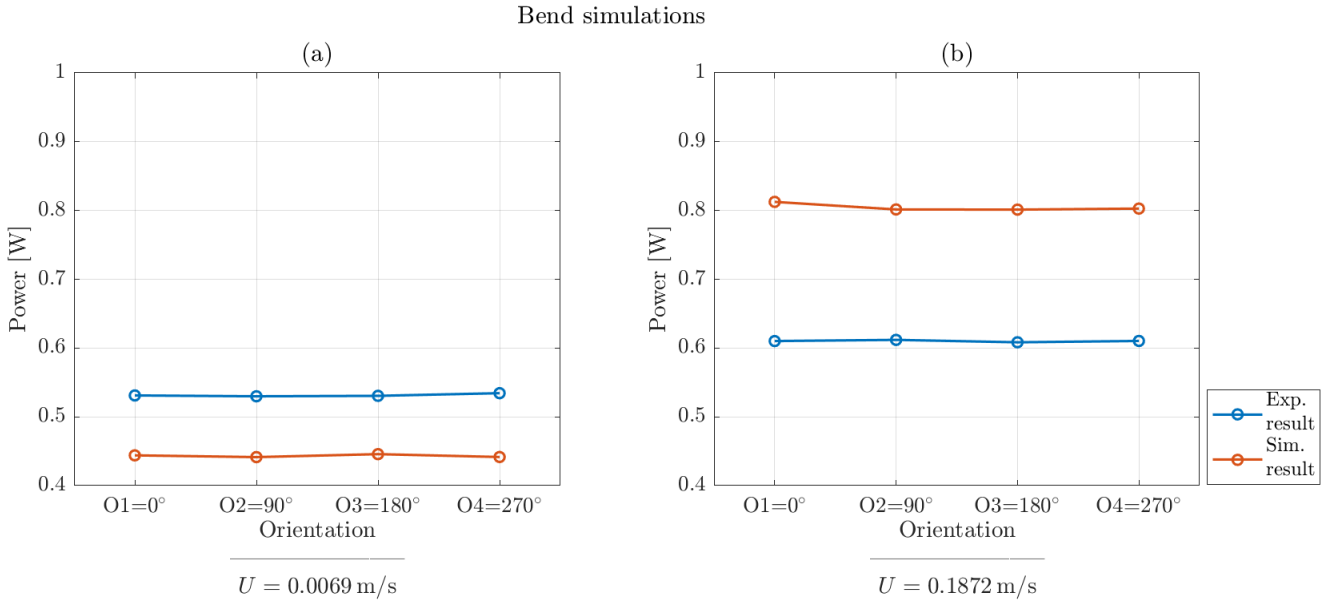


**Figure 3.20 | Comparison of bend simulation and experimental results for  $\Delta T = 15.9^\circ\text{C}$ .**

The power that is applied in the simulations and the average power from the experiments are similar in the sense that they barely change for different orientations. For low velocities, it can be seen that the simulated results undershoot the experimental results whereas for high velocities the simulation overshoots the experimental results. This is a tendency that the straight pipe simulations shown in figure 3.19 also suggest. Furthermore, the velocity contour found in the simulation of inlet conditions confirms the experimental results, in which no discernible pattern was found between orientation and sensor response. Had the contour indicated the expected behavior in the velocity profile at the sensor position, the response would be expected to show a higher value on the outside of the bend and conversely, a lower value on the inside, as depicted in figure 2.8.

## 4 | Conclusion

With the ability to measure low flows in small geometries, the iST thermal mass flow sensor offers a great solution to the optimization of systems and minimizing machine downtime. This report investigated the operating principle and performance under different operating conditions and installation requirements of the sensor module from iST.

Initializing the experimental data collection, operational considerations were deducted by a test of the time for the sensor output to settle. A dependence between sensor module diameter and time for the voltage to level was deduced to be between 5-10 minutes. As such, in further workings with the iST mass flow sensor module, a delay should be considered when initializing operation, regardless of the sensor module diameter size.

Based on information from the manufacturer, iST, the output signal response of the sensor across varying mass flows, was expected to be described by a characteristic curve based on King's law. This behavior was confirmed based on experimental and numerical evaluations. The experiments under varying flow conditions proved the sensor response to correlate with King's law with a coefficient of determination of value  $R^2 = 0.97$ . The curve characteristics found from the experimental results were further confirmed by tendencies found through CFD analysis, in which results were found through iteration. Upon experimental and numerical confirmation of the correlation to the expected curve characteristics, King's law was utilized to derive an expression that described the analytical equation for a specified temperature setting for two different sensor diameters. This equation was found with a coefficient of determination of minimum  $R^2 = 0.89$ . After the correlation between mass flow rate and corresponding voltage was found the sensor response was examined in terms of stability through varying states of flow.

The stability of the voltage output was examined by varying the mass flow in order to gain insight into the ideal operating range of the sensor module. Determining the stability of the voltage output, by utilizing standard deviation, it was observed that the voltage was less stable in the turbulent region compared to the laminar region. Furthermore, when considering flow in the transitional region of  $2000 < \text{Re} < 3000$ , the output was found particularly unstable in comparison to other flow regions. This information suggests an ideal region of operation in the low flow regime. However, as evident from the investigation, appeared a small increase in instability when operating in a very low flow region, often below a Reynolds number of  $\text{Re} < 100$ .

Besides the ideal working range, operational conditions were additionally investigated to offer suggestions as to the installation of the sensor module for ideal operation. To change the flow conditions, it was decided to introduce  $90^\circ$  bends upstream and downstream of the sensor. It was theorized that the velocity would decrease on the inside, and increase on the outside of the bend. If the sensor was placed too close to the bend, this local increase in velocity might skew the readings of the sensor. To test this the sensor module was rotated with respect to the bend, and compared to the same orientations of a case with no bends. It was observed that when the sensor was placed on the outside of the bend, no discernible difference was found between the case with and without bends, indicating the bend itself had no effect on the average voltage. Additionally, it was found that the orientation of the sensor had some effect on the average voltage, however, no identifiable pattern could be concluded from this. Moreover, considering the standard deviation of the case with bends compared to the case without bends, it was found that by introducing bends the stability of the sensor decreased.

The iST thermal flow meter is an out-of-liquid sensor with measuring elements exposed to the surroundings. It was therefore of interest to examine the sensor response when exposed to forced convection, as opposed to natural convection. The effect of insulation was subsequently investigated for a potential increase in stability and effect on output response.

As expected the application of forced convection led to an increase in voltage, as well as a vastly more unstable output compared to the case of natural convection, with a standard deviation three times greater. This increase resulted in a maximum reading error of 38.9% proving the sensor highly sensitive to external forced convection. Additionally, it was found that for higher values of  $\Delta T$ , the difference in voltage between the forced and natural convection cases was significantly larger than for smaller values of  $\Delta T$ . This suggests an ideal temperature setting

of the sensor when used in tap water.

When introducing insulation, it was observed that with increasing levels of insulation the average voltage in the case of forced convection decreased. With an 11 mm thick, short coverage insulation layer applied, the case of forced convection and natural convection became equally stable.

In conclusion, based on the investigation of this report, the iST thermal mass flow sensor operates optimally in laminar low flow ranges with the most stable outputs from experiments with the smaller sensor modules. In terms of installation of the sensor, in cases demanding high precision, bends should be avoided as these offer instability to the output. The instability was still affected when the sensor was installed at a length of 200 mm from the bend. The introduction of flow conditioners might improve the stability - this has, however, not been investigated within this report. Furthermore, in terms of installation, forced convection was found to have a large effect on the sensor module. Covering the sensor module with insulation of any type, proved to be ideal for more stable outputs when exposed to external forced convection. Although extensive, alterations to the investigation could be made to further strengthen the conclusion on the ideal operating range and installation requirements. In the experimental investigation, some of the testing equipment offered insecurities to the results. Among these were the electronically working units, such as the logger, the power supply, and the weighing scale, all with measurement uncertainties, which accounts for some inaccuracy in the results. Furthermore, the used pipes were made of a flexible material making them difficult to keep completely straight. In further investigations, other pipe material could be used to investigate the operation of the sensor when fluid motion is confined to a straight traveling path. Additionally, the experimental results were influenced by a change in environment as the experimental execution spanned across two seasons with weather changes affecting the ambient temperature. The experimental investigation, if conducted further, could, in addition, consider keeping the mass flows steady across the variation in temperature difference setting to ensure a more relevant comparison of the altering parameters. Furthermore, expanding the data collection and ensuring equal collection in all flow regions, would give more insight into the ideal operating range of the sensor module. Lastly, a more thorough CFD analysis could look into the effects of applying a non-adiabatic boundary condition, as well as the effects of the contractions caused by the sensor being inserted into the pipes. Additionally, the consideration of transient effects could offer more in-depth knowledge and possibly quantitative ground for comparison to the experimental results.

## 5 | Bibliography

- [1] ANSYS INC., *Introduction to Ansys Fluent: Lecture 6 Turbulence Modelling*. [https://imechanica.org/files/fluent\\_13.0\\_lecture06-turbulence.pdf](https://imechanica.org/files/fluent_13.0_lecture06-turbulence.pdf). [Online; accessed 24-05-2023].
- [2] BANG & OLUFSEN, *Bang & Olufsen Instruction - Power Supply SN16A*. [https://xdevs.com/doc/Bang\\_Olsen/SN16A%28A%29%20-%20Power%20Supply/SN16A%20%28en%29.pdf](https://xdevs.com/doc/Bang_Olsen/SN16A%28A%29%20-%20Power%20Supply/SN16A%20%28en%29.pdf). [Online; accessed 01-06-2023].
- [3] R. E. BERNHARDSGRÜTTER, C. J. HEPP, J. WÖLLENSTEIN, AND K. SCHMITT, *Fluid-compensated thermal flow sensor: A combination of the 3ω-method and constant temperature anemometry directions*, Sensors and Actuators A: Physical, 350 (2023).
- [4] Y. A. CENGEL AND A. J. GHAJAR, *Heat and Mass Transfer - Fundamental & Applications*, McGraw Hill, 2014.
- [5] J. CHEN, K. ZHANG, L. WANG, AND M. YANG, *Design of a High Precision Ultrasonic Gas Flowmeter*, Sensors, 20 (2020).
- [6] W. FREI, *Meshing Your Geometry: When to Use the Various Element Types*. <https://www.comsol.com/blogs/meshing-your-geometry-various-element-types/>. [Online; accessed 02-05-2023].
- [7] GLOBAL ELECTRONIC SERVICES, INC., *Advantages and Disadvantages of Ultrasonic Flowmeter*. <https://gesrepair.com/ultrasonic-flow-meter-advantages-disadvantages/>. [Online; accessed 30-05-2023].
- [8] iST AG, *Application Note - OOL Module - Thermal mass flow*. Data sheet. [Received: January 2023].
- [9] ———, *Out of Liquid Demo Module - Thermal Mass Flow Demo Module - Optimal for various “Out of Liquid” flow applications*. Data sheet. [Received: January 2023].
- [10] ———, *Quick Start Guide - Flow Demo Board - FS5/FS7, OOL*. Data sheet. [Received: January 2023].
- [11] ———, *Product launch webinar: OOL mass flow meter for liquid flow measurement*. Webinar at <https://www.ist-ag.com/en/flow-sensors>, 2022. [Online; accessed 23-05-2023].
- [12] L. LYNNWORTH AND Y. LIU, *Ultrasonic flowmeters: Half-century progress report, 1955–2005*, Ultrasonics, 44 (2006), pp. e1371–e1378. Proceedings of Ultrasonics International (UI'05) and World Congress on Ultrasonics (WCU).
- [13] W. L. MARTINEZ AND M. CHO, *Statistics in MATLAB a Primer*, CRC Press, 2014.
- [14] METTLER INSTRUMENTE AG, *Mettler PC16 Scale Manual*. <https://ltt.arizona.edu/sites/ltt.lab.arizona.edu/files/Mettler%20PC%2016%20scale%20manual.pdf>, 2016. [Online; accessed 21-04-2023].
- [15] M. PERIC AND S. FERGUSON, *The Advantage of Polyhedral*. [https://web.archive.org/web/20131206232340/http://www.plmmarketplace.com/upload/Tmp/The\\_Advantage\\_of\\_polyhedral.pdf](https://web.archive.org/web/20131206232340/http://www.plmmarketplace.com/upload/Tmp/The_Advantage_of_polyhedral.pdf), 2022. [Online; accessed 03-03-2023].
- [16] P. J. PRITCHARD, *Fox and McDonalds INTRODUCTION TO FLUID MECHANICS*, John Wiley & Sons, INC., 2011.
- [17] SIMSCALE, *Mesh Quality*. <https://www.simscale.com/docs/simulation-setup/meshing/mesh-quality/>. [Online; accessed 31-05-2023].
- [18] B. SJODIN, *What's The Difference Between FEM, FDM and FVM?* <https://www.machinedesign.com/3d-printing-cad/fea-and-simulation/article/21832072/whats-the-difference-between-fem-fdm-and-fvm>. [Online; accessed 02-05-2023].
- [19] T. WANG AND R. BAKER, *Coriolis flowmeters: a review of developments over the past 20 years, and an assessment of the state of the art and likely future directions*, Flow Measurement and Instrumentation, 40 (2014), pp. 99–123.
- [20] C. YOUNG, *Can Turbulent Flow Be Steady*. <https://engineerexcel.com/can-turbulent-flow-be-steady/>, 2022. [Online; accessed 03-03-2023].

## A | Experimental Pictures



**Figure A.1** | Picture of largest sensor with diameter  $D_3$  in foreground and second largest sensor with diameter  $D_1$  in background connected to pipes.

# B | Additional Theory

## B.1 | Wheatstone Bridge

The Wheatstone bridge can be viewed as two resistor branches in parallel as seen in figure B.1. The principle of a voltage divider can be applied to the Wheatstone bridge, in which the voltage of the source will be divided among the resistors in series in direct proportion to the resistance values. Because of the voltage divider principle, the voltage difference between point C and D should be zero in the simple case when  $R_1 = R_3$  and  $R_2 = R_4$ . A difference of zero between the two points constitutes a balanced Wheatstone Bridge. If however one of the resistors were a larger value e.g.  $R_2 < R_4$ , the voltage difference between points C and D would no longer be zero and the bridge is no longer balanced.

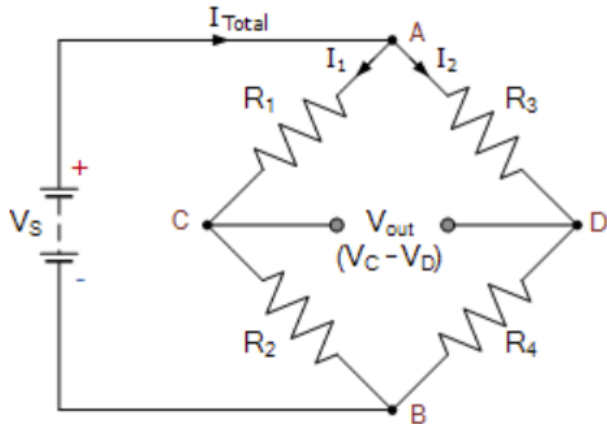


Figure B.1 | Wheatstone Bridge

If instead of known values, an unknown resistance were introduced along with a variable resistance e.g. in  $R_4$  and  $R_3$ . The difference in voltage between point C and D could now be measured while adjusting the variable resistance. Once a balanced bridge is achieved the unknown value of  $R_4$  could be determined, which is the theory behind the Wheatstone bridge.

## B.2 | Simplification of Equation for Wall-Adjacent Cell Size

A simplification of the equation for wall-adjacent cell size can be derived given equation 2.19, the equation for wall shear stress  $\tau_w$ , and the equation for skin-friction for duct flow  $C_f$

$$\tau_w = \frac{1}{2} C_f \rho U_\infty^2, \quad (\text{B.1})$$

$$C_f = 0.078 Re^{-0.25}. \quad (\text{B.2})$$

Inserting equations 2.19 and B.1 in equation 2.20.

$$\Delta y = \frac{y^+ \mu}{\sqrt{\frac{1}{2} C_f \rho U_\infty^2 \sqrt{\rho}}} = \frac{y^+ \mu \sqrt{2}}{U_\infty \sqrt{C_f \rho}}. \quad (\text{B.3})$$

Inserting equation B.2 and simplifying.

$$\Delta y = \frac{y^+ \mu \sqrt{2}}{U_\infty \sqrt{0.078 Re^{-0.25}} \rho} = \frac{y^+ \mu \sqrt{2}}{\rho \frac{\sqrt{0.078}}{\sqrt{Re^{0.25}}} U_\infty} = \frac{y^+ \mu \sqrt{2} \sqrt{Re^{0.25}}}{\sqrt{0.078} U_\infty \rho}, \quad (\text{B.4})$$

$$\Delta y \approx 5.06 \frac{y^+ \mu Re^{1/8}}{U_\infty \rho} = 5.06 \frac{y^+ \mu Re Re^{-7/8}}{U_\infty \rho}. \quad (\text{B.5})$$

This can be rewritten using equation 2.7.

$$\Delta y \approx 5.06 D_h Re_{d_h}^{-7/8} y^+. \quad (\text{B.6})$$

Thus the equation for wall-adjacent cell size is simplified.

## B.3 | Ohm's Law

Ohm's law is the relation between voltage, current, and resistance as shown in equation B.7

$$V = RI. \quad (\text{B.7})$$

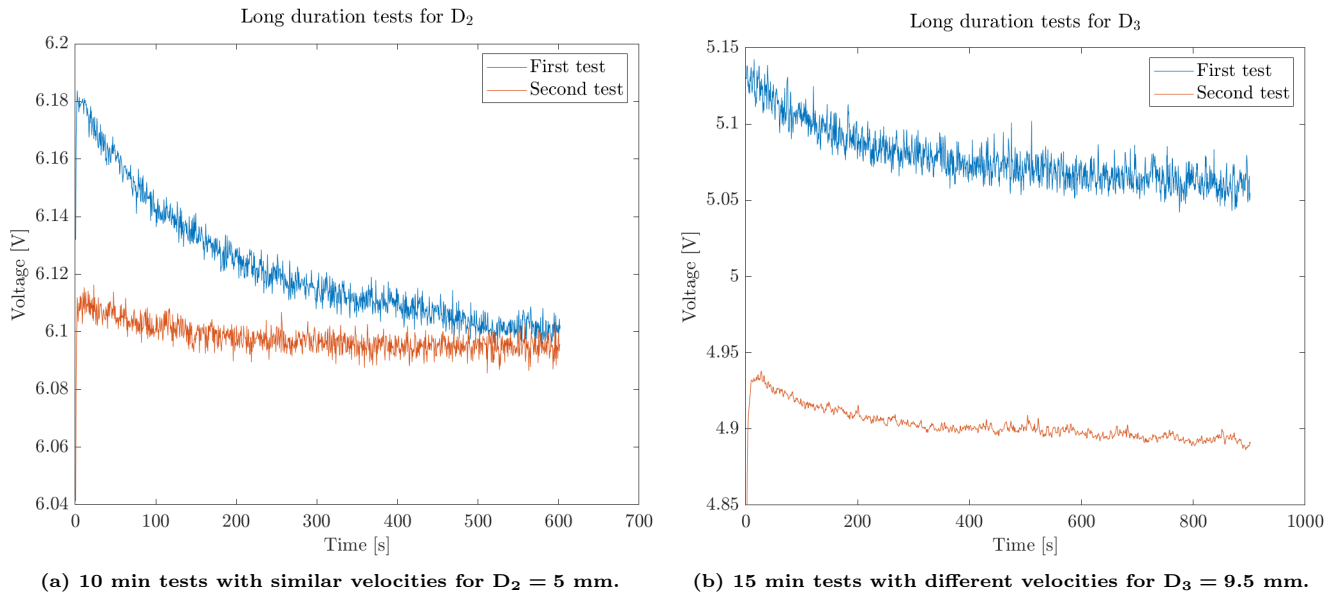
Combining with the equation for electrical power as shown in equation B.8 results in an equation that can be used to calculate the electrical power given a voltage and a resistance

$$P = VI = \frac{V^2}{R}, \quad (\text{B.8})$$

where the resistance of the heater is given by the manufacturer to be  $50 \Omega$ .

# C | Supplementary Plots - Experiments

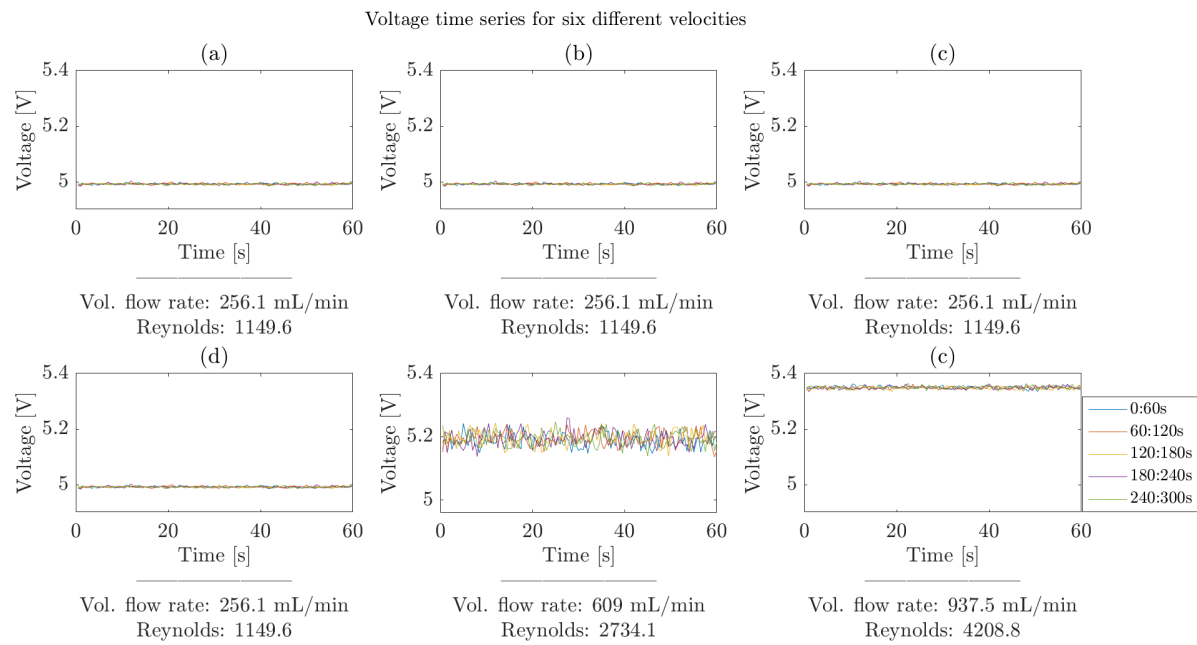
In the following appendices, additional plots have been included.



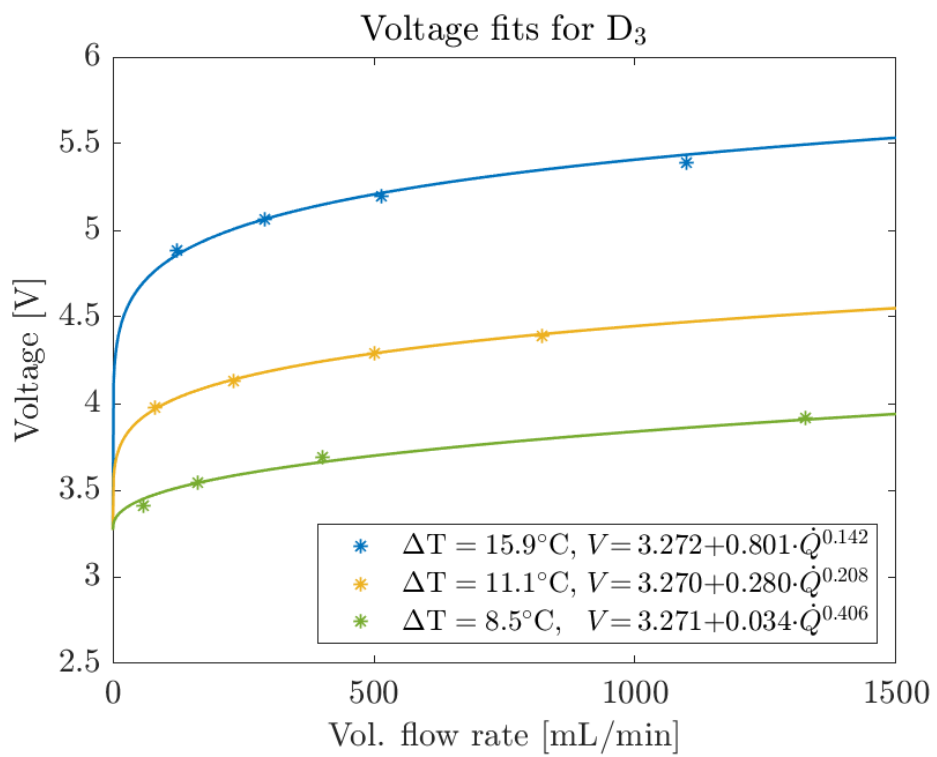
(a) 10 min tests with similar velocities for  $D_2 = 5$  mm.

(b) 15 min tests with different velocities for  $D_3 = 9.5$  mm.

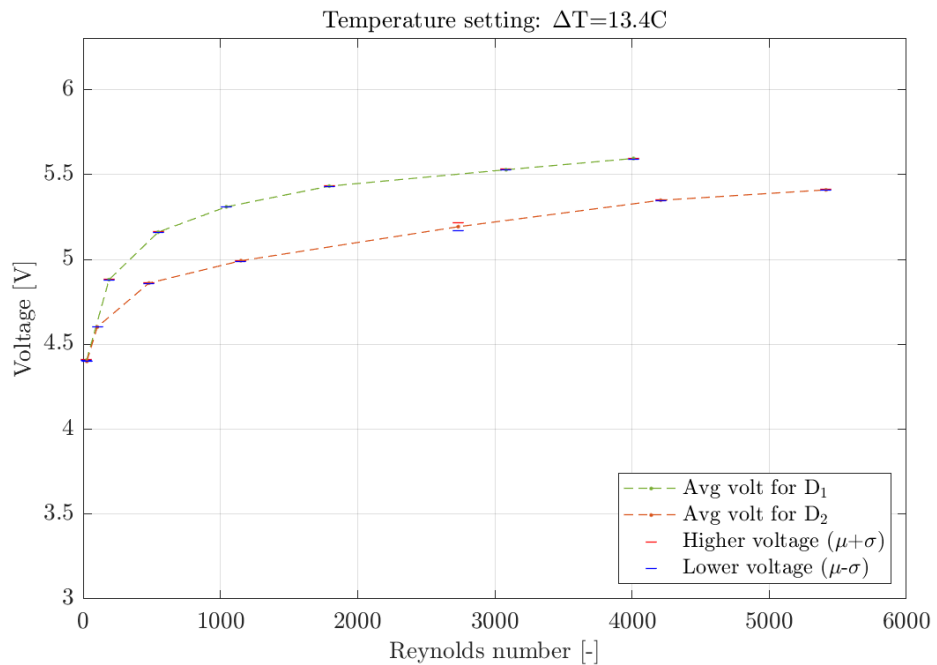
**Figure C.1 | Long duration tests for pipe diameters  $D_2$  and  $D_3$ .**



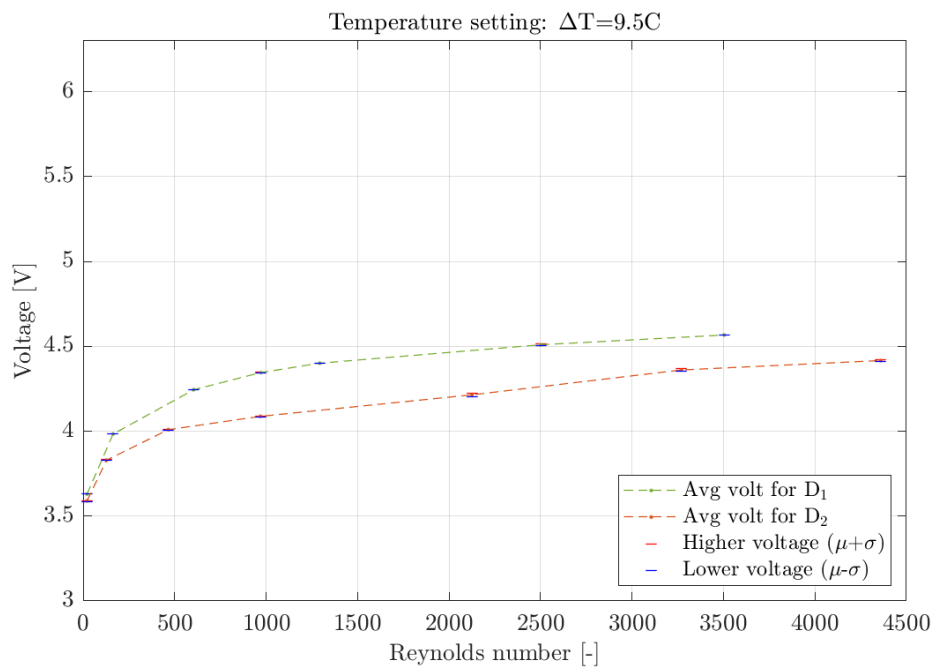
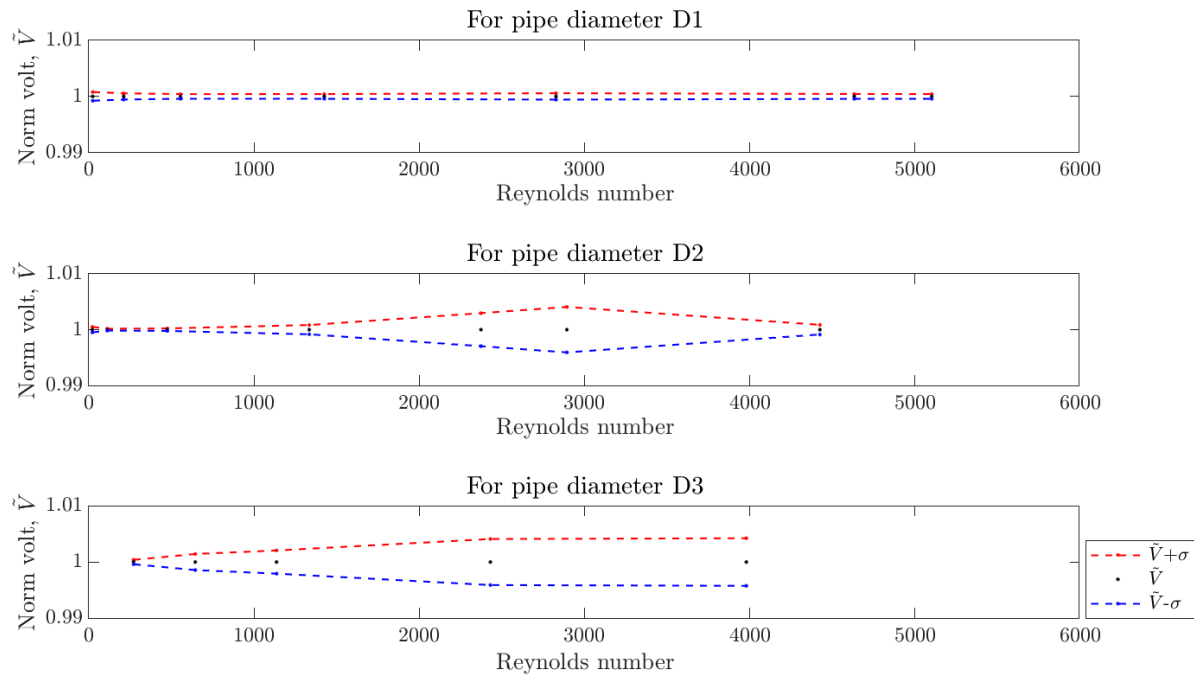
**Figure C.2 | Six voltage time series of different velocities.**

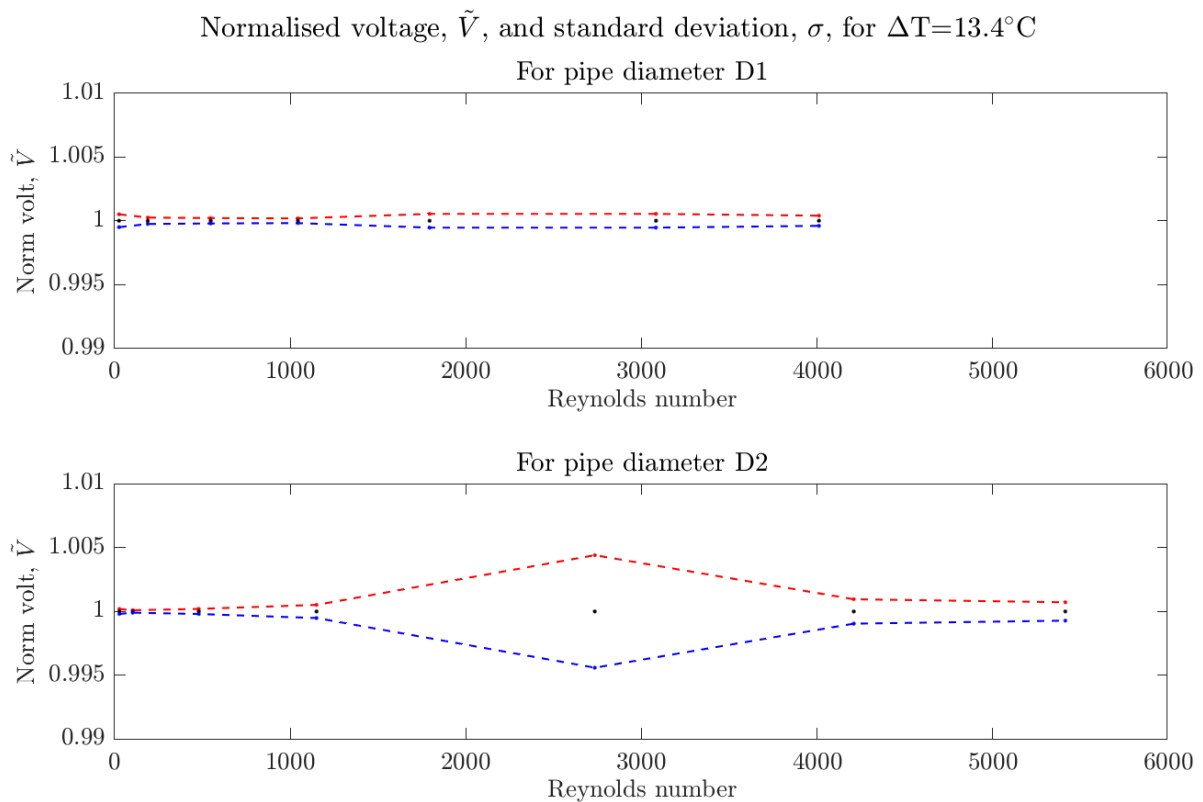
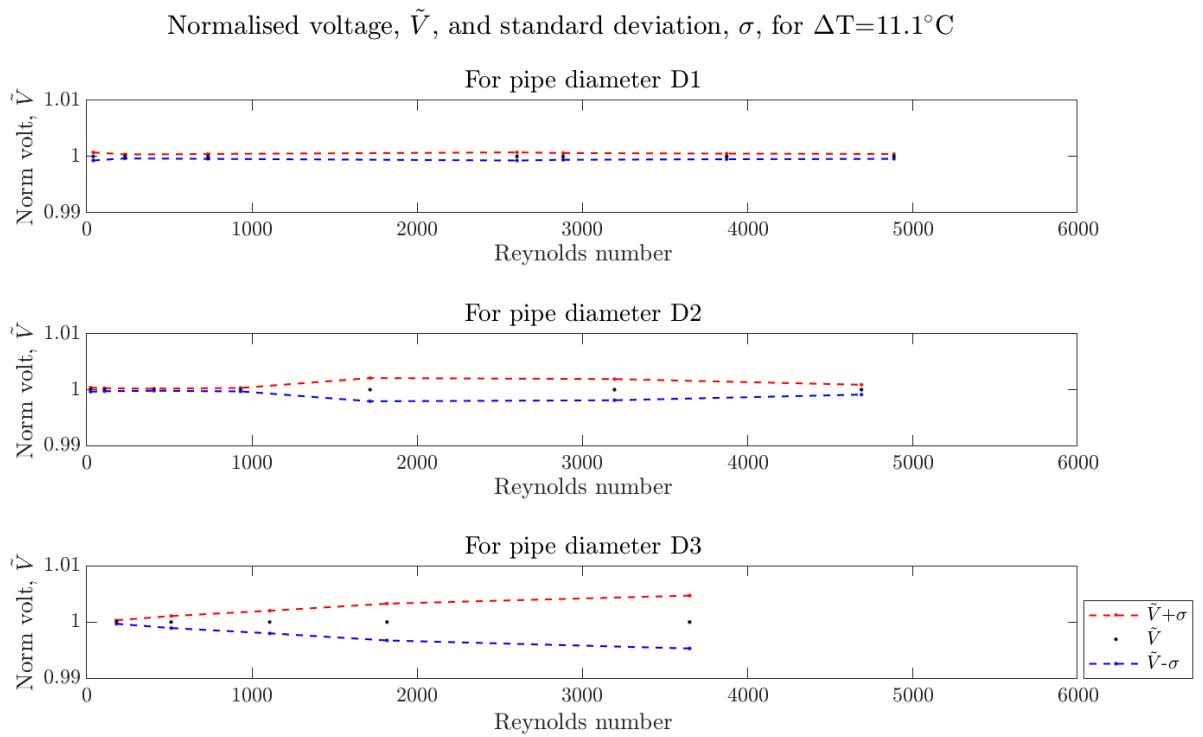


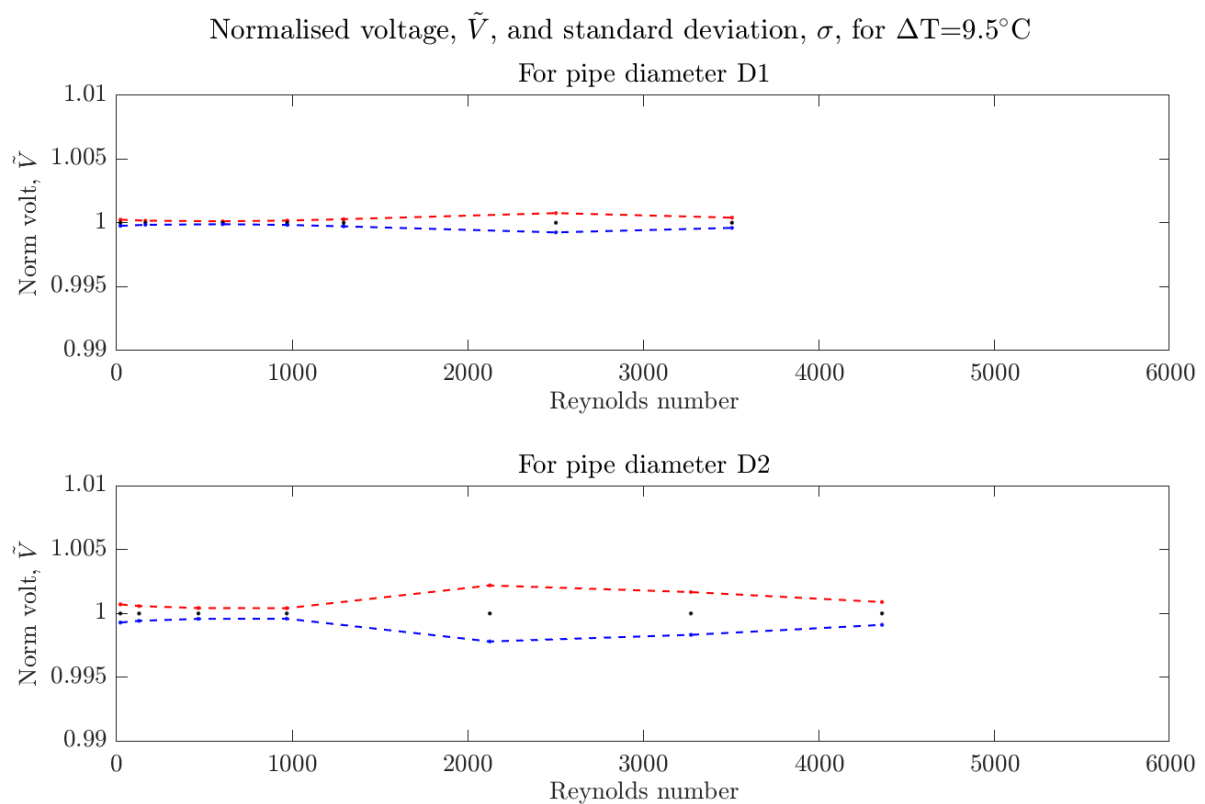
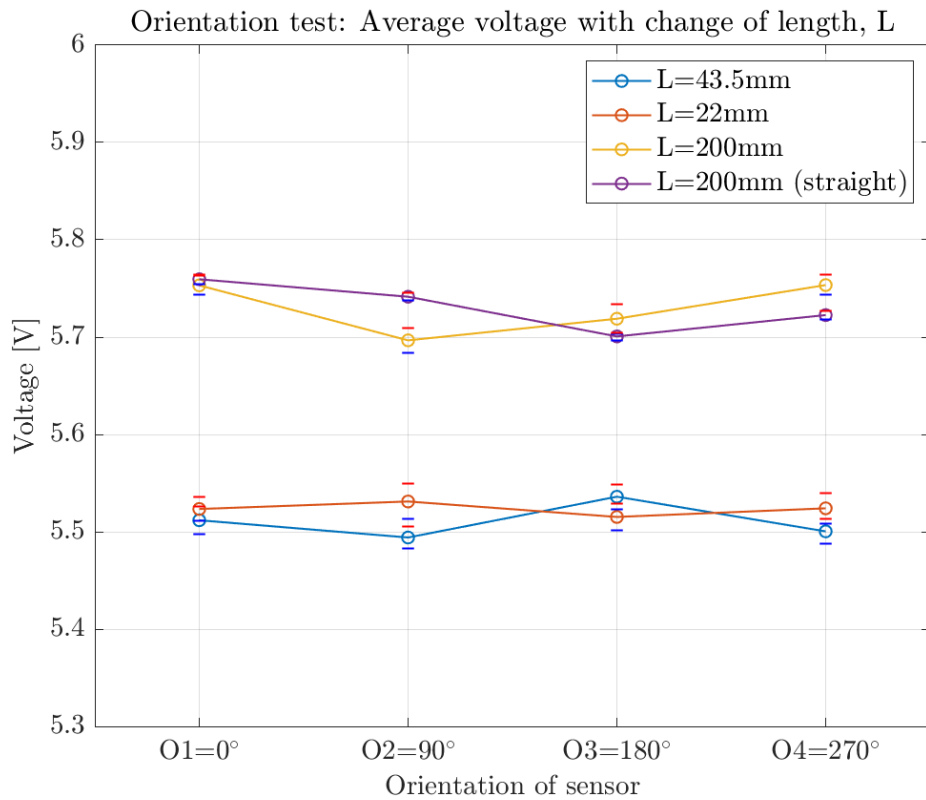
**Figure C.3 |** Voltage fits for D<sub>3</sub>. The minimum  $R^2$  is 0.99.



**Figure C.4 |** Average vol +/- standard deviation for three sensor diameters.

**Figure C.5 | Average vol +/- standard deviation for three sensor diameters.**Normalised voltage,  $\tilde{V}$ , and standard deviation,  $\sigma$ , for  $\Delta T = 15.9^\circ C$ **Figure C.6 | Normalised voltage and standard deviation for three sensor diameters.**

**Figure C.7 | Normalised voltage and standard deviation for two sensor diameters.****Figure C.8 | Normalised voltage and standard deviation for three sensor diameters.**

**Figure C.9 | Normalised voltage and standard deviation for two sensor diameters.****Figure C.10 | Average voltage for orientation test of differing lengths, L, with control test on a straight pipe.**

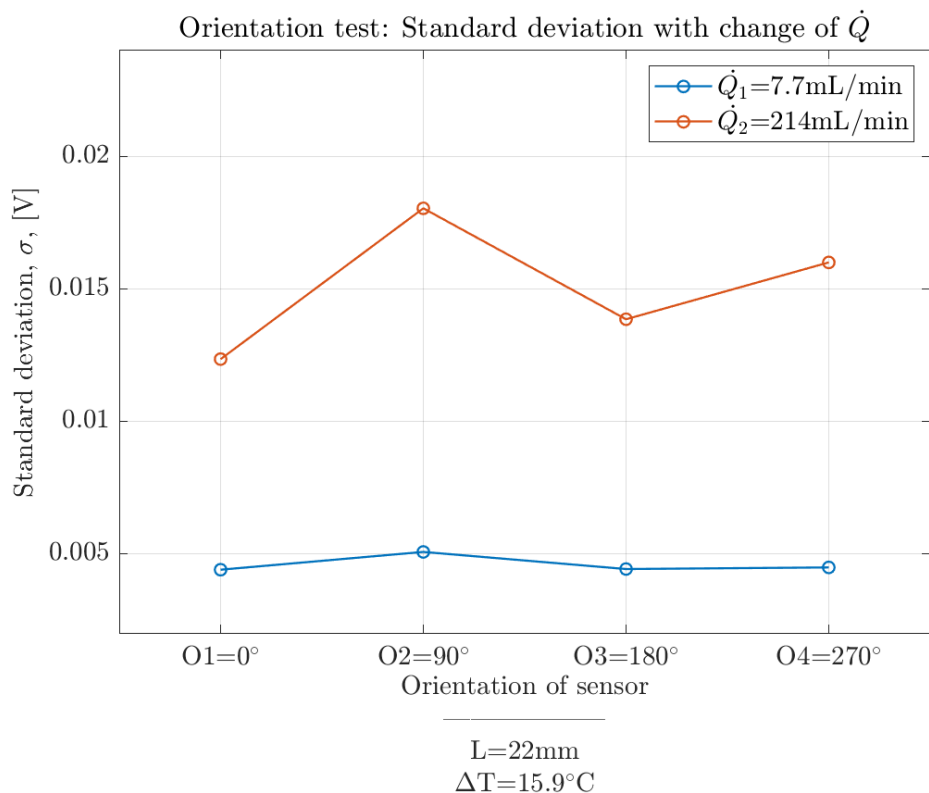


Figure C.11 | Standard deviation vs. vol. flow rate for orientation test.

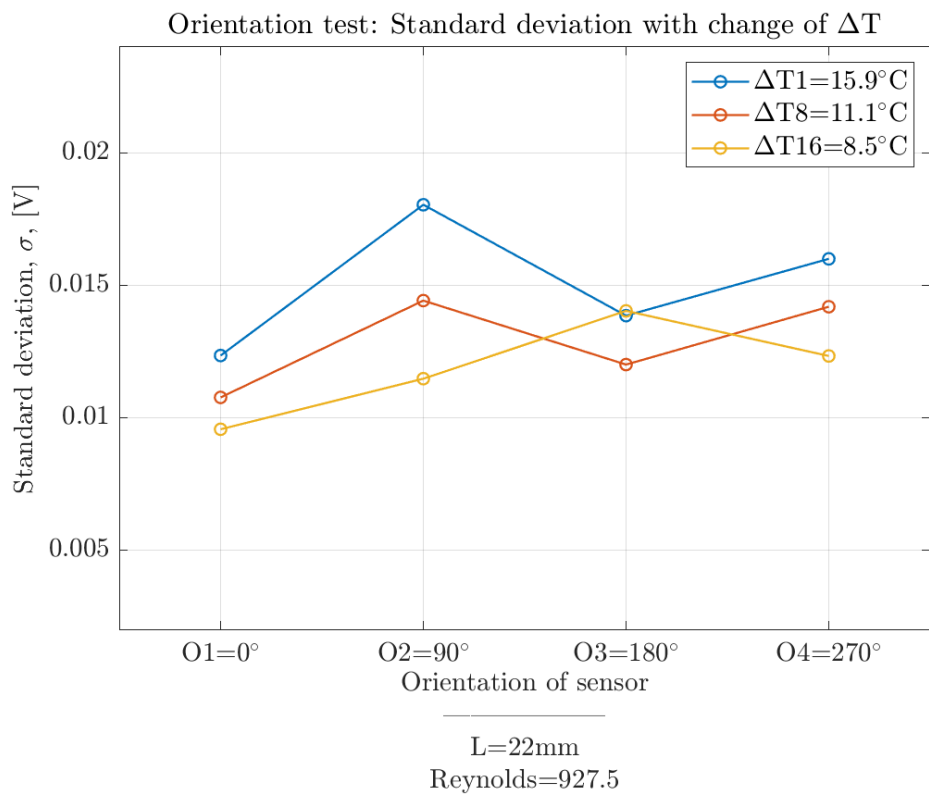
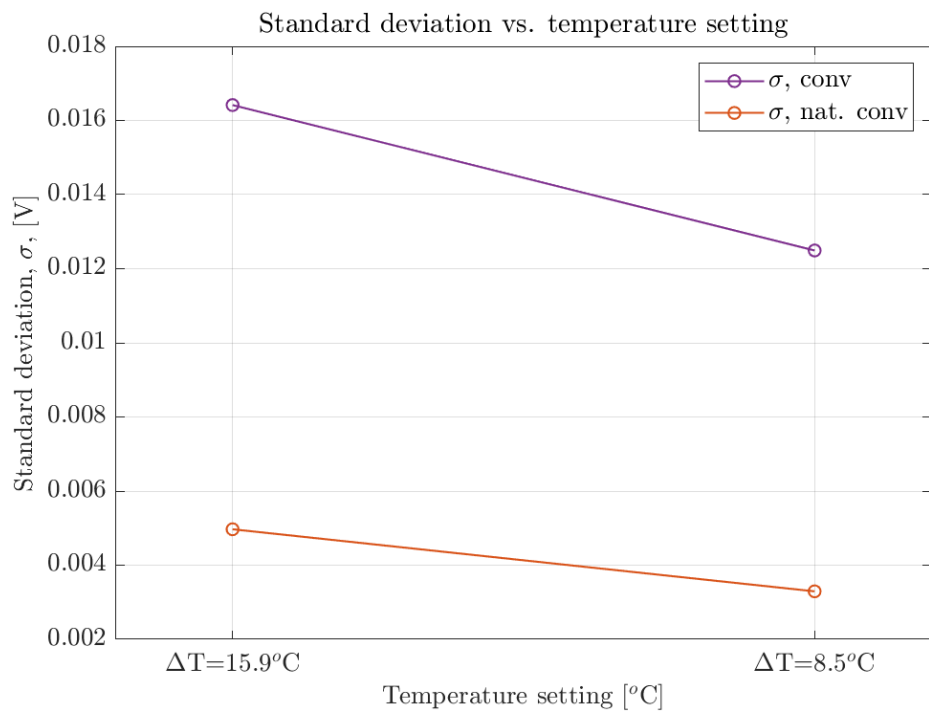
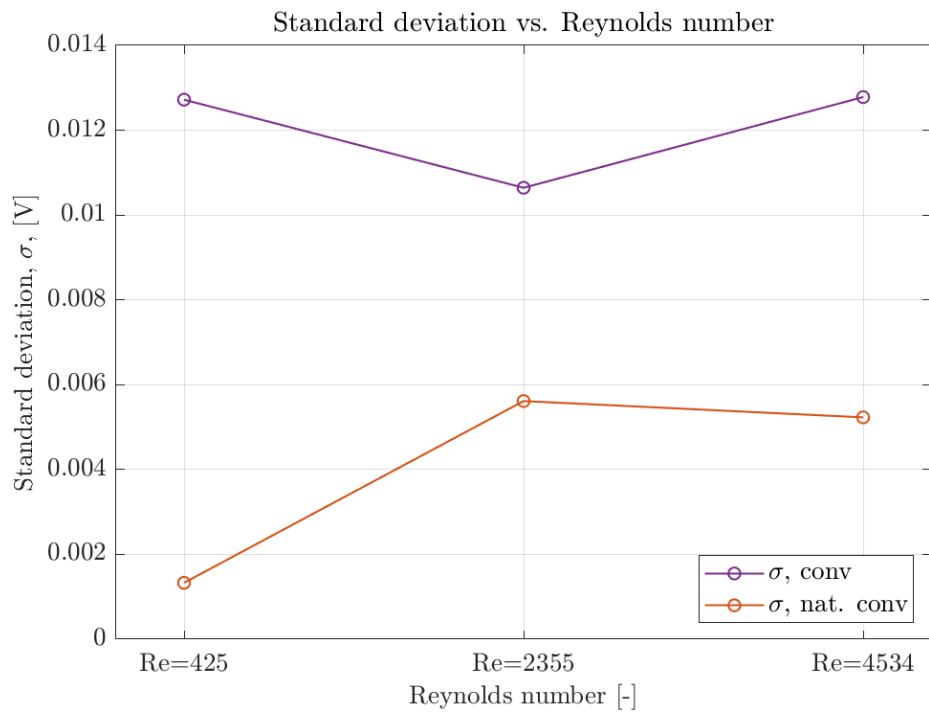


Figure C.12 | Standard deviation vs. temperature setting for orientation test  $\Delta T$ .



**Figure C.13 | Standard deviation vs. temperature setting for forced convection test.**



**Figure C.14 | Standard deviation vs. Reynolds for forced convection test.**

## D | Supplementary Plots - Numerical Study

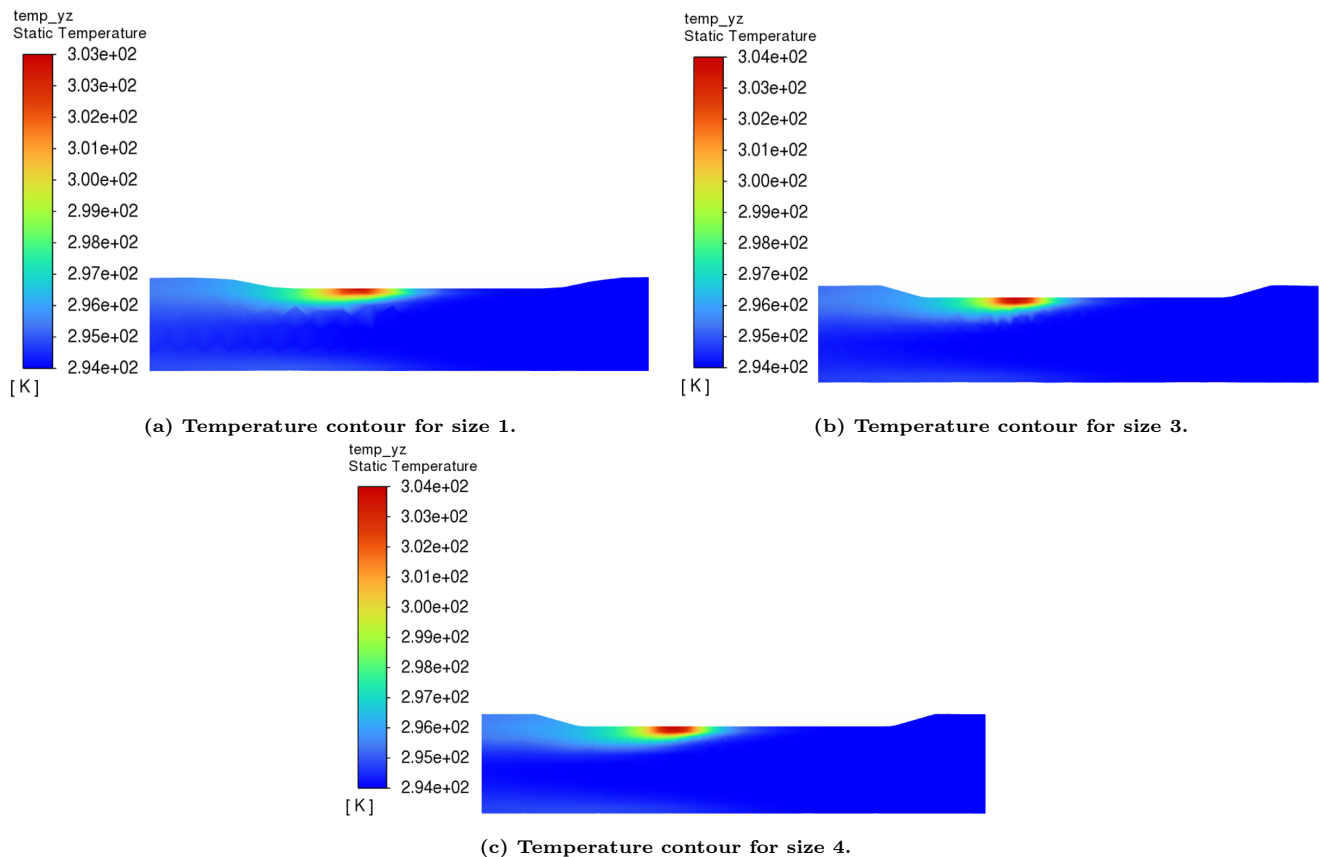


**Figure D.1** | Temperature contours for mesh sizes 1, 3 and 4, for laminar flows where:  $\Delta T = 15.9^\circ\text{C}$ ,  $U = 0.0033 \text{ m/s}$ .

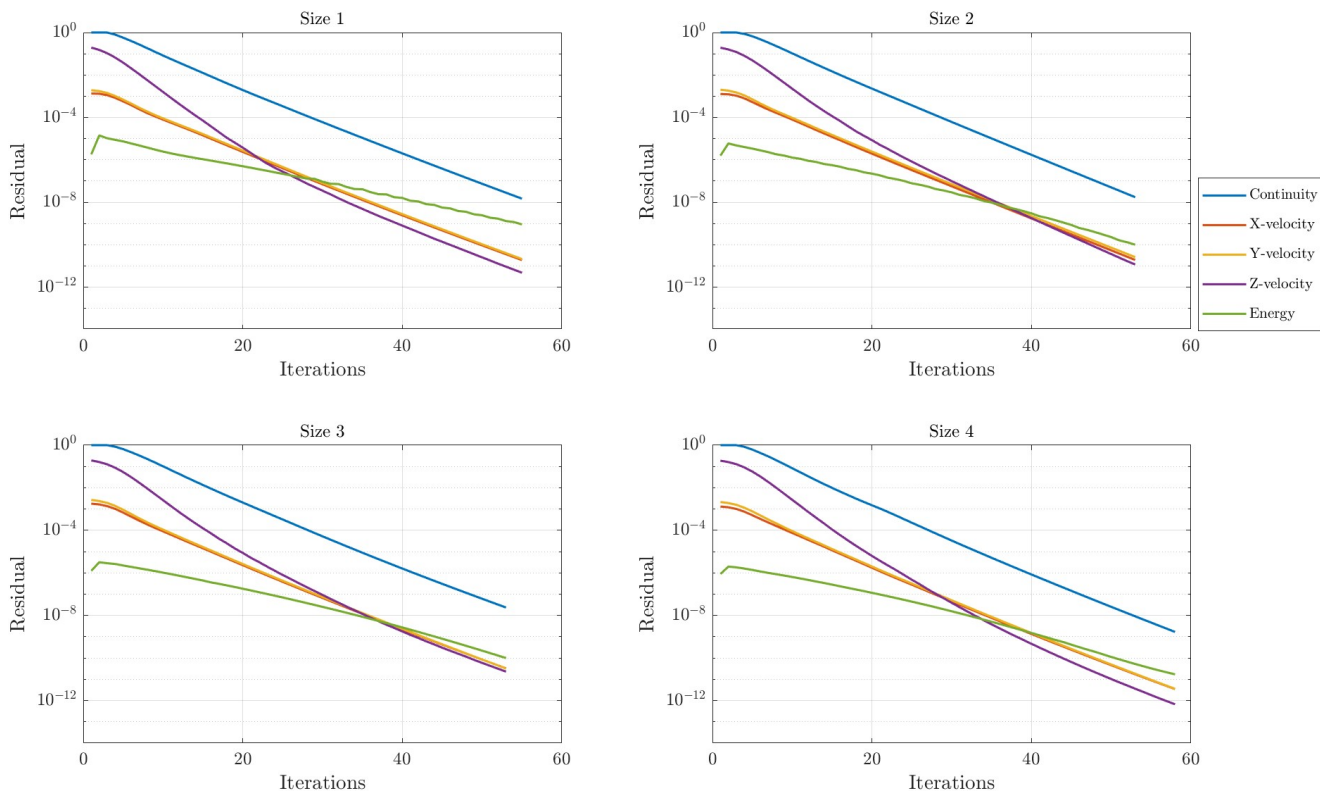


**Figure D.2 |** Residuals for laminar flows for all mesh sizes for  $\Delta T = 15.9^\circ\text{C}$ ,  $U = 0.0033 \text{ m/s}$ .

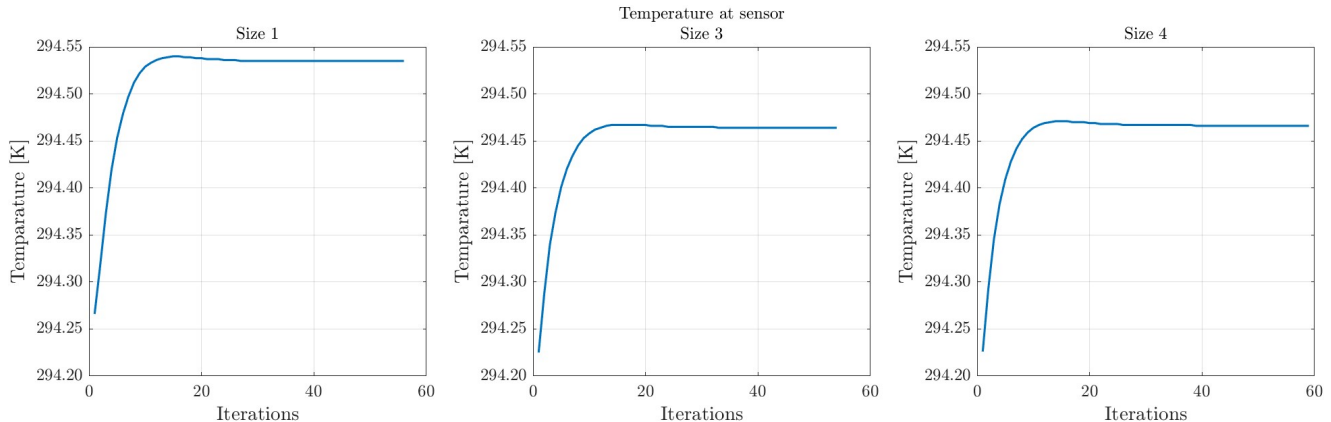


**Figure D.3 |** Temperature convergence at the sensor for laminar flows for mesh sizes 1, 3 and 4 for  $\Delta T = 15.9^\circ\text{C}$ ,  $U = 0.0033 \text{ m/s}$ .

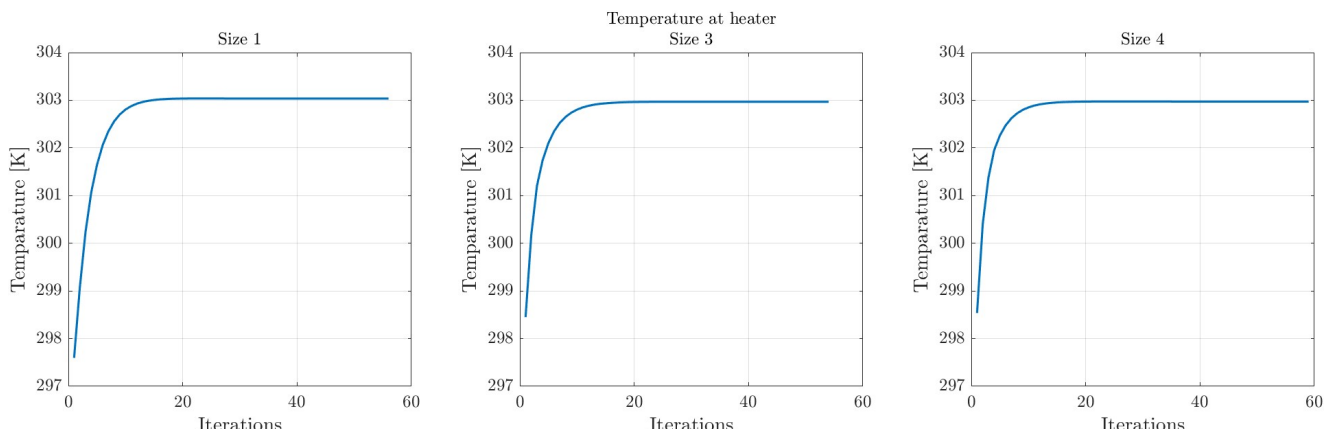


**Figure D.4 |** Temperature convergence at the heater for laminar flows for mesh sizes 1, 3 and 4 for  $\Delta T = 15.9^\circ\text{C}$ ,  $U = 0.0033 \text{ m/s}$ .

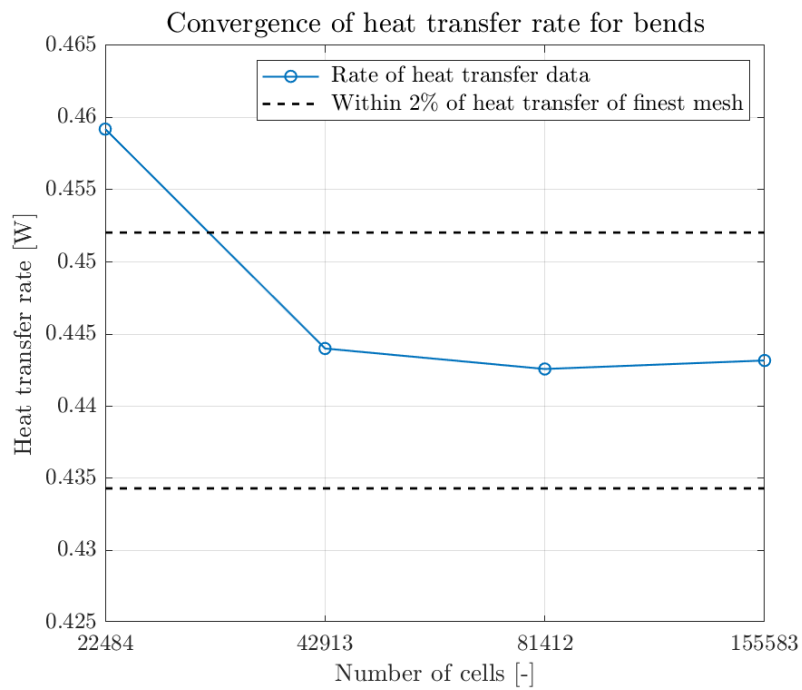


**Figure D.5 | Convergence of heat transfer rate for bends for  $\Delta T = 15.9^\circ\text{C}$ ,  $U = 0.0069 \text{ m/s}$ .**